

SPACE-TIME CONTINUOUS PHASE MODULATION

by

ANNA-MARIE SILVESTER

M.Sc., University of British Columbia, 2004

B.Sc., University of Victoria, 2000

A THESIS SUBMITTED IN PARTIAL FULFILLMENT OF
THE REQUIREMENTS FOR THE DEGREE OF

DOCTOR OF PHILOSOPHY

in

The Faculty of Graduate Studies

(Electrical and Computer Engineering)

THE UNIVERSITY OF BRITISH COLUMBIA
(Vancouver)

December 2008

© Anna-Marie Silvester, 2008

Table of Contents

Table of Contents	i
List of Tables	v
List of Figures	vi
List of Abbreviations	xiv
Notation	xvii
Acknowledgments	xix
1 Introduction	1
1.1 History and Motivation	3
1.2 CPM Foundation	5
1.2.1 CPM Representations	7
1.2.2 CPM & RF Power Amplifiers	11
1.3 Contributions and Organization	17
2 Space-Time Coding for CPM	20
2.1 Transmission Model	23
2.2 Burst-Based OSTBC for CPM	25
2.2.1 Complex Orthogonal Designs (ODs)	25

Table of Contents

2.2.2	Continuous-Phase Modulation (CPM) Specifics	26
2.2.3	Proposed OSTBC Scheme	27
2.2.4	Maximum Likelihood (ML) Detection	29
2.2.5	Performance Analysis	31
2.2.6	Performance Results	34
2.3	Diagonal Block Space-Time (DBST) Coding for CPM	37
2.3.1	Continuous-Phase Modulation (CPM) Specifics	38
2.3.2	Modulation	39
2.3.3	Detection	40
2.3.4	Optimization of DBST-CPM	45
2.3.5	Performance Results	52
2.4	Conclusions	62
3	Distributed ST-CPM	68
3.1	Relay Network Setup	70
3.2	Distributed ST-CPM for Relay Transmission	71
3.2.1	Detection of the Distributed ST-CPM Signals	73
3.2.2	Optimization of Distributed ST-CPM	73
3.2.3	Simulation Results	78
3.3	Energy Consumption of Distributed ST Coding Methods	84
3.3.1	Distributed ST Coding Overview	85
3.3.2	Power Amplifier Modeling	87
3.3.3	Energy Consumption Analysis	90
3.3.4	Simulations	93
3.4	Conclusions	99

4 Concatenated Coding for Space–Time Coding with Continuous Phase Modulation	101
4.1 Concatenated Coded Transmission System	103
4.1.1 Double Parity-Check (DPC) Codes	107
4.1.2 ST–CPM	111
4.1.3 Soft Decoding of ST–CPM	112
4.2 Analysis and Design of Concatenated ST–CPM Using EXIT Charts	117
4.2.1 Generation of the Mutual Information Transfer Characteristics	118
4.2.2 Generation of the EXIT Chart for the AWGN channel	123
4.2.3 Generation of the EXIT chart for the Quasi-Static Fading Channel (QSFC)	125
4.3 Capacity	127
4.3.1 AWGN Channel	127
4.3.2 Quasi-Static Fading Channel	129
4.4 Results and Discussion	131
4.4.1 The AWGN Channel	131
4.4.2 Block Fading Channel	138
4.4.3 Comparison with Previous Work	141
4.5 Conclusions	147
5 Conclusions and Future Work	148
5.1 Research Contributions	148
5.2 General Conclusions	151
5.3 Suggestions for Future Work	151
Bibliography	152

Appendices

A Related Publications 159

List of Tables

2.1	Pseudo-code for distance spectrum calculation for DBST-CPM.	64
2.2	Optimized DBST-CPM for $N_T = 2$ and $M = 4$. Gain with respect to repetition code considering an FER of 10^{-2}	65
2.3	Optimized DBST-CPM for $N_T = 2$ and $M = 8$. Gain with respect to repetition code considering an FER of 10^{-2}	66
2.4	Optimized DBST-CPM for $N_T = 3$ and $M = 4$. Gain with respect to repetition code considering an FER of 10^{-2}	67
4.1	Symbol labeling for $M = 4$	111
4.2	Symbol labeling for $M = 8$	112
4.3	SNR to achieve capacity vs. threshold SNR from EXIT chart analysis for MSK. Note that (*) denotes schemes whose EXIT chart tunnel opens after the ‘threshold’ SNR given in this Table.	133
4.4	SNR to achieve capacity vs. threshold SNR from EXIT chart analysis for binary 1REC with $h = 1/3$ and $h = 1/4$. Note that (*) denotes schemes whose EXIT chart tunnel opens after the ‘threshold’ SNR given in this Table.	134

List of Figures

1.1	Decomposition of CPM into a trellis-encoder and a memoryless modulator using phase-increment mapping.	9
1.2	Decomposition of CPM using phase-state mapping.	10
1.3	A general circuit digram of a power amplifier.	12
1.4	The transistor current of Class A, Class AB, and Class C power amplifiers.	14
1.5	The conduction angle of Class B and Class C amplifiers.	15
2.1	Transmitter and receiver model for CPM with burst-based OSTBC.	23
2.2	Transmitter and receiver model for CPM with burst-based OSTBC.	30
2.3	BER and FER vs. $10 \log_{10}(E_b/\mathcal{N}_0)$ of GMSK with phase-state mapping. Single-antenna transmission ($N_T = 1$), OSTBC ($N_T = 2, N_T = 4$), and the ST coding scheme of [1] ($N_T = 2$) are compared.	34
2.4	BER and FER vs. $10 \log_{10}(E_b/\mathcal{N}_0)$ of binary 2REC with phase-state mapping. Single-antenna transmission ($N_T = 1$), OSTBC ($N_T = 2, N_T = 4$), and the ST coding scheme of [1] ($N_T = 2$) are compared.	35
2.5	BER and FER vs. $10 \log_{10}(E_b/\mathcal{N}_0)$ of 4-ary 1RC with phase-state mapping. Single-antenna transmission ($N_T = 1$), OSTBC ($N_T = 2, N_T = 4$), and the ST coding scheme of [1] ($N_T = 2$) are compared.	36

2.6	Trellis of DBST-CPM for $N_T = 2$ and CPM with 1REC pulse, $M = 4$, and $h = 1/2$. Left: Repetition ST code. Right: Optimal ST code (see Section 2.3.4 for details about ST code optimization).	42
2.7	FER vs. $10 \log_{10}(E_b/\mathcal{N}_0)$ for 1REC pulse, $h = 1/2$, and $M = 4$. DBST-CPM ($N_T = 2$ and $N_T = 3$) with repetition code and optimal code and CPM with $N_T = 1$. Simulation results and the analytical upper bound are compared for the QSFC.	53
2.8	FER vs. $10 \log_{10}(E_b/\mathcal{N}_0)$ for 1REC pulse, $h = 1/2$, and $M = 4$. DBST-CPM ($N_T = 2$) with repetition code and optimal code. MLSD and RSSD with CSI for the QSFC.	55
2.9	FER vs. $10 \log_{10}(E_b/\mathcal{N}_0)$ for 1REC impulse, $h = 1/2$, and $M = 4$. DBST-CPM ($N_T = 2$) with repetition code and optimal code. Coherent detection with CSI and non-coherent detection without CSI for the QSFC. 2-state trellis for repetition code, 4-state trellis for optimal code.	57
2.10	FER vs. $10 \log_{10}(E_b/\mathcal{N}_0)$ for 1REC pulse, $h = 1/2$, and $M = 4$. DBST-CPM ($N_T = 2$) with repetition code and optimal code. Coherent detection with CSI and non-coherent detection without CSI for the QSFC with phase noise with variance $\sigma_{\Delta}^2 = 0.01$. 2-state trellis for repetition code, 4-state trellis for optimal code.	58
2.11	FER vs. $10 \log_{10}(E_b/\mathcal{N}_0)$ for 1REC pulse, $h = 1/2$, and $M = 4$. DBST-CPM ($N_T = 2$) with repetition code and optimal code. Coherent detection with CSI and non-coherent detection without CSI for the continuous fading channel with normalized bandwidth $B_f T = 0.03$. 2-state trellis for repetition code, 4-state trellis for optimal code.	59

2.12 BER vs. $10 \log_{10}(E_b/\mathcal{N}_0)$ for DBST-CPM and the PV scheme [2], both with $N_T = 2$. DBST-CPM: 1REC pulse, $h = 1/2$, and $M = 4$. PV ST-CPM: 1REC pulse, $h = 1/2$, and $M = 4$ (“sub-optimal”) and $M = 8$ (“optimal”). Data rate is 1 bit per symbol duration T in all cases. Non-coherent detection without CSI for the continuous fading channel with normalized bandwidth $B_f T = 0.001$. As reference: DBST-CPM and coherent detection with CSI.	60
2.13 BER vs. $10 \log_{10}(E_b/\mathcal{N}_0)$ for DBST-CPM and the PHK scheme [3], both with $N_T = 2$. DBST-CPM: 1REC pulse, $h = 1/4$, and $M = 4$. PHK ST-CPM: 1REC pulse, $h = 1/2$, and $M = 2$. Data rate is 1 bit per symbol duration T in all cases. Non-coherent detection without CSI for the continuous fading channel with normalized bandwidth $B_f T = f_d T = 0.01$ and $B_f T = f_d T = 0.03$ according to Clarke’s model for DBST-CPM and a third order Butterworth spectrum for PHK scheme. $N_d = 10$ for DBST-CPM corresponds to $N = 5$ for the PHK scheme.	61
3.1 Two phase transmission in the relay network.	71
3.2 Annealing algorithm for signature set generation.	79
3.3 Average distribution losses as a function of the total number of nodes N , and the number of active nodes $N_S = 2, 3, 5$. Deterministic signature vector sets optimized for $N_a = N_c = 2$ active nodes and random signature vector sets are considered. ‘CE’ indicates constant envelope sets.	80

3.4	Average BER of a distributed ST-CPM code versus $10 \log_{10}(E_b/N_0)$ for a network with $N = 30$ nodes and different numbers of active nodes N_S . Deterministic signature vector sets optimized for $N_a = N_c = 2$ active nodes and random signature vector sets are considered. ‘CE’ indicates constant envelope sets. The ST-CPM code is optimized for $N_c = d = 2$ with the CPM parameters $M = 4, h = 1/4$, and a 1REC phase pulse as given in [4, Table I].	81
3.5	Average BER of a distributed ST-CPM code versus $10 \log_{10}(E_b/N_0)$ for a network with $N = 30$ nodes where the number of active nodes N_S depends on the probability p that any given node is listening for the source’s transmission. Deterministic signature vector sets optimized for $N_a = N_c = 2$ active nodes and random signature vector sets are considered. ‘CE’ indicates constant envelope sets. The ST-CPM code is optimized for $N_c = d = 2$ with the CPM parameters $M = 4, h = 1/4$, and a 1REC phase pulse as given in [4, Table I].	83
3.6	Drain efficiency, η , (%), power added efficiency, PAE, (%), output power, P_{out} , (dBm), dc power supplying the power amplifier, P_{dc} , (dBm), and power gain - output power minus input power (dB) vs. input power for the Class AB power amplifier designed by Carls <i>et al.</i> [5].	89
3.7	Drain efficiency, η , (%), power added efficiency, PAE, (%), output power, P_{out} , (dBm), dc power supplying the power amplifier, P_{dc} , (dBm), and power gain - output power minus input power (dB) vs. input power for the Class C power amplifier designed by Cao <i>et al.</i> [6].	90
3.8	BER performance vs. input power P_{in} (dBm) of the distributed ST-LM code for different values of total loss (N_L). Class C amplifier [6].	94

3.9	Total energy (nJ) per active node, per symbol vs. maximum transmission distance (m) to achieve a BER of 10^{-3} for a distributed ST-LM scheme ('LIN') and a distributed ST-CPM scheme ('CPM'). The number of active nodes includes $N_s = 2, 3$, and 5. A Class AB amplifier [5] is employed. . . .	96
3.10	Total energy (nJ) per active node, per symbol vs. maximum transmission distance (m) to achieve a BER of 10^{-3} for a distributed ST-LM scheme ('LIN') and a distributed ST-CPM scheme ('CPM'). The number of active nodes includes $N_s = 2, 3$, and 5. A Class C amplifier [6] is employed. . . .	97
3.11	Total energy (nJ) per active node, per symbol vs. maximum transmission distance (m) for $N_s = 5$ active nodes and for a distributed ST-LM scheme ('LIN') and a distributed ST-CPM scheme ('CPM'). Results are shown for BERs of 10^{-2} , 10^{-3} , and 10^{-4} . A Class C amplifier [6] is employed. . . .	98
4.1	Block diagram of a serially concatenated transmission system.	104
4.2	Block diagram of a serially concatenated transmission system.	105
4.3	The structure of the DPC I rate $k/(2k - 1)$ code.	107
4.4	The structure of the DPC II rate $k/(2k + 1)$ code.	108
4.5	Generation of the forward and backward recursion metrics ($f[i]$ and $b[i]$) for DPC I and DPC II.	110
4.6	Plot of the $J(\sigma)$ function.	121
4.7	Mutual information transfer chart for the DPC codes.	123
4.8	EXIT chart depicting the mutual information transfer for the DPC II rate 10/21 code and for the ST-CPM code employing $N_T = 1$ transmit antenna, and $M = 4$, $h = 1/4$, a 1REC pulse with Ungerboeck mapping, and with an SNR (AWGN channel) of ranging from $10 \log_{10}(E_b/\mathcal{N}_0) = +0.2$ dB to +5.2 dB in increments of 0.2 dB.	124

4.9	Two EXIT charts illustrating the effect of interleaver length on the decoding trajectory. On the left a short interleaver is used, and on the right a long interleaver is used.	126
4.10	Estimated Capacity for $M = 4$ CPM employing a 1REC phase pulse, and with $h = 1/4$	130
4.11	The mutual information transfer characteristics of a select group of DPC I and DPC II codes, and MSK (CPM: $M = 2$, 1REC phase pulse and $h = 1/2$) with E_b/\mathcal{N}_0 in steps of 0.5 dB.	132
4.12	Estimated capacity (bold curves) and simulated BER (non-bold curves) vs. $10 \log_{10}(E_b/\mathcal{N}_0)$ for MSK (CPM: $M = 2$, 1REC phase pulse and $h = 1/2$) concatenated with DPC I class codes (in the figure to the left) and DPC II class codes (in the figure to the right).	135
4.13	EXIT chart showing the threshold SNR for three labelings of CPM ($M = 4$, $h = 1/4$, a 1REC phase pulse) and the rate 10/21 DPC II code. SNR is E_b/\mathcal{N}_0	136
4.14	Estimated capacity (bold curve) and simulated BER (non-bold curves) vs. $10 \log_{10}(E_b/\mathcal{N}_0)$ for CPM: $M = 4$, 1REC phase pulse and $h = 1/4$) concatenated with the rate 10/21 rate DPC II code.	138
4.15	Mutual information transfer chart for the ST-CPM code employing $N_T = 1$ transmit antenna, and $M = 8$, $h = 1/4$, a 2RC pulse, and with a SNR of $10 \log_{10}(E_b/\mathcal{N}_0) = -2.0$ dB and the symbol mappings given in Table 4.2.	139
4.16	Estimated capacity (bold curve) and simulated BER (non-bold curves) vs. $10 \log_{10}(E_b/\mathcal{N}_0)$ for CPM: $M = 8$, 2RC phase pulse and $h = 1/4$) concatenated with the rate 10/21 rate DPC II code.	140

4.17 EXIT chart for $N_T = 2$ ($M = 4$, 1REC, $h = 1/4$) and the 10/21 rate DPC II code. The UL, GL1 and GL2 are shown at their threshold SNRs.	141
4.18 EXIT chart for $N_T = 3$ ($M = 8$, 2RC, $h = 1/4$) and the 10/21 rate DPC II code. The UL and SSPL are shown for SNRs of 1.4, 5.0, and 10.0 dB. . . .	142
4.19 Estimated outage probability (bold curve) and simulated FER (non-bold curves) vs. $10 \log_{10}(\bar{E}_b/\mathcal{N}_0)$ for concatenated ST-CPM. Results for $N_T = 2$ ($M = 4$, 1REC, $h = 1/4$), and $N_T = 3$ ($M = 8$, 2RC, $h = 1/4$) and the 10/21 rate DPC II code. UL, GL1, and GL2 shown for $N_T = 2$, and UL, and SSPL shown for $N_T = 3$	143
4.20 BER vs. $10 \log_{10}(\bar{E}_b/\mathcal{N}_0)$ for the concatenated CPM scheme proposed by Moqvist and Aulin in [7], and for the proposed scheme employing MSK concatenated with the rate 10/21 DPC II code over an AWGN channel. . .	144
4.21 FER vs. $10 \log_{10}(\bar{E}_b/\mathcal{N}_0)$ for the concatenated CPM scheme employing a (7,5) convolutional code as proposed by Zhang and Fitz in [8], [9], and the performance of CPM concatenated with the rate 10/21 DPC II code. The channel is a continuous fading channel with fading bandwidth $B_f T = 0.008$, and $N_T = 2$, $N_R = 2$ antenna are employed. The underlying CPM scheme is 1RC, $h = 1/4$, $M = 4$. The interleaver length is 256 bits, and 5 iterations are used.	145

4.22 BER vs. $10 \log_{10}(\bar{E}_b/\mathcal{N}_0)$ for the concatenated CPM scheme denoted as ‘system B’ by Bokomulla and Aulin [9], and the proposed scheme. Both schemes employ $N_T = 2$, $N_R = 2$, and a 600 bit interleaver. ‘System B’: (7,5) convolutional outer code, MSK and a $\Delta fT = 1/6$ normalized carrier offset. ST-CPM and DPC code: rate 10/21 DPC II code, 2RC phase pulse, $M = 4$, and $h = 1/4$. The channel is a QSFC constant for $f = 1, 10, 30$ symbol intervals. 10 iterations are permitted. 146

List of Abbreviations

APP	<i>A Posteriori</i> Probability
AWGN	Additive White Gaussian Noise
BER	Bit Error Rate
BCJR	Bahl, Cocke, Jelinek and Raviv
BICM	Bit-Interleaved Coded Modulation
BPSK	Binary Phase Shift Keying
CC	Convolutional Code
cdf	Cumulative Density Function
CPM	Continuous-Phase Modulation
CRC	Cyclic Redundancy Check
DF	Decode and Forward
DFDD	Decision Feedback Differential Detection
DPC	Double Parity Check
DPSK	Differential Phase Shift Keying
DSTM	Differential Space-Time Modulation
CSI	Channel State Information
EXIT	EXtrinsic Information Transfer
FB	Forward-Backward
FEC	Forward Error Correction
GMSK	Gaussian Minimum Shift Keying

List of Abbreviations

GSM	Global System for Mobile Communication
IEEE	Institute of Electrical and Electronic Engineers
i.i.d.	Independent, Identically Distributed
LLR	Log-Likelihood Ratio
M -FSK	M -ary Frequency Shift Keying
ML	Maximum-Likelihood
M -PAM	M -ary Pulse Amplitude Modulation
M -PSK	M -ary Phase Shift Keying
M -QAM	M -ary Quadrature Amplitude Modulation
MIMO	Multiple-Input Multiple-Output
MMSE	Minimum Mean Square Error
MRC	Maximum-Ratio Combining
NB	Narrowband
OD	Orthogonal Design
PAM	Pulse Amplitude Modulation
PAPR	Peak to Average Power Ratio
pdf	Probability Density Function
PEP	Pair-wise Error Probability
QAM	Quadrature Amplitude Modulation
QPSK	Quaternary Phase Shift Keying
QSFC	Quasi-Static Fading Channel
REC	Rectangular
RC	Raised-Cosine
SISO	Single-Input Single-Output
SNR	Signal-to-Noise Ratio

List of Abbreviations

SRN	Square-Root Nyquist
ST	Space-Time
STBC	Space-Time Block Code
STTC	Space-Time Trellis Code
WLAN	Wireless Local Area Network
WSN	Wireless Sensor Network
WPAN	Wireless Personal Area Network

Notation

Throughout this thesis, bold upper case and lower case letters denote matrices and vectors, respectively. The remaining notation and operators used in this thesis are listed as follows:

$(\cdot)^*$	Complex conjugation
$[\cdot]^T$	Transposition
$[\cdot]^H$	Hermitian transposition
$\det(\cdot)$	Matrix determinant
$ \cdot $	Absolute value of a complex number
$\ \cdot\ _2$	L_2 -norm of a vector
$\text{Re}\{\cdot\}$	Real part of a complex number
$\text{Im}\{\cdot\}$	Imaginary part of a complex number
$\mathcal{E}_x(\cdot)$	Statistical expectation with respect to x
$\text{Pr}\{\cdot\}$	Probability of an event
$J_0(\cdot)$	Zeroth order modified Bessel function of the first kind
$\text{diag}(\mathbf{x})$	A matrix with the elements of vector \mathbf{x} on the main diagonal
\otimes	Convolution operator
\mathbf{I}_X	$X \times X$ identity matrix
$\mathbf{0}_X$	All-zero column vector of length X
$\mathcal{N}(\mu, \sigma^2)$	Gaussian RV with mean μ and variance σ^2
$j \triangleq \sqrt{-1}$	Imaginary unit
$\text{card}\{\cdot\}$	Cardinality of a set

$\text{vec}\{\cdot\}$	Vectorization of a matrix
$r(\cdot)$	Rank of a matrix
\oplus	Modulo-2 addition

Acknowledgments

First and foremost, I would like to thank Professor Lutz Lampe for the advice, technical insight, and encouragement he provided throughout my work on this thesis. Professor Lampe willingly gave his of time and energies to assist me in my work, and for this I will always be very grateful. I would also like to thank Professor Robert Schober for many stimulating and helpful discussions.

I would also like to thank my friends and colleagues at the Department of Electrical and Computer Engineering at the University of British Columbia for many lively, educational, and entertaining discussions.

This work was supported by the Natural Sciences and Engineering Research Council (NSERC) of Canada, Bell Canada, and the University of British Columbia Graduate Fellowship.

Chapter 1

Introduction

Wireless technologies have become a permanent fixture in many aspects of our day-to-day lives. We use cell phones, personal digital assistants, wireless networks (for example wireless local area networks (WLANs)), wireless cable replacement (for example wireless personal area networks (WPANs)), and wireless sensors on a daily basis. This proliferation of wireless devices, accompanied by a desire to transmit increasing large amounts of data, has placed an intense pressure on a limited frequency spectrum. Compounding the problem, the wireless channel itself presents a considerable obstacle to communication. Attenuation due to the destructive addition of multipaths can cause deep fades, occasionally making detection of transmitted signals impossible.

One of the techniques with great potential to combat fading and/or to increase the data rate of the wireless system is space-time (ST) coding, pioneered by Tarokh *et al.* [10], Alamouti [11], Foschini and Gans [12], Teletar [13], and Wittneben [14] amongst others. The ST code delivers duplicate copies of the transmitted signal to the receiver using multiple antennas at the transmitter and possibly also at the receiver, and transmitting over multiple time intervals. This diversity in space provides a form of protection for the signal against a fade occurring on the channel between one transmit/receive antenna pair in any given time interval. The ST code can be used either to increase the quantity of information transmitted without increasing system bandwidth, or to improve the reliability of the transmitted information, or to provide some combination of increased data rate and increased reliability. If increased data rate is the goal, then it has been shown that when

the ST code is properly constructed capacity grows linearly with every transmit and receive antenna pair added to the multiple antenna system. If increased reliability is the goal, then it has been shown that when the error rate of the multiple antenna system is plotted versus signal-to-noise ratio (SNR) on a log-log scale the slope of the curve is determined by the product of the number of transmit and receive antennas. Note that both cases require that the channel provides spatial selectivity.

Another concern for wireless communication is that as the number of wireless devices in daily use grows the wireless device itself is shrinking. Reduced device size often comes at the cost of reduced battery capacity. For a cell phone reduced battery capacity means that the user must charge his or her phone more often, however for a remote wireless sensor reduced battery capacity means reduced lifetime. Thus, the ever decreasing size of the wireless device is imposing an ever increasing need for energy efficiency on the underlying communication scheme.

In this area, continuous-phase modulation (CPM) has the potential to provide considerable energy savings. CPM is a modulation technique that involves the transmission of a signal with continuous-phase and a constant envelope. The continuous-phase property produces a very bandwidth efficient signal, and the constant-envelope property enables non-linear (and thus energy efficient) signal amplification. In fact, CPM has been adopted for use with Bluetooth and the Global System for Mobile Communication (GSM) because of these very properties.

This thesis will focus on the combination of ST coding and CPM with application to all wireless networks, but with a specific focus on wireless sensor networks. The ST-CPM code is of special interest in this environment because in this environment energy consumption is highly constrained. The remainder of this chapter will provide a background for the introduction of the proposed ST-CPM codes and coding schemes. In Section 1.1, we

review previously proposed ST-CPM schemes and motivate the need for further study in this area. Section 1.2, provides a background on CPM and introduces the representation of CPM used in this thesis. Further, this section overviews the power amplifier, and explains why CPM is more energy efficient than linear modulations. Finally, Section 1.3 concludes this chapter with a summary of the contributions made by this thesis.

1.1 History and Motivation

Space-time (ST) coding schemes that employ linear and thus, in general, non-constant envelope modulation formats have been widely studied. Although these schemes are highly effective at alleviating the effects of multipath fading over the wireless channel, a ST-CPM scheme has the potential to offer performance gains in the fading channel *and* increased bandwidth and energy efficiency. Increased bandwidth efficiency is due to the continuous-phase property of CPM, which reduces the spectral side lobes of this scheme with respect to linear modulation schemes. Increased energy efficiency is result of both the ST component and the CPM component. Space-time coding improves the system error rate in direct relation to the number of transmit and receive antennas employed. Thus, increasing the number of antennas in the system allows the signal to be transmitted with less energy while still maintaining a target BER. CPM contributes to a reduction in the amount of energy expended by the hardware of the wireless device. The constant envelope property of CPM means that lower power, more energy efficient power amplifiers can be used than are used for linear modulations.

Although the combination of ST coding and CPM has a great deal of promise, the design of a ST-CPM coding scheme is not straightforward due to the memory inherent to CPM. Previous efforts to extend the concept of ST coding to CPM have yielded high decoding complexity [1], or reduced error-rate performance [15]. Both of these schemes

require modified CPM receivers. Other efforts have produced ST codes that are designed for specific CPM formats, e.g. [16], [17], [18], [19], and [20]. Non-coherent detection of ST-CPM codes, which removes the assumption of perfect channel state information at the receiver, has been the subject of very little investigation. In practical systems, perfect channel state information as assumed by coherent detection schemes is not available at the receiver, and estimates of the channel state are obtained using methods that substantially increase the overhead of the transmission scheme. The previous work on non-coherent detection of ST-CPM that has been conducted was performed by [2] and [3], and in both cases it was limited to specific CPM formats. Thus, in Chapter 2 we propose two ST-CPM coding schemes that can use any CPM format, any number of transmit and receive antennas, and existing CPM receivers. The second scheme is a general design method suited for non-coherent detection.

As mentioned earlier, the device with perhaps the most stringent constraints on energy consumption is the remote wireless sensor. Networks of these wireless sensors have the potential to take the place of wired sensor networks. In addition, many new applications are evolving in which only wireless sensors are appropriate, for example object tracking and battlefield surveillance. One of the technologies that may enable the widespread use of wireless sensors is distributed ST coding, a scheme in which spatially separated cooperating devices can produce a diversity gain in a fading channel. Again, distributed ST coding schemes employing linear modulation have been the subject of much investigation, e.g. [21], and [22]. The design of the majority of these distributed ST codes calls for the multiplexing of two or more data streams, which has the potential to greatly increase the peak-to-average power ratio (PAPR) of the resulting signal and thereby increase the energy consumed in the device hardware. In general, minimizing the energy consumption of a wireless device is important, however, minimizing the energy consumption of a device employing distributed

ST coding will be even more important. Employing relaying implies that several devices are involved in the transmission of most messages meaning that each wireless device will be active more often. Also, the performance of distributed ST schemes is often dependent upon the number of available relays, therefore, minimizing energy consumption will maintain the connectivity of the network over a longer period of time thereby extending the length of time that cooperative diversity gains are available. Thus, in Chapter 3, we propose a distributed ST-CPM code.

Improved error-rates can be obtained by employing a ST-CPM code as the inner code in a serially concatenated code. The resulting code can have both the capacity approaching performance and the energy efficiency offered by ST-CPM. CPM is an excellent candidate for the inner code in the concatenated system as it is recursive in nature. To date, serially concatenated codes designed for CPM, and ST-CPM have primarily employed convolutional codes [8], [9], and [23]. Recently a class of codes called double parity check (DPC) codes were introduced for use with differential phase shift keying (DPSK) [24]. These codes yielded capacity approaching performance with very low complexity. In Chapter 4, we investigate the performance of a serially concatenated system employing the low complexity DPC codes as an outer code, and ST-CPM as the inner code.

1.2 CPM Foundation

Before launching into a discussion of CPM in the context of ST coding, we begin with a brief description of the properties of CPM. The passband CPM signal is given by

$$x_{\text{PB}}(t) = \frac{\sqrt{2E_s}}{T} \cos(\Phi(t, \mathbf{a})) = \frac{\sqrt{2E_s}}{T} \cos(2\pi f_c t + \phi(t, \mathbf{a}) + \phi_0), \quad (1.1)$$

where E_s is the energy per symbol (transmitted in the interval T), f_c is the carrier frequency, and \mathbf{a} is the sequence of M -ary input data symbols $a[i]$, $a[i] \in \pm 1, \pm 3, \dots, \pm(M-1)$. ϕ_0 is a constant that denotes the initial phase of the CPM signal, which we set to zero without loss of generality. The equivalent baseband signal, which we employ in this work, is given by

$$x(t) = \frac{\sqrt{E_s}}{T} e^{j\phi(t, \mathbf{a})}. \quad (1.2)$$

The information carrying phase in (1.1) and (1.2) is given by

$$\phi(t, \mathbf{a}) = 2\pi h \sum_{i=0}^{\infty} a[i] \int_{-\infty}^t g(\tau - iT) d\tau = 2\pi h \sum_{i=0}^{\infty} a[i] q(t - iT), \quad (1.3)$$

where h denotes the modulation index, and $h = k/p$ is assumed to be rational and irreducible. The frequency pulse $g(t)$ is any function that is positively defined over the interval $0 \leq t < LT$, and that is normalized such that $\int_{-\infty}^{\infty} g(t) dt = 1/2$. The corresponding phase pulse $q(t)$ is given by

$$q(t) = \begin{cases} 0 & t < 0 \\ \int_0^t g(\tau) d\tau & 0 \leq t < LT \\ 1/2 & t \geq LT \end{cases}$$

If $L = 1$, then the CPM scheme is called *full response*, and if $L > 1$ the CPM scheme is called *partial response*. In this thesis, we consider both full and partial response CPM. Also, we consider three popular pulse shapes, i.e. rectangular, (REC), raised cosine (RC),

and Gaussian minimum shift keying (GMSK) given below

$$\text{LREC :} \quad g(t) = \begin{cases} \frac{1}{2LT}, & 0 < t < LT \\ 0, & \text{otherwise,} \end{cases} \quad (1.4)$$

$$\text{LRC :} \quad g(t) = \begin{cases} \frac{(1-\cos(2\pi t/LT))}{2LT}, & 0 < t < LT \\ 0, & \text{otherwise,} \end{cases} \quad (1.5)$$

$$\text{GMSK :} \quad g(t) = \left\{ Q \left[\frac{2\pi B(t-\frac{T}{2})}{(\ln 2)^{1/2}} \right] - Q \left[\frac{2\pi B(t+\frac{T}{2})}{(\ln 2)^{1/2}} \right] \right\}, \quad Q(t) = \int_t^{\infty} \frac{1}{\sqrt{2\pi}} e^{-x^2/2} dt. \quad (1.6)$$

1.2.1 CPM Representations

The phase transitions of CPM can be represented by a trellis structure. However, the construction of CPM outlined to this point has a time-variant trellis with $2pM^{L-1}$ states, of which only half are occupied at any given time. In this thesis, we will adopt the representation of CPM developed independently by Rimoldi in [25] and Huber and Liu in [26] that has a time-invariant trellis. To achieve the time invariant trellis a slope function $c(t)$ is introduced [26]

$$c(t) \triangleq \begin{cases} 0, & t < 0 \\ \frac{(M-1)}{2LT}t, & 0 \leq t < LT \\ \frac{M-1}{2}, & t \geq LT \end{cases} \quad (1.7)$$

and a zero term is added to the phase term $\Phi(t, \mathbf{a})$ given in Eq. (1.1) resulting in the following expression of the phase function

$$\Phi(t, \mathbf{a}) = 2\pi f_c t - 2\pi h \sum_{i=-\infty}^n c(t - iT) + \phi(t, \mathbf{a}) + 2\pi h \sum_{i=-\infty}^n c(t - iT). \quad (1.8)$$

The first two terms in Eq. (1.8) can be combined by defining a new reference frequency f_r , given by

$$f_r = f_c - h \frac{(M-1)}{2T}, \quad (1.9)$$

and the third and fourth terms can be re-expressed using a unipolar information symbol $b[i]$, given by

$$b[i] = \frac{a[i] + M - 1}{2} \in \{0, 1, \dots, M - 1\}. \quad (1.10)$$

Using Eqs. (1.9) and (1.10), the phase term given in Eq. (1.8), within the interval $nT \leq t < (n+1)T$, becomes

$$\Phi(t, \mathbf{b}) = 2\pi f_r t + \phi_r + \frac{2\pi}{p} \Psi[n-L] + 2\pi h \sum_{i=n-L+1}^n p(t-iT, b[i]) \quad (1.11)$$

where ϕ_r is the modified initial phase, $\Psi[n-L]$ is the modified normalized phase state given by

$$\Psi[n-L] = \left[k \sum_{i=-\infty}^{n-L} b[i] \right] \bmod (p) \in 0, 1, \dots, p-1 \quad (1.12)$$

and $p(t-iT, b[i])$ is the phase state transition function given by

$$p(t-iT, b[i]) = (2b[i] - (M-1))q(t) + c(t). \quad (1.13)$$

The modified information carrying phase, which can be substituted into (1.1) and (1.2) in place of $\phi(t, \mathbf{a})$ is given by

$$\phi(t, \mathbf{b}) = \frac{2\pi}{p} \Psi[n-L] + 2\pi h \sum_{i=n-L+1}^n p(t-iT, b[i]). \quad (1.14)$$

Finally, using this representation the resulting CPM modulator can be split into two components: a trellis encoder with pM^{L-1} states, and a signal mapper containing pM^L possible

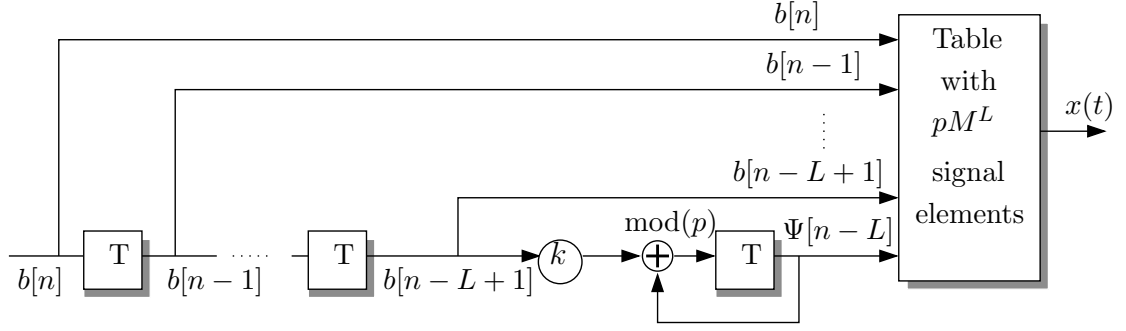


Figure 1.1: Decomposition of CPM into a trellis-encoder and a memoryless modulator using phase-increment mapping.

signals. These signals can be uniquely referenced by an address vector $\mathbf{d}[n]$, given by

$$\mathbf{d}[n] = [\Psi[n-L], b[n-L+1], \dots, b[n-1], b[n]]. \quad (1.15)$$

The construction of the CPM signal as it is outlined above has been called *phase-increment* mapping by [27]. A block diagram of the phase-increment CPM modulator is shown in Figure 1.1. This name has been applied because input data is mapped to a phase change, and the resulting signal is rotationally phase invariant. However, due to the recursive structure of the phase-increment mapper, one error event will affect at least two symbols. An alternative structure for the CPM modulator was suggested in [27] and employs *phase-state* mapping, which alleviates the double error problem, but results in a rotationally phase variant signal. A block diagram of the phase-state CPM modulator is shown in Figure 1.2. The symbols \mathbf{b} are generated using

$$(kb[n])\text{mod}(p) = (\Psi[n] - \Psi[n-1])\text{mod}(p) \quad (1.16)$$

The representation of CPM discussed above showed that CPM can be split into a trellis encoder and a signal mapper that transmits one of pM^L possible signals. Further, there

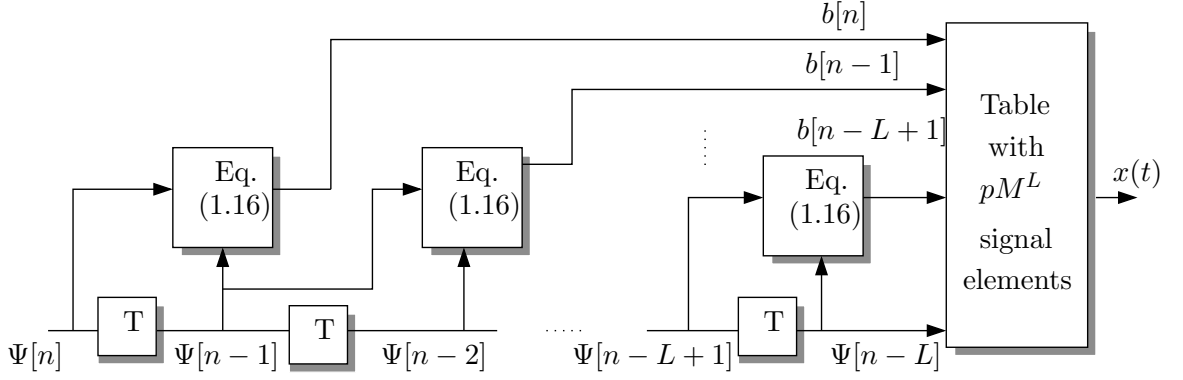


Figure 1.2: Decomposition of CPM using phase-state mapping.

are M^L transmitted signals differentiated by only by the initial phase state $\Psi[n-L]$. Thus, optimally the CPM receiver requires a bank of M^L baseband matched filters [26]. In the wireless sensing applications that we consider device complexity is always a concern. Therefore, we adopt the reduced matched filter set described in [26]. In [26], it was shown that the number of filters required to provide a sufficient statistic can be upper bounded by D_{\max} , which is given by

$$D_{\max} = \lceil 1.11h(M-1) + 2.22 \rceil. \quad (1.17)$$

For most practical combinations of modulation index, h , and modulation order, M , $D = 2$, or 3 matched filters are sufficient. The corresponding baseband receiver filters proposed by [26] are given by

$$h_D^d(t) = \frac{1}{T} e^{j2\pi f_d t}, \quad 0 \leq t < T, \quad d \in \{1, 2, \dots, D\}, \quad (1.18)$$

where

$$f_d = \frac{\Delta f}{2}(2d - 1 - D), \quad d \in \{1, 2, \dots, D\}. \quad (1.19)$$

In these equations that specify the basis functions for the receiver filters only one pa-

parameter, the frequency spacing parameter Δf , needs to be optimized with respect to the transmitted CPM scheme. The optimal value of Δf can be found by maximizing the minimum Euclidean distance for the CPM scheme. In [26] and [27], it is shown that minimal losses are incurred for $0.25 < \Delta f < 0.75$ when $D = 2$, or 3 received filters are used. Therefore, rather than optimize Δf for each CPM scheme that we study, we will set $\Delta f = 0.5$ for all schemes.

The matched filter bank required for demodulation can be denoted by the matrix

$$\mathbf{h}_D(t) = [h_D^1(t), h_D^2(t), \dots, h_D^D(t)]. \quad (1.20)$$

The basis functions of the reduced matched filter bank, $h_D^d(t)$, are not orthogonal. Therefore, a matrix \mathbf{C} is introduced to account for the cross-correlations of the basis functions. This matrix is given by

$$\mathbf{C} = \frac{1}{T} \int_0^T \mathbf{h}_D^T(t) \mathbf{h}_D^*(t) dt, \quad (1.21)$$

1.2.2 CPM & RF Power Amplifiers

The use or study of CPM is often justified by the energy efficiency of this modulation technique. The energy savings made possible by CPM are due to its constant envelope property that enables the use of non-linear power amplifiers. Here, we briefly overview the properties of the RF power amplifier and explain how CPM and the Class C power amplifier save energy. In Chapter 3, we will analyze in more detail the energy savings resulting from the use of CPM in a distributed network. Note that in this section an uppercase symbol denotes a direct current (dc) value, and a lowercase value denotes an alternating current (ac) value.

A generalized RF power amplifier is shown in Fig 1.3. The energy consumption and linearity of the power amplifier are determined by the quantity of time that the transistor

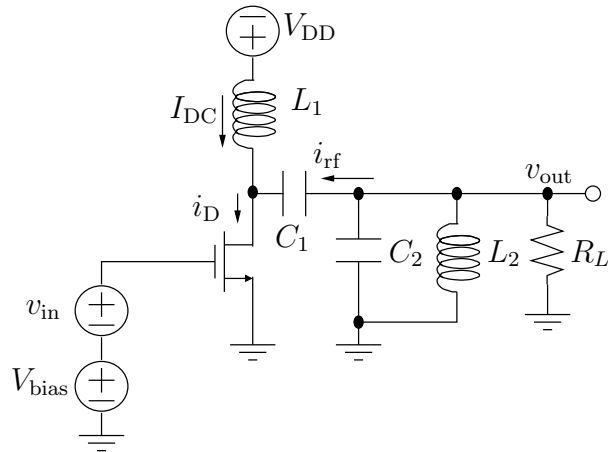


Figure 1.3: A general circuit diagram of a power amplifier.

conducts the current i_D , and the magnitude of i_D . This in turn is first dependent upon the bias voltage V_{bias} , and secondly upon the voltage input to the power amplifier v_{in} . The value of capacitor C_1 is set to be very large to ensure that there is no dc component seen at the output of the device, and the elements L_2 and C_2 form a tank circuit that determines the frequency ($i_{\text{rf}} = I_{\text{rf}} \sin \omega_0 t$, $\omega_0 = 1/\sqrt{L_2 C_2}$) of the output signal.

The transistor operates in one of three possible states depending upon the bias voltage, V_{bias} , and the power amplifier input signal, v_{in} . When the sum of the bias and input voltages is less than the threshold voltage of the transistor, no current flows through the transistor ($i_D = 0$) and the transistor is in its ‘cut-off’ state. When the sum of the bias and input voltages is greater than the threshold voltage, the transistor is said to become ‘active’ and current flows through the transistor ($i_D > 0$). In the ‘active’ state, the current i_D is linearly dependent upon the voltage v_{in} . Finally, in the ‘saturation’ state, the transistor conducts current but does not match a linear increase in input voltage, v_{in} , with a linear increase in current i_D . In summary these states are:

cut-off	$V_{\text{bias}} + v_{\text{in}} < V_T$	$i_D = 0$
active	$V_{\text{bias}} + v_{\text{in}} \geq V_T$	$i_D = g_m(V_{\text{bias}} + v_{\text{in}} - V_T)$
saturation	$V_{\text{bias}} + v_{\text{in}} \geq V_T$	$i_D = V_{DD}/R_L$

The output of the power amplifier is determined by the magnitude and portion of time that the transistor conducts the current i_D . The tank circuit shown in Figure 1.3 (elements L_2 and C_2) filters any harmonics generated when current i_D flows and ceases to flow so that the output power amplifier voltage is given by

$$v_{\text{out}} = I_{\text{fund}} R_L \sin(\omega_0 t), \quad (1.22)$$

where I_{fund} is given by

$$I_{\text{fund}} = \frac{2}{T} \int_0^T i_D \sin(\omega_0 t) dt \quad (1.23)$$

Amplifier Classes

The class to which the power amplifier belongs is dependent upon the value of the voltage V_{bias} . A Class A amplifier is characterized by $V_{\text{bias}} \geq V_T + |v_{\text{in}}|$, (i.e. transistor is always conducting). A Class AB amplifier is produced when $V_{\text{bias}} > V_T$, (i.e. the transistor conducts more than half of every period). A Class B amplifier is produced when $V_{\text{bias}} = V_T$. In this case the input signal voltage must be greater than zero ($v_{\text{in}} > 0$) for the transistor to conduct, (i.e. the transistor conducts current for half of every period). A Class C amplifier is characterized by $V_{\text{bias}} < V_T$. In this case the transistor conducts current when $v_{\text{in}} > V_T - V_{\text{bias}}$ (i.e. the transistor conducts less than half of every period).

Figure 1.4 shows the current through the transistor for Class A, AB, and C power amplifiers. The portion of the period for which the transistor conducts can also be used to characterize a power amplifier, and is denoted as the conduction angle, 2ϕ . The conduction

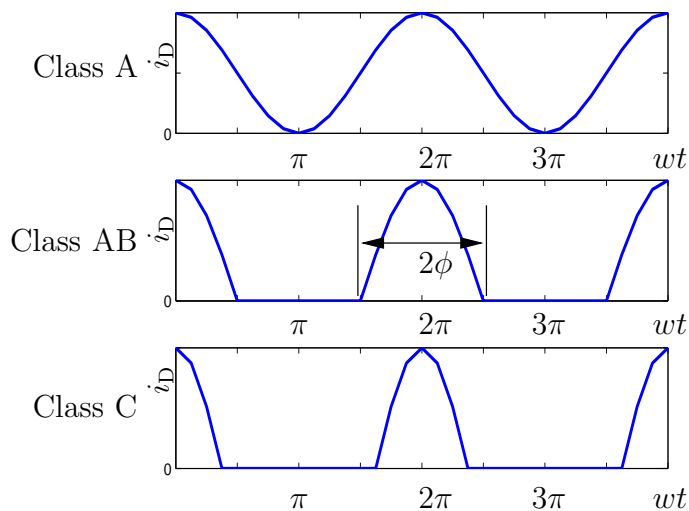


Figure 1.4: The transistor current of Class A, Class AB, and Class C power amplifiers.

angles for Class A, and B power amplifiers are $\phi = \pi$, and $\phi = \pi/2$, respectively. The conduction angles for Class AB and C power amplifier are dependent upon the input voltage v_{in} , and i_D and vary in the ranges $\pi > \phi > \pi/2$, and $\phi < \pi/2$, respectively.

Amplifier Linearity

The conduction angle can be used to re-express the current at the output of the power amplifier, I_{fund} , as

$$\begin{aligned}
 I_{fund} &= \frac{2}{T} \int_0^T i_D \sin(w_0 t) dt \\
 &= \frac{I_{rf}}{2\pi} [2\phi - \sin 2\phi]
 \end{aligned} \tag{1.24}$$

Thus, when operating as a Class A ($\phi = \pi$) or Class B ($\phi = \pi/2$) amplifier, the output current is linearly dependent upon I_{rf} in the ‘active’ range of the transistor. However, when operating as a Class AB ($\phi > \pi/2$) or C ($\phi < \pi/2$) amplifier, the output is no longer a linear function of the input, v_{in} , because the conduction angle changes with the amplitude

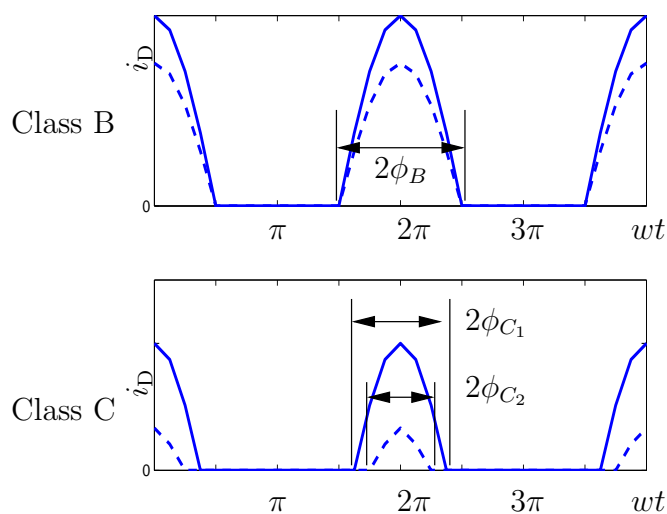


Figure 1.5: The conduction angle of Class B and Class C amplifiers.

of I_{rf} , see Figure 1.5. In fact, a true Class B power amplifier is also not realizable because the abrupt on/off characteristic is not possible with a practical transistor. Therefore the conduction angle of a practical Class B power amplifier is not exactly $\phi = \pi/2$ and a practical Class B amplifier is not truly linear. Additionally, all classes of power amplifier are non-linear when the input voltage is large and the transistor operates near or at saturation. In fact, operation in this region causes significant distortion, and performance degradation for non-constant envelope modulations. For this reason, non-constant envelope modulation schemes often employ a ‘back-off’ region, i.e. these schemes never transmit at the maximum output power of the power amplifier.

Amplifier Efficiency

Often power amplifiers are characterized in the literature by a performance criterion called *drain efficiency*. Drain efficiency is the ratio of transmitted power to dc input power, where transmitted power is given by $P_{out} = I_{fund}^2 R_L / 2$, and dc input power is given by

$P_{\text{dc}} = V_{\text{DD}}\bar{i}_{\text{D}}$. The dc component of i_{D} is

$$\begin{aligned}\bar{i}_{\text{D}} &= \frac{1}{2\pi} \int_{-\phi}^{\phi} (I_{\text{DC}} + I_{\text{rf}} \cos \theta) d\theta \\ &= \frac{I_{\text{rf}}}{\pi} (\sin \phi - \phi \cos \phi).\end{aligned}\tag{1.25}$$

Thus the drain efficiency can be written as [28, Chap 15.]

$$\begin{aligned}\eta &= \frac{P_{\text{out}}}{P_{\text{dc}}} \\ &= \frac{\pi I_{\text{rf}} R_L [2\phi - \sin 2\phi]^2}{8V_{\text{DD}} (\sin \phi - \phi \cos \phi)}.\end{aligned}\tag{1.26}$$

The drain efficiency of an amplifier is a function of I_{rf} , which is dependent upon the input voltage v_{in} . Therefore, it is common to characterize and compare different classes of amplifiers by their peak drain efficiency (i.e. when the maximum amount of power is being transmitted). In this case $I_{\text{fund}} = V_{\text{DD}}/R_L$ determines that $I_{\text{rf}} = 2\pi V_{\text{DD}}/(R_L[2\phi - \sin 2\phi])$, which yields

$$\eta_{\text{max}} = \frac{[2\phi - \sin 2\phi]}{4(\sin \phi - \phi \cos \phi)}\tag{1.27}$$

Using the above expression, the values for peak drain efficiency that are usually quoted in the literature are $1/2$, $\pi/4$, and a function of ϕ for Class A, B, and C amplifiers, respectively. Theoretically the maximum drain efficiency of a Class C amplifier can approach one ($\eta_{\text{max}} \rightarrow 1$), however for this to happen the peak value of the transistor current must approach infinity ($|i_{\text{D}}|_{\text{max}} \rightarrow \infty$). Although, these values are often used in the literature they do not give a full picture of the performance of an amplifier. Average drain efficiency values are often very different from the maximum efficiency values, which assume operation in the ‘saturation’ region of the power amplifier. For example [29] finds the average drain efficiency for multi-carrier signals with a 10 dB peak-to-average power ratio to be

5 and 28 percent for ideal Class A and Class B power amplifiers. In addition, the drain efficiency metric does not account for the input signal power (at the v_{in} source). Several other efficiency measures have been proposed. Here, we will list two of the alternatives to drain efficiency. The first is *power added efficiency*, which is given by

$$\text{PAE} = \frac{P_{\text{out}} - P_{\text{in}}}{P_{\text{dc}}}, \quad (1.28)$$

where P_{in} is the signal power supplied to the power amplifier (i.e at v_{in}). The second efficiency measure is *total efficiency*, which is given by

$$\eta_T = \frac{P_{\text{out}}}{P_{\text{dc}} + P_{\text{in}}}. \quad (1.29)$$

1.3 Contributions and Organization

The main goal of this thesis is to combine ST coding with CPM to produce a flexible, low complexity, energy efficient transmission format. This thesis proposes:

- A block-based orthogonal ST code for CPM (Chapter 2).
- A block-based diagonal ST code for CPM with a low-complexity non-coherent receiver (Chapter 2).
- A distributed ST code for CPM for use in uncoordinated cooperative networks (Chapter 3).
- A serially concatenated ST-CPM code (Chapter 4).

More specifically, in Chapter 2, we present two ST-CPM coding schemes. The first ST-CPM code employs a simple burst-based approach that allows for the straightforward

combination of any CPM format with orthogonal designs (ODs) [11],[30]. The resulting orthogonal ST block code (OSTBC) can use the same detection techniques at the receiver as are used for single-antenna transmission after an appropriate combining at the receiver. The proposed OSTBC scheme entails a lower complexity than all previously proposed ST coding schemes for CPM and yields a better performance for the important case of $N_T = 2$ transmit antennas. The second ST-CPM code is inspired by differential space-time modulation (DSTM) using diagonal signal matrices, which was devised for linear modulations by Hughes in [31] and by Hochwald and Sweldens in [32]. The resulting diagonal block ST-CPM (DBST-CPM) code enables non-coherent detection without channel state information (CSI). Further, a low-complexity receiver design is proposed that includes branch metrics for reduced-state non-coherent sequence detection and for different fading channels. We derive an upper bound for the frame error rate (FER) of DBST-CPM, and employ the bound in an efficient algorithm to find optimal DBST-CPM codes.

The proposed DBST-CPM code is employed in both Chapter 3 and Chapter 4. In Chapter 3 the DBST-CPM forms the basis of a distributed ST-CPM code. The distributed ST codes are designed to operate in wireless networks containing a large set of nodes, of which only a small *a priori* unknown subset will be active at any time. The devised distributed ST-CPM scheme combines the DBST-CPM code, (commonly assigned to all relay nodes) with signature vectors (uniquely assigned to nodes). We propose a numerical method for the optimization of signature vectors sets and show that the performance of the proposed distributed ST-CPM scheme is close to that achievable with co-located antennas. The decoding complexity of the proposed scheme is shown to be independent of the number of active relay nodes, and non-coherent receiver implementations, which do not require channel estimation, are applicable. In the second portion of this chapter, the energy consumption of the proposed distributed ST-CPM scheme is compared with

that of a distributed ST linear modulation (LM) scheme. The distributed ST schemes are compared using the total energy (radiated and used in hardware) required to supply a target bit error rate (BER) at a maximum transmission distance. The distributed ST-CPM scheme is shown to outperform the distributed ST-LM scheme for all but short-range transmission and performance gains are shown to increase with the number of active relay nodes.

Finally, in Chapter 4, a serially concatenated code for ST-CPM is proposed. The concatenated code consists of the diagonal signalling matrix from Chapter 2 as the inner code, and a class of double parity check (DPC) codes as the outer code. We employ extrinsic information transfer (EXIT) charts to select the best CPM symbol labelings for the diagonally-structured ST-CPM code. We outline a method for estimating the capacity of the underlying ST-CPM scheme in additive white Gaussian noise (AWGN) and derive an expression for the outage probability over a quasi-static fading channel (QSFC) in order to evaluate the merit of the proposed code. The resulting concatenated codes that are formed from the ST-CPM code and a DPC code are shown to provide performance close to capacity, and to provide performance superior to that provided by the more common combination of CPM, or ST-CPM schemes with convolutional codes.

Chapter 2

Space-Time Coding for CPM

Space-time coding is widely recognized as an effective means to combat the effects of multipath fading in wireless communications. Numerous space-time codes (STCs), which can broadly be classified into space-time block codes (STBCs) and space-time trellis codes (STTCs), have been proposed in the literature, cf. e.g. [33]. Almost all existing STC designs consider linear and thus, in general, non-constant envelope modulation formats. However, as previously discussed, constant envelope modulation formats such as continuous-phase modulation (CPM) are particularly appealing for implementation in wireless devices due to their high power and bandwidth efficiency. In fact, CPM is used in many wireless communication systems such as Bluetooth and the Global System for Mobile Communication (GSM) because of these very properties.

In the past few years there has been an effort to extend the concept of space-time (ST) coding originally developed for linear modulations to CPM. Fairly general ST code design rules for CPM have been given by Zhang and Fitz [1]. However, the decoding complexity of the resulting ST-CPM scheme is exponential in the number of transmit antennas. Orthogonal ST coded CPM schemes with reduced decoding complexity have been proposed by Wang and Xia [15]. In this case, orthogonality is achieved by requiring that the CPM waveforms transmitted over different antennas fulfill certain constraints in neighboring symbol intervals. However, due to the inherent memory of CPM, the design of the orthogonal schemes in [15] is quite involved and, in general, their error performance is not as good as that of the schemes in [1].

The ST coding schemes in [1, 15] have the disadvantage that the phase trellis inherent to CPM has to be modified. Therefore, existing CPM receivers cannot directly be applied and new receivers specifically tailored for the adopted ST coding scheme have to be developed. Both [1] and [15] emphasize that, because of the phase continuity and the associated inherent memory of CPM signals, a straightforward combination of CPM and orthogonal designs (ODs) [11, 30] is *not* possible.

More recently, ST codes for simple CPM schemes have been proposed. Cavers [16] and Xian *et al.* [17] have introduced ST codes for minimum-shift keying (MSK). ST codes for the special cases of binary CPM were proposed by Ahmadi and Rao [18] and Zhao and Giannakis [19], and for CPFSK by Maw and Taylor [20]. It is worth pointing out that all previously proposed ST coding schemes for CPM can be classified as ST trellis codes.

The ST-CPM schemes listed above have been designed for quasi-static fading channels (QSFCs) with coherent detection assuming perfect channel state information (CSI) at the receiver. More recently, Pande *et al.* [3] proposed a non-coherent¹ receiver for the orthogonal STTC design with full response CPM in [15, 34], and Pancaldi and Vitetta [2] considered ST CPFSK and non-coherent detection.

In this chapter, we propose two ST coding schemes for CPM. The first scheme shows that CPM can be easily combined with ODs by using a burst-based approach. This is similar in spirit to time-reversal ST block coding [35] proposed for inter-symbol interference channels. However, in the considered case the time-reversal is not necessary since the memory is introduced by the modulation itself and not by the channel. The proposed burst-based orthogonal space-time block coding (OSTBC) scheme has the same advantages as symbol-by-symbol OSTBC for linear modulations. In particular, the proposed scheme can be applied to *any* existing CPM format and, after an appropriate ST combining at

¹For the sake of brevity, we will often omit the terms ‘with CSI’ and ‘without CSI’ and refer to respective receivers as ‘coherent’ and ‘non-coherent’ receivers, respectively.

the receiver, the same detection techniques as in case of single-antenna transmission can be used. The second scheme is a *general* design method suited for non-coherent detection. The scheme is inspired by differential space-time modulation (DSTM) using diagonal signal matrices, which was devised for linear modulations by Hughes in [31] and by Hochwald and Sweldens in [32]. The diagonal structure of the signal matrices (only one antenna transmits at any given time) results in relatively simple decision rules that provide high performance at low complexity for non-coherent transmission [31, 32]. In addition, the diagonal structure of the signal matrices results in a highly versatile ST scheme that can support any number of transmit and receive antennas, and any data rate. This flexibility and the efficient receiver implementations possible for DSTM have made this DSTM scheme successful despite the rate loss implicit in the diagonal structure. ST schemes employing diagonally structured signalling matrices are especially attractive for transmission of low data rates in non-coherent environments.

This chapter is organized as follows. In Section 2.1, the transmission model employed for both of the proposed ST-CPM schemes is introduced. In Section 2.2, the OSTBC for CPM based upon burst-based transmission is introduced. The section begins with an overview of ODs and the specifics of CPM for the OSTBC scheme. Then, the burst-based OSTBC for CPM is introduced. Its performance is analyzed in Section 2.2.5 and simulation results for the scheme are presented in Section 2.2.6. In Section 2.3 the ST-CPM scheme employing diagonal signal matrices is introduced. First, the specifics of CPM for this scheme are overviewed, and then the new DBST-CPM scheme and corresponding non-coherent receiver designs are presented. The performance bound and an optimization algorithm are given in Section 2.3.4. Numerical and simulation results are shown and discussed in Section 2.3.5. Finally, Section 2.4 concludes the chapter.

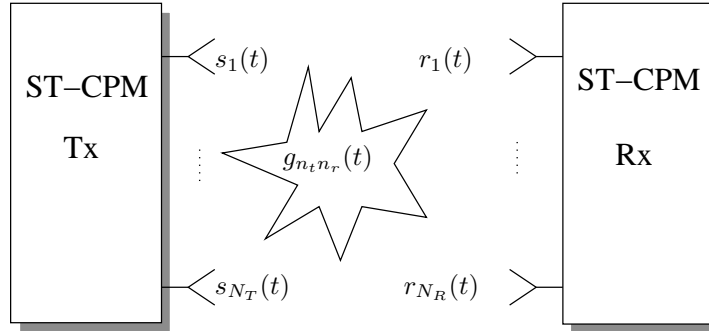


Figure 2.1: Transmitter and receiver model for CPM with burst-based OSTBC.

2.1 Transmission Model

The general ST-CPM system considered is assumed to be a multiple-input multiple-output (MIMO) transmission system with N_T transmit and N_R receive antennas as shown in Figure 2.1. All signals are represented by their complex baseband equivalents.

Let $s_{n_t}(t)$ denote the signal consisting of N_f symbols that is transmitted over antenna n_t , $1 \leq n_t \leq N_T$, during the time interval $0 \leq t < N_T N_f T$ (see Section 2.2.3 for further details on the structure of $s_{n_t}(t)$ and its relation to $x_{n_t}(t)$ for the proposed OSTBC scheme, and Section and 2.3.2 for the DBST-CPM scheme). The transmitted ST-CPM signal can be written as

$$\mathbf{S}(t, \mathbf{a}) = [s_1(t) \ s_2(t) \ \dots \ s_{N_T}(t)]^T. \quad (2.1)$$

The received signal, $\mathbf{r}(t) \triangleq [r_1(t) \ r_2(t) \ \dots \ r_{N_R}(t)]^T$ for N_R receive antennas, is given by

$$\mathbf{r}(t) = \mathbf{G}(t) \cdot \mathbf{S}(t, \mathbf{a}) + \mathbf{n}(t), \quad 0 \leq t < N_T N_f T, \quad (2.2)$$

where $\mathbf{n}(t) \triangleq [n_1(t) \ n_2(t) \ \dots \ n_{N_R}(t)]^T$ is the noise vector whose elements, $n_{n_r}(t)$, $1 \leq n_r \leq N_R$, denote independent additive white Gaussian noise (AWGN) processes with power spectral density \mathcal{N}_0 , and where $\mathbf{G}(t)$ is an $N_R \times N_T$ matrix that contains the elements $g_{n_r n_t}(t)$, $1 \leq n_t \leq N_T$, $1 \leq n_r \leq N_R$, which denote the channel gains between transmit antennas n_t and receive antennas n_r at time t . We will assume that the channel is constant

for at least one symbol period T , thus $\mathbf{G}(t)$ is equal to $\mathbf{G}[n] \triangleq \mathbf{G}(nT)$ for $nT \leq t \leq (n+1)T$, $0 \leq n < N_T N_f$.

In this thesis, we will consider three popular and practically relevant channel models: quasi-static fading, quasi-static fading with phase noise, and continuous fading.

Quasi-Static Fading Channel (QSFC): The QSFC model is often used for the design and analysis of space-time coded systems, cf. e.g. [36, 37, 38]. The QSFC model dictates that the channel is constant for one frame and changes independently from frame to frame. Accordingly, the channel coefficients (elements of $\mathbf{G}[n]$) for the QSFC can be written as

$$g_{n_t n_r}[n] = f_{n_t n_r}, \quad 0 \leq n < N_f. \quad (2.3)$$

We assume that the $f_{n_t n_r}$ are independently and identically distributed zero-mean complex Gaussian random variables with unit-variance, i.e., we consider a Rayleigh QSFC, cf. e.g. [36, 37, 38].

QSFC with Phase Noise: An extension of the above model takes into account phase noise due to carrier frequency instabilities caused by low-cost local oscillators. A common model for the phase noise process $\theta_{n_t n_r}[n]$ is the random-walk (Wiener) model [39]

$$\theta_{n_t n_r}[n] = \theta_{n_t n_r}[n-1] + \Delta_{n_t n_r}[n], \quad (2.4)$$

where $\Delta_{n_t n_r}[\cdot]$ is a white Gaussian process with variance σ_Δ^2 . The resulting channel coefficients are the product of phase noise and quasi-static fading and are given by

$$g_{n_t n_r}[n] = e^{j\theta_{n_t n_r}[n]} f_{n_t n_r}, \quad 0 \leq n < N_f. \quad (2.5)$$

We note that, while phase noise is irrelevant or, by definition, not present for (idealized) coherent detection, the QSFC-with-phase-noise model is practically relevant and an important benchmark model for non-coherent detection.

Continuous Fading Channel: Another generalization of the QSFC model is the case of continuous fading, where the channel coefficients are samples of a discrete-time random process

$$g_{n_t n_r}[n] = f_{n_t n_r}[n], \quad 0 \leq n < N_f. \quad (2.6)$$

We assume that the $f_{n_t n_r}[n]$ are spatially uncorrelated zero-mean complex Gaussian (Rayleigh fading) random processes with autocorrelation function, $\varphi_{ff}[\kappa]$, according to Clarke's model [40]

$$\varphi_{ff}[\kappa] \triangleq \mathcal{E}\{f_{n_t n_r}^*[n]f_{n_t n_r}[n + \kappa]\} = J_0(2\pi B_f T \kappa), \quad (2.7)$$

where $J_0(\cdot)$ and B_f are the the zeroth order Bessel function of the first kind and the one-sided bandwidth of the continuous-time fading process, respectively. As already implicit in (2.7), all $N_T N_R$ fading processes are assumed to have identical temporal correlations.

2.2 Burst-Based OSTBC for CPM

In this section, we introduce the proposed burst-based OSTBC scheme for CPM. We begin with a brief review complex ODs and overview the specifics of the CPM used for this ST scheme. Next, we present the considered transmission model and discuss the ST forming at the transmitter. Then, we show that an appropriate ST combining at the receiver enables single-input single-output (SISO) maximum-likelihood (ML) detection.

2.2.1 Complex Orthogonal Designs (ODs)

The complex ODs $\mathcal{O}(\mathbf{x})$ [30], $\mathbf{x} \triangleq [x_1, x_2, \dots, x_{N_C}]^T$, $N_C \leq N_T$, for N_C data symbols x_{n_c} , $1 \leq n_c \leq N_C$, considered in this chapter are $N_S \times N_T$ matrices with entries $\pm x_{n_c}$, $\pm x_{n_c}^*$, and 0. ODs with entries that are the sum or difference of different x_{n_c} or $x_{n_c}^*$ are not allowed, because of the constant envelope requirement of the transmit signal. The elements of $\mathcal{O}(\mathbf{x})$ are transmitted over the N_T transmit antennas in N_S symbol intervals and the code rate is

$R_C \triangleq N_C/N_S$. All ODs have the property $\mathcal{O}^H(\mathbf{x})\mathcal{O}(\mathbf{x}) = (\sum_{n_c=1}^{N_C} |x_{n_c}|^2)\mathbf{I}_{N_T}$ [30]. Popular examples are Alamouti's code [11] ($N_T = 2$) and the OD in [41, Eq. (22)] ($N_T = 4$), which are given by

$$\mathcal{O}(\mathbf{x}) \triangleq \begin{bmatrix} x_1 & x_2 \\ -x_2^* & x_1^* \end{bmatrix} \quad (2.8)$$

and

$$\mathcal{O}(\mathbf{x}) \triangleq \begin{bmatrix} x_1 & x_2 & x_3 & 0 \\ -x_2^* & x_1^* & 0 & -x_3 \\ -x_3^* & 0 & x_1^* & x_2 \\ 0 & x_3^* & -x_2^* & x_1 \end{bmatrix}, \quad (2.9)$$

respectively. Alamouti's code has rate $R_C = 1$, whereas the OD in [41, Eq. (22)] has rate $R_C = 3/4$. Note that all entries in the same column of $\mathcal{O}(\mathbf{x})$ are transmitted over the same antenna, whereas all entries in the same row are transmitted at the same time.

2.2.2 Continuous-Phase Modulation (CPM) Specifics

For the proposed OSTBC scheme N_C CPM waveforms $x_{n_c}(t)$, $1 \leq n_c \leq N_C$, are required [42]

$$x_{n_c}(t) = \sqrt{\frac{E_s}{T}} \exp\left(j2\pi h \sum_{i=0}^{N_B+N_E-1} a_{n_c}[i]q(t-iT)\right), \quad (2.10)$$

where E_s , T , N_B , and N_E denote the energy per symbol, the symbol duration, the number of data symbols, and the number of termination symbols, respectively, and $N_f = N_B + N_E$. The symbols $a_{n_c}[i] \in \mathcal{A}$, $0 \leq i \leq N_B - 1$, are independent, identically distributed (i.i.d.) M -ary data symbols taken from the alphabet $\mathcal{A} = \{-M+1, -M+3, \dots, M-1\}$, whereas the symbols $a_{n_c}[i] \in \mathcal{A}$, $N_B \leq i \leq N_B + N_E - 1$, are known to the receiver and necessary for termination of the CPM trellis for decoding. Note that we assume in Eq. (2.10) that the same CPM format is used for all n_c , $1 \leq n_c \leq N_C$. This restriction is not necessary

and only made to simplify the exposition.

2.2.3 Proposed OSTBC Scheme

As pointed out in [1, 15], the straightforward application of ODs on a symbol-by-symbol level is not possible because of the continuous-phase requirement and the associated memory of CPM. In order to avoid this problem, we propose a simple burst-based OSTBC scheme, i.e., we replace the symbols x_{n_c} in the OD $\mathcal{O}(\mathbf{x})$ by the CPM waveforms $x_{n_c}(t)$, $1 \leq n_c \leq N_C$, of duration $T_B \triangleq (N_B + N_E)T$. The transmitted signals $s_{n_t}(t)$ are then simply the concatenation of the (appropriately normalized) entries of the n_t th column of $\mathcal{O}(\mathbf{x})$ separated by a small guard interval of duration T_G . The guard interval is used to minimize the impact of the transition from one entry of $\mathcal{O}(\mathbf{x})$ to the next on the power spectrum of the transmit signal. For this purpose the amplitude of $s_{n_t}(t)$ may be first slowly decreased to zero, before the amplitude and phase of $s_{n_t}(t)$ are slowly changed to the values prescribed by the next entry of $\mathcal{O}(\mathbf{x})$. This procedure is similar to what is done in the GSM system where a guard interval of 8.25 symbols is inserted after every data burst. In general, T_G should be chosen long enough to make the effects of the transition from one entry of $\mathcal{O}(\mathbf{x})$ to the next on the transmit power spectrum negligible. Although the optimum value for T_G will depend on the particular CPM scheme employed, in practice, $N_E T \leq T_G \leq 2N_E T$ should give satisfactory results.

Taking the guard interval into account, the duration of $s_{n_t}(t)$ is $N_S T_{\text{tot}}$ with $T_{\text{tot}} \triangleq T_B + T_G$. The data rate in bits per channel use of the proposed OSTBC scheme is

$$R = \frac{N_C N_B T}{N_S T_{\text{tot}}} \log_2(M). \quad (2.11)$$

Throughout this section we will assume $N_E \ll N_B$ and $T_G \ll T_B$, in which case the data rate simplifies to $R \approx R_C \log_2(M)$.

To further illustrate the proposed OSTBC scheme, we consider the special case of $N_T = 2$ transmit antennas more in detail. We adopt the OD given by Eq. (2.8) and apply the technique described above to obtain the transmit signals $s_{n_t}(t)$, $n_t = \{1, 2\}$. Thus, taking into account the normalization of the transmit power, the transmitted signals are given by

$$s_1(t) = \begin{cases} \frac{1}{\sqrt{2}} x_1(t) & 0 \leq t \leq T_B \\ -\frac{1}{\sqrt{2}} x_2^*(t - T_{\text{tot}}) & T_{\text{tot}} \leq t \leq T_{\text{tot}} + T_B \end{cases} \quad (2.12)$$

$$s_2(t) = \begin{cases} \frac{1}{\sqrt{2}} x_2(t) & 0 \leq t \leq T_B \\ \frac{1}{\sqrt{2}} x_1^*(t - T_{\text{tot}}) & T_{\text{tot}} \leq t \leq T_{\text{tot}} + T_B \end{cases} \quad (2.13)$$

Obviously, $s_1(t)$ and $s_2(t)$ have constant envelopes and continuous phases for $0 \leq t \leq T_B$ and $T_{\text{tot}} \leq t \leq T_{\text{tot}} + T_B$.

For ODs with zero entries, cf. Eq. (2.9), the transmit signals $s_{n_t}(t)$ are zero in certain intervals. During these intervals the corresponding transmit antenna can be simply switched off. For example, for the OD with $N_T = 4$ in Eq. (2.9) antenna n_t does not transmit in the interval $(N_T - n_t)T_{\text{tot}} \leq t \leq (N_T - n_t + 1)T_{\text{tot}}$, $1 \leq n_t \leq N_T$. Again the guard interval can be used to achieve a smooth transition of the transmit signal between the zero and non-zero entries of $\mathcal{O}(\mathbf{x})$ making the effect on the transmit power spectrum negligible.

Although necessary in practice, for simplicity of exposition we will neglect the guard interval in the following and assume $T_G = 0$.

2.2.4 Maximum Likelihood (ML) Detection

Assuming perfect channel state information at the receiver, for ML detection of the data sequences $\mathbf{a}_{n_c} \triangleq [a_{n_c}[0], a_{n_c}[1], \dots, a_{n_c}[N_B - 1]]^T$, $1 \leq n_c \leq N_C$, we have to evaluate

$$\{\hat{\mathbf{a}}_1, \dots, \hat{\mathbf{a}}_{N_C}\} = \operatorname{argmin}_{\mathbf{a}_1, \dots, \mathbf{a}_{N_C}} \left\{ \sum_{n_r=1}^{N_R} \int_0^{N_s T_B} \left| r_{n_r}(t) - \sum_{n_t=1}^{N_T} g_{n_t n_r} s_{n_t}(t) \right|^2 dt \right\} \quad (2.14)$$

where $\hat{\mathbf{a}}_{n_c}$ denotes the estimate for \mathbf{a}_{n_c} , $1 \leq n_c \leq N_C$. The ML decision rule in Eq. (2.14) can be significantly simplified by exploiting the properties of ODs [30]. To illustrate this, we consider the $N_T = 2$ case and the OD in Eq. (2.8). Using Eqs. (2.12) and (2.13) the integral in Eq. (2.14) can be rewritten as

$$\begin{aligned} & \int_0^{T_B} \left| r_{n_r}(t) - \frac{1}{\sqrt{2}} [g_{1n_r} x_1(t) + g_{2n_r} x_2(t)] \right|^2 dt + \\ & \int_{T_B}^{2T_B} \left| r_{n_r}(t) - \frac{1}{\sqrt{2}} [-g_{1n_r} x_2^*(t - T_B) + g_{2n_r} x_1^*(t - T_B)] \right|^2 dt \\ & = \int_0^{T_B} \left| r_{n_r}(t) - \frac{1}{\sqrt{2}} [g_{1n_r} x_1(t) + g_{2n_r} x_2(t)] \right|^2 dt \\ & \quad + \int_{T_B}^{2T_B} \left| r_{n_r}(t) - \frac{1}{\sqrt{2}} [-g_{1n_r} x_2^*(t - T_B) + g_{2n_r} x_1^*(t - T_B)] \right|^2 dt. \end{aligned} \quad (2.15)$$

Applying Eq. (2.15) in Eq. (2.14) and omitting all irrelevant terms, the ML decision rule in Eq. (2.14) for \mathbf{a}_1 and \mathbf{a}_2 can be simplified to

$$\hat{\mathbf{a}}_{n_c} = \operatorname{argmin}_{\mathbf{a}_{n_c}} \left\{ \int_0^{T_B} |d_{n_c}(t) - x_{n_c}(t)|^2 dt \right\}, \quad (2.16)$$

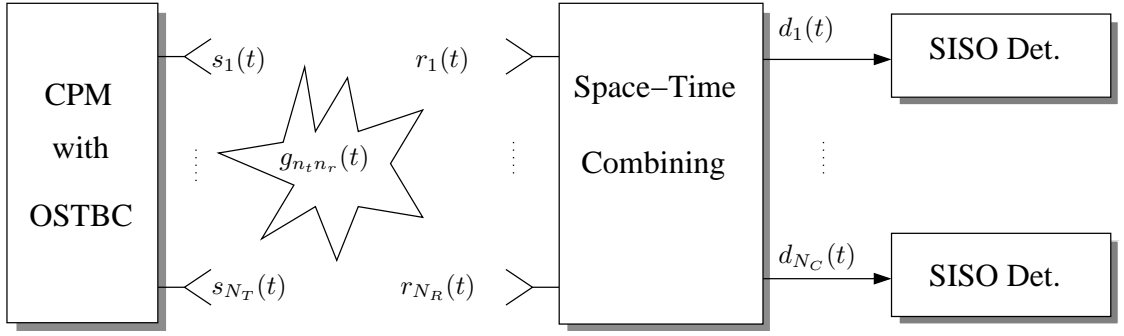


Figure 2.2: Transmitter and receiver model for CPM with burst-based OSTBC.

where $d_{n_c}(t)$ is given by

$$d_1(t) \triangleq \frac{1}{\sqrt{2}} \sum_{n_r=1}^{N_R} (g_{1n_r}^* r_{n_r}(t) + g_{2n_r} r_{n_r}^*(t + T_B)) \quad (2.17)$$

$$d_2(t) \triangleq \frac{1}{\sqrt{2}} \sum_{n_r=1}^{N_R} (g_{2n_r}^* r_{n_r}(t) - g_{1n_r} r_{n_r}^*(t + T_B)). \quad (2.18)$$

Note that irrelevant terms include terms such as $|x_1(t)|^2 |g_{1n_r}|^2$ and $|r_{n_r}(t)|^2 |g_{1n_r}|^2$ which do not affect the decision on \mathbf{a}_{n_c} . Also, note that terms such as $g_{1n_r}^* r_{n_r}(t) g_{2n_r}^* r_{n_r}(t + T_B)$ are zero terms. For ODs with $N_T > 2$, the ML decision rule for \mathbf{a}_{n_c} , $1 \leq n_c \leq N_C$, can also be simplified to Eq. (2.16) where $d_{n_c}(t)$ has the general form

$$d_{n_c}(t) \triangleq \frac{1}{\sqrt{N_C}} \sum_{n_t=1}^{N_T} \sum_{n_r=1}^{N_R} w_{n_t n_r}(n_c) f_{n_c n_t} \{ r_{n_r}(t + (n_t - 1)T_B) \}. \quad (2.19)$$

Here, $f_{n_c n_t} \{ \cdot \}$ is either the identity operator ($f_{n_c n_t} \{ x \} = x$) or the complex conjugation operator ($f_{n_c n_t} \{ x \} = x^*$). The coefficients $w_{n_t n_r}(n_c)$ can take on values $\pm g_{n_t n_r}$ and $\pm g_{n_t n_r}^*$, $1 \leq n_t, n_t' \leq N_T$, $1 \leq n_r \leq N_R$. Both $f_{n_c n_t} \{ \cdot \}$ and $w_{n_t n_r}(n_c)$ depend on the particular OD used and are identical to the respective operators and coefficients appearing in the decision variables for detection of phase-shift keying modulation with OSTBC, cf. e.g. [30].

Interestingly, the ML decision rule in Eq. (2.16) is identical to that for SISO CPM

transmission over an AWGN channel with *equivalent* received signal $d_{nc}(t)$, cf. Figure 2.2. Therefore, Eq. (2.16) can be implemented using any known optimum or sub-optimum method based on e.g. Laurent's representation [43] or Rimoldi's decomposition approach [25, 26] (see also Section 1.2). In contrast to the schemes in [1, 15, 16], there is no need to tailor new detectors for the proposed OSTBC method.

Eq. (2.14) shows that the fading channel has to be approximately constant for $N_S(N_B + N_E)$ symbol intervals. In contrast, for symbol-based OSTBC [11, 30] and the orthogonal ST coded CPM scheme in [15] the fading channel has to be approximately constant only for N_S symbol intervals. Since $N_B \gg 1$ is recommended to make the overhead due to the termination symbols and the guard interval negligible, the admissible fading variations for the proposed burst-based OSTBC scheme are considerably smaller than those for the non-CPM and the CPM schemes in [11, 30] and [1, 15, 16], respectively.

2.2.5 Performance Analysis

Bit Error Rate (BER)

Assuming SISO transmission over an AWGN channel, for high signal-to-noise ratios (SNRs) the BER of CPM can be approximated by [42]

$$\text{BER}(\bar{\gamma}_b) \approx K Q(d_{\min} \sqrt{\bar{\gamma}_b}), \quad (2.20)$$

where d_{\min} denotes the normalized minimum Euclidean distance between two possible bit sequences and K is a positive constant that accounts for the number of bit errors per error event and the dependence of the error event on the transmitted data. $Q(x) \triangleq \frac{1}{\sqrt{2\pi}} \int_x^\infty e^{-t^2/2} dt$ is the Gaussian Q -function and $\bar{\gamma}_b \triangleq E_b/\mathcal{N}_0$, where E_b denotes the received energy per bit.

On the other hand, for CPM with OSTBC with $N_T = 2$ transmit antennas, Eqs. (2.17) and (2.18) show that the equivalent received signal can be rewritten as

$$d_{n_c}(t) = \frac{1}{2} \sum_{n_r=1}^{N_R} (|g_{1n_r}|^2 + |g_{2n_r}|^2) x_{n_c}(t) + z(t), \quad (2.21)$$

where $z(t)$ is an AWGN process with power spectral density $\sum_{n_r=1}^{N_R} (|g_{1n_r}|^2 + |g_{2n_r}|^2) \mathcal{N}_0/2$. Therefore, the instantaneous SNR per bit is $\gamma_b = \sum_{n_r=1}^{N_R} (|g_{1n_r}|^2 + |g_{2n_r}|^2) E_b / (2\mathcal{N}_0)$.

For the general case of N_T transmit antennas and ODs with rate R_C , the instantaneous SNR per bit is

$$\gamma_b = \sum_{n_t=1}^{N_T} \sum_{n_r=1}^{N_R} |g_{n_t n_r}|^2 \frac{R_C E_b}{N_T \mathcal{N}_0}. \quad (2.22)$$

Therefore, using Eq. (2.20) and the alternative representation of the Q -function $Q(x) = \frac{1}{\pi} \int_0^{\pi/2} \exp[-x^2/(2 \sin^2 \theta)] d\theta$, $x \geq 0$ [44], the approximate BER of the proposed OSTBC scheme can be calculated to

$$\begin{aligned} \overline{\text{BER}} &\approx \int_{\mathbf{g}} \text{BER} \left(\sum_{n_t=1}^{N_T} \sum_{n_r=1}^{N_R} |g_{n_t n_r}|^2 \frac{R_C E_b}{N_T \mathcal{N}_0} \right) p_{\mathbf{g}}(\mathbf{g}) d\mathbf{g} \\ &= \frac{K}{\pi} \int_0^{\pi/2} \left(1 + \frac{d_{\min}^2 R_C E_b}{2 N_T \mathcal{N}_0 \sin^2 \theta} \right)^{-N_T N_R} d\theta \end{aligned} \quad (2.23)$$

where $\mathbf{g} \triangleq [g_{11} \ g_{12} \ \dots \ g_{N_T N_R}]^T$ and $p_{\mathbf{g}}(\mathbf{g})$ is the joint probability density function of the elements of \mathbf{g} . Eq. (2.23) is easy to evaluate as only a one-dimensional numerical integration over a finite interval has to be performed.

Using the bound $Q(x) \leq 0.5 \exp(-x^2/2)$, $x \geq 0$, in Eq. (2.23), it is easy to show that the Chernoff bound on the approximate BER is given by

$$\overline{\text{BER}} \lesssim \frac{K}{2} \left(1 + \frac{d_{\min}^2 R_C E_b}{2 N_T \mathcal{N}_0} \right)^{-N_T N_R}. \quad (2.24)$$

Eq. (2.24) shows that the proposed burst-based OSTBC scheme for CPM achieves the maximum diversity order $N_T N_R$.

Frame Error Rate (FER)

To arrive at a meaningful expression for the FER, we have to assume that the bit errors are approximately statistically independent. However, whether the bit errors are independent or not depends on the particular CPM format used. For example, CPM with conventional phase-increment mapping [26] results in double errors due to the resulting differential encoding of the absolute phase. Fortunately, these double errors can be avoided if *phase-state mapping* is employed, (see Section 1.2 for details), which we adopt for the simulations in Section 2.2.6.

Assuming M -ary CPM transmission over an AWGN channel and approximately independent bit errors, the corresponding FER is given by

$$\text{FER}(\gamma_b) \approx 1 - (1 - \text{BER}(\gamma_b))^{\log_2(M)N_B}, \quad (2.25)$$

where $\text{BER}(\bar{\gamma}_b)$ is defined in Eq. (2.20). Combining Eqs. (2.22) and (2.25), the FER of CPM with OSTBC can be obtained from

$$\overline{\text{FER}} \approx \int_{\mathbf{g}} \text{FER} \left(\sum_{n_t=1}^{N_T} \sum_{n_r=1}^{N_R} |g_{n_t n_r}|^2 \frac{R_C E_b}{N_T \mathcal{N}_0} \right) p_{\mathbf{g}}(\mathbf{g}) d\mathbf{g}. \quad (2.26)$$

In the integrand in Eq. (2.26), the fading gains $g_{n_t n_r}$ only appear in the form $|g_{n_t n_r}|^2$. Therefore, the evaluation of Eq. (2.26) involves an $N_T N_R$ -dimensional numerical integration.

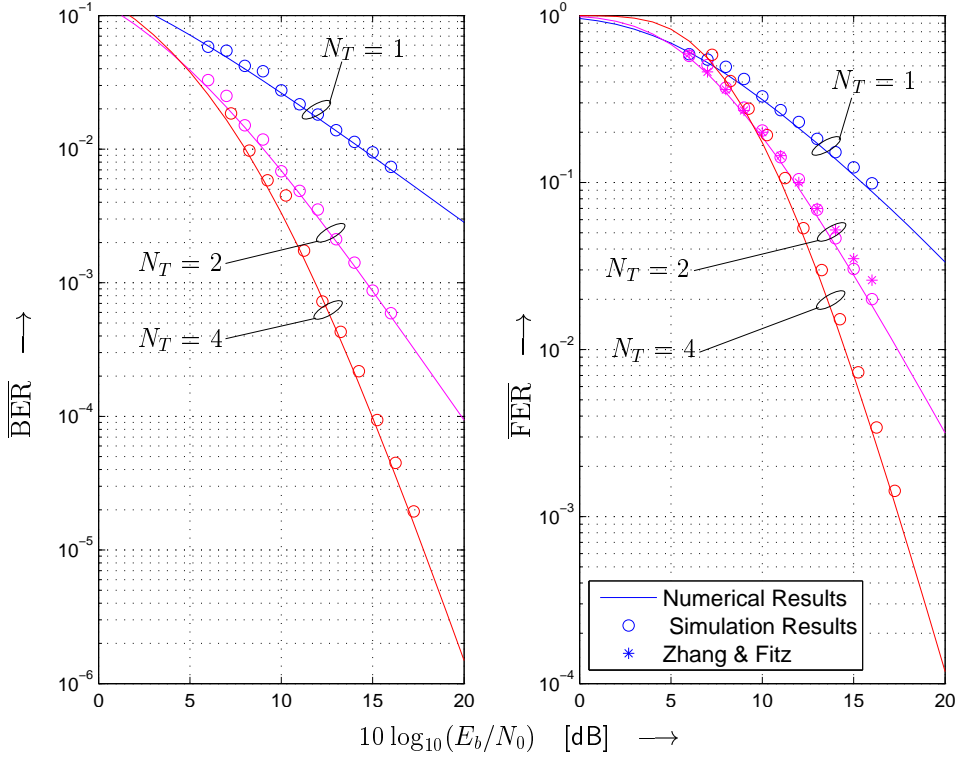


Figure 2.3: BER and FER vs. $10 \log_{10}(E_b/\mathcal{N}_0)$ of GMSK with phase-state mapping. Single-antenna transmission ($N_T = 1$), OSTBC ($N_T = 2$, $N_T = 4$), and the ST coding scheme of [1] ($N_T = 2$) are compared.

2.2.6 Performance Results

In this section, performance results are presented for $N_T = 2$ and $N_T = 4$ transmit antennas employing the ODs in Eq. (2.8). One receive antenna and a frame length of $N_B = 130$ is assumed in all cases. For comparison we also consider single-antenna transmission and the delay diversity (DD) scheme proposed in [1] for $N_T = 2$ transmit antennas. To facilitate the comparison, we adopt the same CPM schemes as [1]: GMSK with time-bandwidth product $BT = 0.3$, binary 2REC with $h = 1/2$, and 4-ary 1RC with $h = 1/4$. The derivative of $q(t)$ is a rectangular pulse of duration $2T$ and a raised-cosine pulse of duration T for 2REC and 1RC, respectively. Phase-state mapping [26] (see Section 1.2) is applied for all CPM

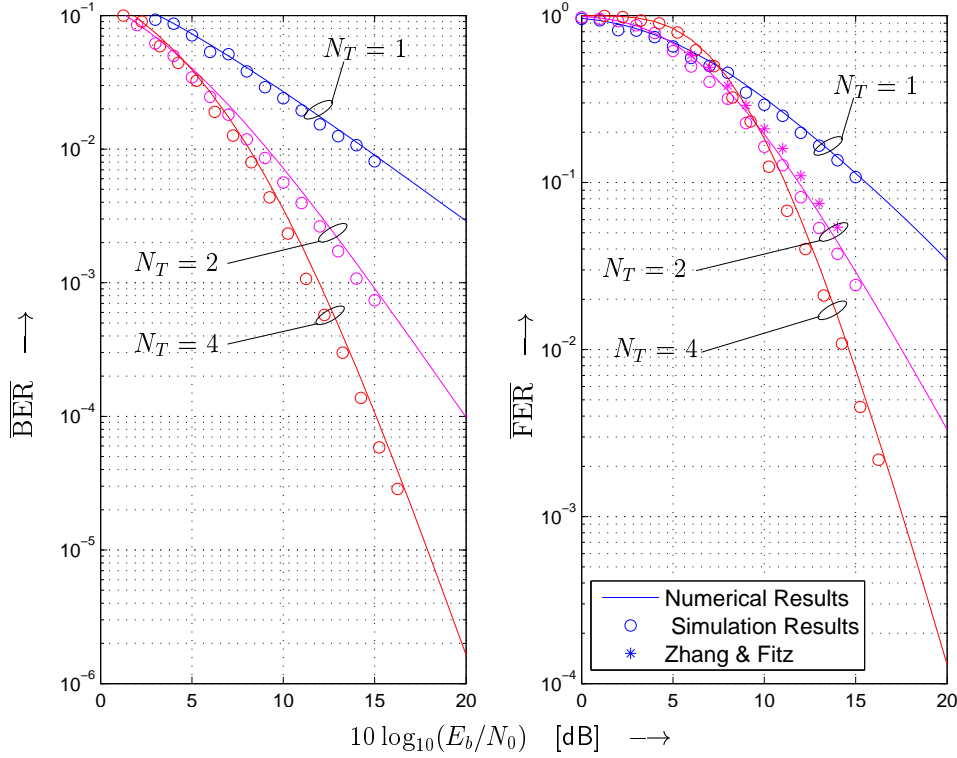


Figure 2.4: BER and FER vs. $10 \log_{10}(E_b/\mathcal{N}_0)$ of binary 2REC with phase-state mapping. Single-antenna transmission ($N_T = 1$), OSTBC ($N_T = 2$, $N_T = 4$), and the ST coding scheme of [1] ($N_T = 2$) are compared.

schemes, and as a result $K = 1$ was valid in all cases. Note that [1] employed CPM with phase-increment mapping. The resulting double errors affect the BER but not the FER. Therefore, the FER comparison between the scheme in [1] and the proposed approach in Figs. 2.3–2.5 is fair. The normalized squared minimum Euclidean distances of GMSK, binary 2REC, and 4-ary 1RC are $d_{\min}^2 = 1.77$, $d_{\min}^2 = 1.73$, and $d_{\min}^2 = 1.64$, respectively. For GMSK and binary 2REC the data rate is $R = 1$ bit/(channel use) for $N_T = 1$ and $N_T = 2$, and $R = 3/4$ bit/(channel use) for $N_T = 4$. For 4-ary 1RC $R = 2$ bit/(channel use) results for $N_T = 1$ and $N_T = 2$, and $R = 3/2$ bit/(channel use) for $N_T = 4$.

Figs. 2.3, 2.4, and 2.5 depict the BERs and FERs for GMSK, binary 2REC, and 4-ary

1RC, respectively. Simulation results (circles) and numerical results (solid lines) obtained by evaluating Eqs. (2.23) and (2.26) are in excellent agreement for both single-antenna CPM and CPM with OSTBC. Obviously, the proposed OSTBC scheme achieves a significant performance improvement compared to single-antenna transmission. For all considered CPM schemes with $N_T = 2$ the FERs of the DD scheme of [1] are slightly higher than the FERs of CPM with OSTBC.

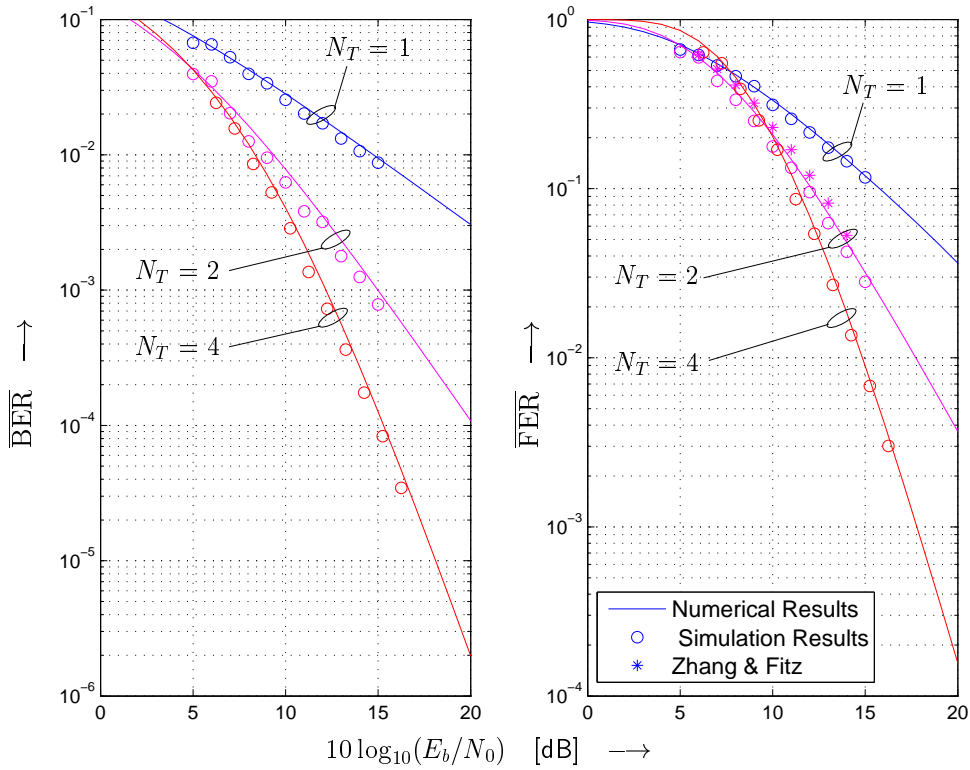


Figure 2.5: BER and FER vs. $10 \log_{10}(E_b/N_0)$ of 4-ary 1RC with phase-state mapping. Single-antenna transmission ($N_T = 1$), OSTBC ($N_T = 2$, $N_T = 4$), and the ST coding scheme of [1] ($N_T = 2$) are compared.

For the simulation of single-antenna CPM and CPM with OSTBC we adopted the reduced complexity detection technique proposed in [26]. For all considered examples, two receive filters and two (GMSK, binary 2REC) and four (4-ary 1RC) states for decoding

were sufficient to achieve close-to-optimum performance. Assuming optimum implementation, the complexity of the DD scheme of [1] is exponential in the number of transmit antennas and much higher than that of the proposed burst-based OSTBC approach. Unfortunately, it is not straightforward to design low-complexity receivers that preserve the diversity gain of optimum detection for DD and this problem was not discussed in [1].

For $N_T = 4$, a fair comparison with [1] is difficult because of the rate loss of complex ODs for $N_T > 2$ and the large differences in the required detection complexity. Furthermore, we note that the performance of the scheme proposed in [15] is not shown, since it is slightly worse than that of the scheme in [1], cf. [15, Figure 3].

2.3 Diagonal Block Space-Time (DBST) Coding for CPM

In this section, we introduce the second ST-CPM scheme that we proposed in this thesis. In order to preserve the constant envelope, continuous-phase properties of CPM for our ST-CPM scheme we once again elect to transmit blocks or frames of data rather than data symbols (each element in the signal matrix is now a CPM frame rather than a symbol as is used in DSTM for linear modulation formats). Careful design of the data mappings for each transmit frame produces a coding gain in addition to the expected diversity gain. The resulting diagonal block-based ST-CPM (DBST-CPM) scheme can (a) be used with any CPM format, (b) enable non-coherent detection, and (c) accommodate any number of transmit and receive antennas. (The flexibility of the proposed scheme is in notable contrast to other non-coherent ST-CPM schemes presented in the literature). In addition, this section presents receiver designs for non-coherent detection of DBST-CPM in three different fading environments, employing elements from per-survivor processing [45], linear

prediction-based decision-feedback differential detection (DFDD) for DSTM [46], and state reduction for CPM [26] to minimize detection complexity. Also in this section an efficient search algorithm is designed to find the optimal data mappings for our ST-CPM scheme. The applied data mappings are referred to as the *ST code*. (Optimization of the ST code is similar to optimization of the DSTM diagonal constellation parameters [31, 32], however due to the memory inherent to CPM ST code optimization requires a sequence-based approach.) Finally, a tight bound for the frame-error rate (FER) of DBST-CPM under is derived (under the assumption of coherent detection and a quasi-static fading channel (QSFC)) that is used as the basis for the optimization of DBST-CPM.

We begin with an introduction to the ST-code structure of our proposed DBST-CPM scheme, and then develop the receiver structure including decision rules for coherent and non-coherent detection for the fading channels considered before.

2.3.1 Continuous-Phase Modulation (CPM) Specifics

The proposed ST-CPM scheme employs N_T CPM waveforms [42]

$$x_{n_t}(t) = \sqrt{\frac{E_s}{T}} \exp \left(j2\pi h \sum_{i=0}^{N_f-1} a_{n_t}[i]q(t - iT) \right), \quad 0 \leq t < N_f T, \quad 1 \leq n_t \leq N_T, \quad (2.27)$$

where E_s , T , and N_f denote the energy per symbol, the symbol duration, and the frame length, which is the number of data-carrying symbols $a_{n_t}[i]$, respectively. The symbols $a_{n_t}[i]$ are taken from the alphabet $\mathcal{A} \triangleq \{-M + 1, -M + 3, \dots, M - 1\}$ of size M . For

later reference, we also introduce the vectors

$$\begin{aligned}
 \mathbf{a}_{n_t} &\triangleq [a_{n_t}[0] \ a_{n_t}[1] \ \dots \ a_{n_t}[N_f - 1]] , \\
 \mathbf{a}[i] &\triangleq [a_1[i] \ a_2[i] \ \dots \ a_{N_T}[i]] , \\
 \mathbf{a} &\triangleq [\mathbf{a}[0] \ \mathbf{a}[1] \ \dots \ \mathbf{a}[N_f - 1]] ,
 \end{aligned} \tag{2.28}$$

of, respectively, data symbols transmitted over antenna n_t , data symbols assigned to the N_T antennas during modulation interval i , and all data symbols in one frame.

Note that we assume in Eq. (2.27) that the same CPM format is used for all antennas n_t , $1 \leq n_t \leq N_T$. This restriction is not necessary, but it is made for the purpose of simplicity in this paper.

2.3.2 Modulation

Only one antenna transmits at any time when diagonal matrices are employed. If each antenna is used for transmission in N_f consecutive modulation intervals, phase continuity can be preserved for CPM without any additional signal processing or complicated design restrictions. Hence, the proposed ST-CPM scheme employs transmit signals [see Eq. (2.27) for $x_{n_t}(t)$]

$$s_{n_t}(t) = \begin{cases} x_{n_t}(t - (n_t - 1)N_f T), & (n_t - 1)N_f T \leq t < n_t N_f T , \\ 0 , & \text{otherwise,} \end{cases} \tag{2.29}$$

i.e., the N_T antennas $n_t = 1, \dots, N_T$ are used sequentially. Thus, we can write the ST-CPM signal matrix as

$$\mathbf{S}(t, \mathbf{a}) = \begin{bmatrix} x_1(t) & 0 & \cdots & 0 \\ 0 & x_2(t - N_f T) & \cdots & 0 \\ \vdots & & & \vdots \\ 0 & 0 & \cdots & x_{N_T}(t - (N_T - 1)N_f T) \end{bmatrix}. \quad (2.30)$$

It is interesting to note that the proposed ST-CPM scheme is similar in structure to “block DSTM” for linear modulation considered in [47, 48]. Therefore, we refer to the proposed scheme as DBST-CPM. Also similar to linear DSTM with diagonal matrices, the data vectors $\mathbf{a}[i]$ are chosen from an M -ary constellation and thus the data rate of DBST-CPM is $\log_2(M)/N_T$ bits per symbol duration T . The actual design of the M -ary set of data vectors $\mathbf{a}[i]$, i.e., the optimization of DBST-CPM, will be discussed in detail in Section 2.3.4.

As previously mentioned we have opted to transmit blocks of data to preserve the continuous-phase property of CPM, however, we would like to point out that, as for the OSTBC code proposed in the previous section, the transitions between blocks of data need *not* be considered a violation of the continuous-phase property, but rather they are similar to the transitions observed in *any* packet based transmission scheme, as for example the Global System for Mobile Communication (GSM), wireless local area network (WLAN) systems, Bluetooth, etc.

2.3.3 Detection

The receiver for DBST-CPM, similar to a single-antenna CPM receiver, is comprised of a bank of matched filters and a sequence detector [42], [25], [26].

Filtering and Sampling

If the reduced matched filter bank proposed in Section 1.2.1 is employed, the samples of the filtered received signal are D -dimensional vectors $\mathbf{r}_{n_r}[n] = [r_{n_r}^{(1)}[n], \dots, r_{n_r}^{(D)}[n]]^T$ with

$$r_{n_r}^{(d)}[n] = r_{n_r}(t) \otimes h_d^*(-t) \Big|_{t=nT}, \quad 0 \leq n < N_T N_f, \quad (2.31)$$

where \otimes denotes convolution.

Sequence Detection

Let us introduce the ‘address’ vector for ST-CPM as

$$\mathbf{d}[i] \triangleq [\Upsilon_1[i-L], \dots, \Upsilon_{N_T}[i-L], \mathbf{a}[i-L+1], \dots, \mathbf{a}[i]] \quad (2.32)$$

of L M -ary data symbols $\mathbf{a}[i]$ and N_T p -ary phase states $\Upsilon_{n_t}[i-L]$, which account for the accumulated phase due to past data symbols of the CPM signal transmitted over antenna n_t . Corresponding to the vector $\mathbf{d}[i]$ there are N_T signal elements $\rho_{n_t}(t, \mathbf{d}[i])$, each of which is transmitted over one antenna n_t in the interval $iT + (n_t - 1)N_f T \leq t < (i+1)T + (n_t - 1)N_f T$, $1 \leq n_t \leq N_T$, $0 \leq i < N_f$. Then, corresponding to the D receiver input filters, the sequence detector stores D -dimensional vectors $\boldsymbol{\rho}_{n_t}(\mathbf{d}[i])$, which represent the decorrelated coordinates of $\rho_{n_t}(t, \mathbf{d}[i])$ with respect to the ‘basis’ functions given in Eq. 1.20). More specifically, we have

$$\boldsymbol{\rho}_{n_t}(\mathbf{d}[i]) = \mathbf{C}^{-1} \int_0^T \mathbf{h}^*(t) \rho_{n_t}(t, \mathbf{d}[i]) dt, \quad (2.33)$$

where \mathbf{C} was given in Eq. (1.21).

Depending on the ST code of DBST-CPM (see Section 2.3.4 for the details about the ST

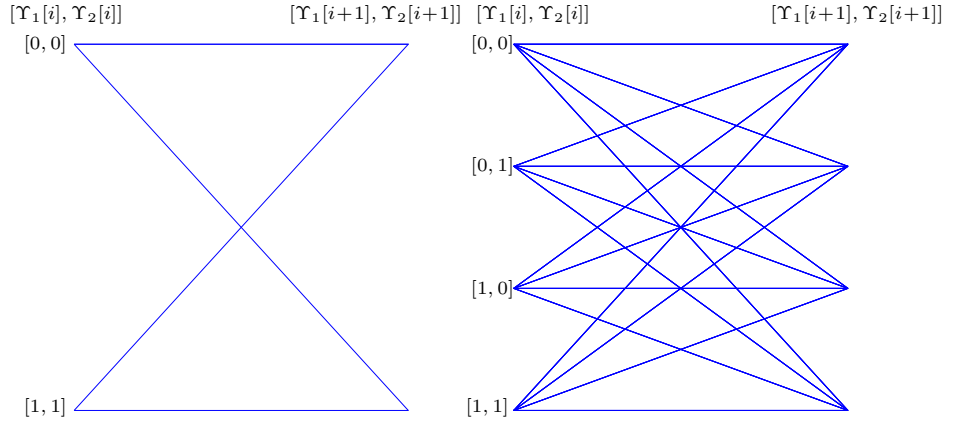


Figure 2.6: Trellis of DBST-CPM for $N_T = 2$ and CPM with 1REC pulse, $M = 4$, and $h = 1/2$. Left: Repetition ST code. Right: Optimal ST code (see Section 2.3.4 for details about ST code optimization).

code) the number of possible CPM phase state vectors $[\Upsilon_1[i], \dots, \Upsilon_{N_T}[i]]$ varies between p and p^{N_T} , and hence the number of states of the trellis representing the DBST-CPM signal varies between pM^{L-1} and $p^{N_T}M^{L-1}$. An illustration of this effect is given in Figure 2.6, which shows two trellises for DBST-CPM with $N_T = 2$, 1REC pulse, i.e., a rectangular frequency pulse $g(t)$ with $L = 1$, $M = 4$, $h = 1/2$, and two different ST codes. As can be seen, the number of states is $pM^{L-1} = 2$ for one ST code and $p^{N_T}M^{L-1} = 4$ for the other.

For sequence detection we adopt the classical Viterbi algorithm [49] operating on the DBST-CPM trellis with path metrics $\Psi_\mu[i]$ for each state μ at data-symbol interval i , and the path-metric update

$$\Psi_\nu[i + 1] = \Psi_\mu[i] + \psi_{\mu\nu}[i], \quad (2.34)$$

where $\psi_{\mu\nu}[i]$ denotes the metric for the branch leaving from state μ and ending in state ν during the i th data-symbol interval. Next, we will discuss the design of $\psi_{\mu\nu}[i]$ for coherent and non-coherent sequence detection.

A) Coherent Detection: Although our ultimate goal is the application of detection without CSI, it is useful for later optimization of DBST-CPM and performance comparison

to first consider the coherent detector. The maximum likelihood sequence detector (MLSD) for coherent detection of DBST-CPM cross-correlates the filtered received samples with the vectors $\boldsymbol{\rho}_{n_t}(\mathbf{d}[i])$ multiplied by the respective channel gains, and sums over all N_R receive antennas and all N_T transmit antennas. The branch metric reads

$$\psi_{\mu\nu}[i] = \sum_{n_t=1}^{N_T} \sum_{n_r=1}^{N_R} \operatorname{Re} \left\{ \mathbf{r}_{n_r}^H [i + (n_t - 1)N_f] \boldsymbol{\rho}_{n_t}(\mathbf{d}_{\mu\nu}[i]) g_{n_t n_r} [i + (n_t - 1)N_f] \right\}, \quad 0 \leq i < N_f, \quad (2.35)$$

where $\mathbf{d}_{\mu\nu}[i]$ is the address vector corresponding to the transition from state μ to ν and $\operatorname{Re}\{\cdot\}$ denotes the real part of a complex number.

B) Non-coherent Detection: Because the DBST-CPM data symbols $a_{n_t}[i]$ are inherently differentially encoded (see Eq. (2.27) and note that $q(t) = 1/2$ for $t \geq LT$), the ST-CPM signal is invariant to phase rotations and non-coherent sequence detection is directly applicable, cf. e.g. [50, 51]. In order to avoid an increase in the number of trellis states compared to coherent detection, we make use of ideas from per-survivor processing (PSP) [45] and decision-feedback differential detection (DFDD) for DSTM [46]. In particular, we propose to implicitly estimate the channel using per-state reference symbols $\eta_{\mu, n_r, n_t}[i]$ constructed as

$$\eta_{\mu, n_r, n_t}[i] = \sum_{k=1}^{N_d-1} l_k \mathbf{r}_{n_r}^T [i - k + (n_t - 1)N_f] \boldsymbol{\rho}_{n_t}^* (\tilde{\mathbf{d}}_{\mu}[i - k]), \quad (2.36)$$

where $[\tilde{\mathbf{d}}[i - N_d + 1], \dots, \tilde{\mathbf{d}}[i - 1]]$ are the $N_d - 1$ tentative (PSP) decisions corresponding to the path ending in state μ (cf. [45]) and $\mathbf{l} = [l_1 l_2 \dots l_{N_d-1}]$ are the coefficients of a linear minimum mean-square error (MMSE) predictor for the fading-plus-noise process, cf. e.g. [46, 52] for linear modulation. Note that only $N_d - 1$ previous symbols $\tilde{\mathbf{d}}[i - k]$ are used to form the reference in order to limit the complexity of the receiver. The branch metric

for non-coherent detection of DBST-CPM reads

$$\psi_{\mu\nu}[i] \triangleq \sum_{n_t=1}^{N_T} \sum_{n_r=1}^{N_R} \text{Re} \{ \mathbf{r}_{n_r}^H [i + (n_t - 1)N_f] \boldsymbol{\rho}_{n_t}(\mathbf{d}[i]) \eta_{\mu, n_r, n_t}[i] \} . \quad (2.37)$$

If the statistics of the fading process $g_{n_t n_r}[n]$ are known *a priori*, the predictor coefficients l_k can be calculated from the Yule-Walker equation [53]

$$\mathbf{l} = \mathbf{R}^{-1} \mathbf{p} , \quad (2.38)$$

where \mathbf{R} is a Toeplitz matrix, whose first row is given by $[\varphi_{gg}[0] + \sigma_n^2, \varphi_{gg}[1], \dots, \varphi_{gg}[N_d - 2]]$, $\mathbf{p} = [\varphi_{gg}[1] \varphi_{gg}[2] \dots \varphi_{gg}[N_d - 1]]^T$, and $\sigma_n^2 \triangleq \mathcal{N}_0/T$, $\phi_{gg}[\kappa] \triangleq \mathcal{E}\{g_{n_r n_r}^*[n] g_{n_r n_r}[n + \kappa]\}$. For the three channel models introduced in Section 2.1 we have (a) QSFC: $\varphi_{gg}[\kappa] = 1$, (b) QSFC with phase noise: $\varphi_{gg}[\kappa] = e^{-\sigma_\Delta^2 |\kappa|/2}$, and (c) continuous fading channel: $\varphi_{gg}[\kappa] = \varphi_{ff}[\kappa]$, as it was given in Eq. (2.7). Alternatively, \mathbf{l} can be obtained using adaptive algorithms, cf. e.g. [54].

C) Reduced State Sequence Detection (RSSD): As mentioned before, the number of phase state vectors of DBST-CPM is variable depending on the applied ST code (see Section 2.3.4). In particular, we found that for most of the power-efficient ST codes this number attains its maximal value of p^{N_T} . In these cases, the DBST-CPM trellis and thus the sequence detector, whether coherent or non-coherent, will require $p^{N_T} M^{L-1}$ states (using the modified CPM phase trellis given in [25, 26]). Hence, complexity of the receiver increases considerably with the number of transmit antennas N_T and the application of RSSD [26, 55] becomes desirable. In particular, we concentrate on reducing the phase states from p^m , $1 \leq m \leq N_T$, where the value of m depends on the ST code, to p , which is the same as for the single-antenna case. Accordingly, at each stage of the sequence detector only the largest out of p^m path metrics corresponding to the set of trellis states which differ

in the phase state only is selected, and thus, the number of possible branch metrics that need to be calculated in any given interval is reduced from $p^m M^L$ to pM^L .

2.3.4 Optimization of DBST-CPM

The diagonal structure of the DBST-CPM signalling matrix given in Eq. (2.30) guarantees full diversity. In addition, a significant coding gain can be realized if the the data mappings of successive frames are correctly chosen. Thus, the proper design of DBST-CPM requires an optimization of the structure of the vectors $\mathbf{a}[i]$. Let

$$\mathbf{C} \triangleq \{\mathbf{c}[1], \mathbf{c}[2], \dots, \mathbf{c}[M]\} \subset \mathcal{A}^{N_T}, \quad (2.39)$$

be the set of M vectors $\mathbf{c}[i] \triangleq [c_1[i] \ c_2[i] \ \dots \ c_{N_T}[i]]$ from which the $\mathbf{a}[i]$ are selected through the mapping of $\log_2(M)$ data bits. We refer to \mathbf{C} as the *ST code* of DBST-CPM. For example, one possibility is to choose $c_{n_t}[i] = c_1[i]$, $2 \leq n_t \leq N_T$, i.e., \mathbf{C} is a repetition code. The optimization of \mathbf{C} is similar to the optimization of the constellation parameters $[u_1 \dots u_{N_T}]$ in [32, Section VII]. However, due to the inherent memory of CPM, the optimization cannot be performed for individual modulation intervals as in [32], instead the entire ST signal $\mathbf{S}(t, \mathbf{a})$ has to be considered.

We consider the frame-error rate (FER) of DBST-CPM as the optimization criterion. For this purpose, in Section 2.3.4 we derive a tight upper bound for the FER, and an algorithm for its numerical evaluation is presented in Section 2.3.4.

Derivation of Frame Error Rate (FER) Bound

In this section, we will first derive the Chernoff bound on the pair-wise error probability (PEP) of our DBST-CPM scheme to demonstrate that it achieves full diversity. Then, we will derive a tighter bound on the FER, and finally truncate the bound to arrive at a useful

approximation of the upper bound that can be efficiently evaluated. For mathematical tractability we assume coherent MLSD and the QSFC in the derivation of the upper FER bound. As justification for these assumptions we note that the diagonal structure of the ST-CPM signal matrix was chosen for express purpose of facilitating non-coherent detection. Thus DBST-CPM yields non-coherent performance that approaches that of MLSD with CSI. In fact, simulation results in Section 2.3.5 will show that the non-coherent and reduced state performance of the ST-codes approaches coherent performance. Furthermore, the assumption of a QSFC is, in terms of code optimization, also a good approximation for the continuous fading channel since the memory of DBST-CPM is limited.

Pair-Wise Error Probability (PEP) The PEP $P(\mathbf{a}^\alpha \rightarrow \mathbf{a}^\beta)$ is the probability that the receiver erroneously decides in favour of the sequence \mathbf{a}^β when the transmitted sequence is \mathbf{a}^α . Under the assumption that the data sequence \mathbf{a}^α was transmitted the corresponding received signal and the QSFC coefficients are $\mathbf{r}(t, \mathbf{a}^\alpha)$ and $g_{n_t n_r}$, respectively. The MLSD metric, $m(\mathbf{r}(t, \mathbf{a}^\alpha), \mathbf{a}^\beta)$, for a trial sequence \mathbf{a}^β is then given by

$$m(\mathbf{r}(t, \mathbf{a}^\alpha), \mathbf{a}^\beta) = \sum_{n_t=1}^{N_T} \sum_{n_r=1}^{N_R} \int_0^{N_f T} |r_{n_r}(t + (n_t - 1)T, \mathbf{a}^\alpha) - g_{n_t n_r} x_{n_t}(t, \mathbf{a}^\beta)|^2 dt . \quad (2.40)$$

The PEP $P(\mathbf{a}^\alpha \rightarrow \mathbf{a}^\beta)$, conditioned on the channel \mathbf{G} follows as ($\Pr\{\cdot\}$ denotes probability)

$$P(\mathbf{a}^\alpha \rightarrow \mathbf{a}^\beta | \mathbf{G}) = \Pr\{m(\mathbf{r}(t, \mathbf{a}^\alpha), \mathbf{a}^\beta) < m(\mathbf{r}(t, \mathbf{a}^\alpha), \mathbf{a}^\alpha)\} = Q \left(\sqrt{\frac{d^2(\mathbf{a}^\alpha, \mathbf{a}^\beta, \mathbf{G})}{2\mathcal{N}_0}} \right) , \quad (2.41)$$

where $Q(x) \triangleq 1/\sqrt{2\pi} \int_x^\infty e^{-t^2/2} dt$, and

$$d^2(\mathbf{a}^\alpha, \mathbf{a}^\beta, \mathbf{G}) \triangleq \sum_{n_t=1}^{N_T} \sum_{n_r=1}^{N_R} |g_{n_t n_r}|^2 \Delta_{n_t} \quad (2.42)$$

is the sum of the scaled squared Euclidean distances

$$\Delta_{n_t} \triangleq \int_0^{N_f T} |x_{n_t}(t, \mathbf{a}_{n_t}^\alpha) - x_{n_t}(t, \mathbf{a}_{n_t}^\beta)|^2 dt, \quad (2.43)$$

between the transmitted and the erroneous CPM signal for antenna n_t . Considering the CPM signal description in Eq. (2.27), the squared Euclidean distances can be written as

$$\Delta_{n_t} = 2NE_s - \frac{2E_s}{T} \int_0^{N_f T} \cos \left(2\pi h \sum_{i=0}^{N_f-1} (a_{n_t}^\alpha[i] - a_{n_t}^\beta[i])q(t - iT) \right) dt, \quad (2.44)$$

which only depends on the difference sequence $\gamma_{n_t}[i] \triangleq a_{n_t}^\alpha[i] - a_{n_t}^\beta[i]$. The Chernoff bound for the average PEP has the familiar form

$$P(\mathbf{a}^\alpha \rightarrow \mathbf{a}^\beta) \leq \left(\prod_{n_t=1}^{N_T} \frac{1}{1 + \Delta_{n_t}/(4N_0)} \right)^{N_R}. \quad (2.45)$$

If the code words in \mathbf{C} are different in each position, then $\Delta_{n_t} > 0$ for $1 \leq n_t \leq N_T$ and DBST-CPM achieves full diversity.

Bound on FER In principle, we could directly use the Chernoff bound on the PEP as a design criterion and only consider the dominant error event maximizing Eq. (2.45). However, when the fading channel is static, there are no dominant error events, since for any given frame the received signal-to-noise ratio (SNR) may be low, which results in a high probability for all error events. Alternatively, we could combine the PEP bound Eq. (2.45) with the union bound, which sums over all possible error events. But, again when the channel is static or only slowly varying, the union bound is typically not tight and may diverge even at high SNR [36].

Hence, in order to produce a useful design criterion we adopt another approach that

was applied in [36] to estimate the performance of space-time trellis codes for the QSFC. In order to prevent the union bound from diverging at low SNR, we define a region \mathcal{R} that contains values of the channel matrix \mathbf{G} that result in low SNR. While there are many possibilities for defining a suitable \mathcal{R} , spherical and cubical regions provide simple and tight bounds. Of these two possibilities the spherical region provides a tighter and simpler bound, but a closed-form expression cannot be found for more than one receive antenna [36]. In this section, for simplicity we will present the FER bound assuming one receive antenna and the spherical bound, but we note that the bound can be extended to any number of receive antennas using the cubical bound. We define region \mathcal{R} as an N_T dimensional hypersphere of radius R centered around the origin

$$\mathcal{R} \triangleq \left\{ \mathbf{G} \left| \sum_{n_t=1}^{N_T} |g_{1n_t}|^2 \leq R^2 \right. \right\}, \quad (2.46)$$

and upper bound the FER by

$$P_e = \Pr\{e|\mathbf{G} \in \mathcal{R}\} \Pr\{\mathbf{G} \in \mathcal{R}\} + \Pr\{e|\mathbf{G} \notin \mathcal{R}\} \Pr\{\mathbf{G} \notin \mathcal{R}\} \quad (2.47)$$

$$\leq \Pr\{\mathbf{G} \in \mathcal{R}\} + \Pr\{\mathbf{G} \notin \mathcal{R}\} \sum_{\mathbf{a}^\alpha} \Pr(\mathbf{a}^\alpha) \sum_{\mathbf{a}^\beta \neq \mathbf{a}^\alpha} P(\mathbf{a}^\alpha \rightarrow \mathbf{a}^\beta | \mathbf{G}). \quad (2.48)$$

Making use of the derivation in [36, Appendix] and the PEP from Eq. (2.41), we can find a closed-form expression for the bound on the FER. The bound is dependent on the relationship between the squared Euclidean distances Δ_{n_t} . As an illustration we will explicitly show expressions for the bound for two different special cases.

A) Distinct Euclidean Distances: When all squared Euclidean distance terms are

unique, i.e., for $\Delta_{n_t} \neq \Delta_i$ for $n_t \neq i$, the bound can be written as

$$P_e \leq \left[1 - e^{-R^2} \left(\sum_{n_t=1}^{N_T} \frac{R^{2n_t}}{n_t!} \right) \right] + \frac{1}{2} \sum_{\mathbf{a}^\alpha} \Pr(\mathbf{a}^\alpha) \sum_{\mathbf{a}^\beta \neq \mathbf{a}^\alpha} \left[\sum_{n_t=1}^{N_T} \left(\prod_{i \neq n_t} \frac{1}{(\Delta_i - \Delta_{n_t})\gamma} \right) \frac{e^{-(1+\Delta_{n_t}\gamma)R^2}}{(1 + \Delta_{n_t}\gamma)} \right], \quad (2.49)$$

where $\gamma = 1/(4\mathcal{N}_0)$.

B) Identical Euclidean Distances: When all squared Euclidean distance terms are identical, i.e., $\Delta_{n_t} = \Delta$ for $1 \leq n_t \leq N_T$, the bound can be written as

$$P_e \leq \left[1 - e^{-R^2} \left(\sum_{n_t=1}^{N_T} \frac{R^{2n_t}}{n_t!} \right) \right] + \frac{1}{2} \sum_{\mathbf{a}^\alpha} \Pr(\mathbf{a}^\alpha) \sum_{\mathbf{a}^\beta \neq \mathbf{a}^\alpha} \left[e^{(1+\Delta\gamma)R^2} \sum_{n_t=0}^{N_T-1} \frac{R^{2n_t}}{(1 + \Delta\gamma)^{N_T-n_t}} \frac{1}{n_t!} \right]. \quad (2.50)$$

During numerical evaluation of P_e , the radius, R , of the hypersphere is optimized to produce the tightest upper bound using a Golden Section search [56, Section 10.1].

Truncated Bound on FER The number of distance terms that need to be considered for the FER bound, e.g. in Eqs. (2.49) and (2.50) for the two special cases, can be reduced by using the concept of simple error events, cf. e.g. [36, 37, 38]. An error event is considered a simple error event if the erroneous sequence diverges from the transmitted sequence and re-merges only once, i.e., there is only one erroneous segment in the received stream. Furthermore, because calculation of the entire distance spectrum is computationally expensive we truncate the sum such that terms whose product distance

$$p(\mathbf{\Delta}) \triangleq \prod_{n_t=1}^{N_T} \Delta_{n_t} \quad (2.51)$$

for $\mathbf{\Delta} \triangleq [\Delta_1 \dots \Delta_{N_T}]$ exceed a threshold p_{\max} are discarded. Hence, considering for example the case that all Δ_{n_t} are unique [Eq. (2.49)], the truncated bound can be numerically

evaluated as

$$P_e \leq \left[1 - e^{-R^2} \left(\sum_{n_t=1}^{N_T} \frac{R^{2n_t}}{n_t!} \right) \right] + \sum_{p(\mathbf{\Delta}) < p_{\max}} A(\mathbf{\Delta}) \left[\sum_{n_t=1}^{N_T} \left(\prod_{i \neq n_t} \frac{1}{(\Delta_i - \Delta_{n_t})^\gamma} \right) \frac{e^{-(1+\Delta_{n_t}\gamma)R^2}}{(1 + \Delta_{n_t}\gamma)} \right], \quad (2.52)$$

where $A(\mathbf{\Delta})$ accounts for the multiplicity and the probability of the pair-wise error events with distance vector $\mathbf{\Delta}$. The contribution of Δ_{n_t} to the bound in Eq. (2.49) decreases exponentially with increasing Δ_{n_t} , therefore, when p_{\max} is large the truncated bound is a good approximation of the upper bound. Similar expressions for the truncated bound can be found for any number of unique and repeated squared Euclidean distance terms, e.g. for the case of all repeated Euclidean distances considered in Eq. (2.50).

The weight $A(\mathbf{\Delta})$ can be evaluated by assuming that the frame length N_f is very large. Using this assumption edge effects caused by termination of trellis can be neglected and all error events can be assumed to start in the middle of a long block. Analysis of this kind is referred to as first error event analysis [57]. Following this assumption, an error event of length L_e symbols may be repeated N_f/L_e times. Therefore, the weight of an error event with distance vector $\mathbf{\Delta}$ is written as

$$A(\mathbf{\Delta}) = \sum_{L_e} \sum_b \frac{N_f}{L_e} N_e(b, L_e, p(\mathbf{\Delta})) \prod_{i=0}^{L_e} P(\gamma_1[i]) \quad (2.53)$$

where $N_e(b, L_e, p(\mathbf{\Delta}))$ denotes the multiplicity of error events with number of bit errors b , length L_e , and product distance $p(\mathbf{\Delta})$, and $P(\gamma_1[i])$ denotes the probability of difference sequence $\gamma_1[i]$ and is given by $P(\gamma_1[i]) = (M - |\gamma_1[i]/2|)/M$.

Note that the difference sequences for all antennas $n_t > 1$ are uniquely determined by the difference sequence of antenna $n_t = 1$. Therefore, the probability of the pair-wise error event with distance vector $\mathbf{\Delta}$ is dependent only on the data stream transmitted from antenna $n_t = 1$.

Algorithm for Numerical Evaluation of the Truncated FER Bound

To find the optimal DBST-CPM ST code for any given CPM format we require an efficient search algorithm. Our proposed algorithm finds the optimum code \mathbf{C} by evaluating the truncated upper bound [e.g. Eq. (2.52)] for all possibilities for \mathbf{C} and selecting the code that produces the lowest bound. In particular, exploiting the symmetry of the problem, $(M!/N_T!)^{N_T-1}$ combinations of code vectors need to be examined.

To find all pairs $(\mathbf{\Delta}, A(\mathbf{\Delta}))$ required for the truncated bound, i.e., the distance spectrum, we extend the algorithm presented in [58] for CPM with a single antenna. Initially, the possible difference sequence sets $\{\gamma_{n_i}\}$ for the ST code and their probabilities must be determined. For example, for a two antenna system, $M = 4$, and ST code

$$\mathbf{C} = \left\{ \left[\begin{array}{c} -3 \\ -1 \end{array} \right], \left[\begin{array}{c} -1 \\ +3 \end{array} \right], \left[\begin{array}{c} +1 \\ -3 \end{array} \right], \left[\begin{array}{c} +3 \\ +1 \end{array} \right] \right\}$$

the possible difference sequences are given by

$$\left\{ \left[\begin{array}{c} \gamma_1 \\ \gamma_2 \end{array} \right] \right\} = \left\{ \left[\begin{array}{c} 0 \\ 0 \end{array} \right], \left[\begin{array}{c} -2 \\ -4 \end{array} \right], \left[\begin{array}{c} -4 \\ +2 \end{array} \right], \left[\begin{array}{c} -6 \\ -2 \end{array} \right], \left[\begin{array}{c} -2 \\ +6 \end{array} \right], \left[\begin{array}{c} +2 \\ +4 \end{array} \right], \left[\begin{array}{c} +4 \\ -2 \end{array} \right], \left[\begin{array}{c} +6 \\ +2 \end{array} \right], \left[\begin{array}{c} +2 \\ -6 \end{array} \right] \right\}$$

Additionally, the bound p_{\max} on the product distance and a bound on the length of error sequences must be set.

Table 2.1 shows the pseudo-code for the algorithm that calculates the distance spectrum. \mathbf{e}_i denotes an error sequence, i.e., a vector of difference sequences, and the algorithm begins by evaluating the distance of all possible error sequences of length $L_e = 1$. The algorithm maintains a list \mathcal{L} of error sequences that satisfy all of the criteria of the algorithm.

Once the length one error sequences have been evaluated each error sequence is treated individually and extended by one difference symbol, and the corresponding Euclidean distance, the error sequence weight, and the length of the error sequence are recorded, and the algorithm proceeds with $L_e = 2$ and so forth. As the algorithm proceeds error events that exceed the bound p_{\max} are discarded, and error events with the same product Euclidean distance $\prod_{n_t=1}^{N_T} \Delta_{n_t}$, the same number of bit errors b , the same length L_e , and the same phase state $\sum_{i=1}^n \gamma_1[i]$ are merged by adding their weighting factors. If the error event path re-merges with the transmitted stream, i.e., $\sum_{i=1}^n \gamma_{n_t}[i] = 0$ for all $n_t = 1, \dots, N_T$, then the path is saved and is no longer updated. The algorithm is terminated when there are no remaining error events to update with $p(\Delta) < p_{\max}$, or the error event path length reaches a pre-defined upper bound.

2.3.5 Performance Results

In this section, we present extensive performance results for the proposed DBST-CPM scheme. The ST codes considered for simulation have been optimized by setting $p_{\max} = 30^{N_T}$ in the search algorithm in Table 2.1. The same threshold is applied for all numerical FER results shown in this section. One receive antenna and a frame length of $N_f = 130$ are assumed in all cases. The number of filters in the receive filter bank is chosen to be $D = 3$. Phase-increment mapping [26] is applied for all CPM schemes. Unless stated otherwise, DBST-CPM with $M = 4$, $h = 1/2$, and 1REC pulse is assumed. Numerical and simulation results are presented as function of the SNR E_b/N_0 , where $E_b = \frac{E_s}{\log_2(M)/N_T}$ denotes the average received energy per bit.

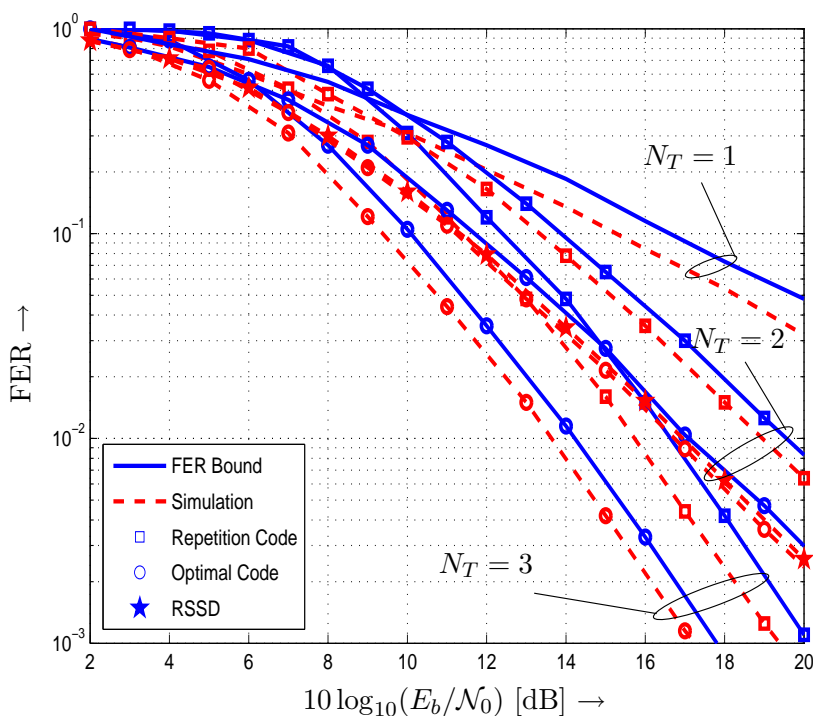


Figure 2.7: FER vs. $10 \log_{10}(E_b/N_0)$ for 1REC pulse, $h = 1/2$, and $M = 4$. DBST-CPM ($N_T = 2$ and $N_T = 3$) with repetition code and optimal code and CPM with $N_T = 1$. Simulation results and the analytical upper bound are compared for the QSFC.

Coherent Detection

In order to separate the effects of code optimization, state reduction, and non-coherent detection, we first present results for coherent detection and the QSFC. The subsequent section will show that the gains obtained under these conditions also apply to non-coherent detection and non-quasi-static fading environments.

A) MLSD: Figure 2.7 depicts the FERs of coherent MLSD for the optimal ST code \mathcal{C} found with the algorithm from Section 2.3.4 and for the repetition code for $N_T = 2$ and $N_T = 3$, respectively. As a reference, the FER for the same CPM scheme and $N_T = 1$ is also shown. It can be seen that the results obtained from simulation (dashed lines) and from numerical evaluation of the truncated bound (solid lines) are in good agreement. We note

that the tightness of the bound is a function of the truncation parameter p_{\max} , which should be set with some care. Large p_{\max} are computationally expensive, and small p_{\max} may not provide an upper bound. Importantly, however, when we set $p_{\max} = 30^{N_T}$ we found that the bound accurately predicts the performance ordering of different codes for numerous system parameters and gives a quantitatively precise approximation of the performance gained by using the optimal code \mathcal{C} in comparison to e.g. the simple repetition code. For the chosen example, this gain amounts to 2 dB in power efficiency for both $N_T = 2$ and $N_T = 3$.

Comparing the performances for DBST-CPM with $N_T = 2$, $N_T = 3$ and single-antenna CPM, we observe that DBST-CPM with multiple antennas results in considerable improvements in power efficiency. In particular, the slopes of the FER curves confirm the diversity advantage of DBST-CPM. Since the same CPM scheme is used for both $N_T = 1$, $N_T = 2$, and $N_T = 3$, the data rate for single-antenna CPM is double of that for DBST-CPM with $N_T = 2$ for example. However, a truly fair comparison is difficult as increasing the size M of the signal constellation also affects the bandwidth of the CPM signal.

B) RSSD: When the repetition code is employed the CPM signals transmitted over N_T antennas are all identical, which means that the number of states for MLSD is pM^{L-1} (independent of N_T) and less than that for the optimal code with in general $p^{N_T}M^{L-1}$ states. Figure 2.8 provides a comparison of DBST-CPM with MLSD and RSSD. For the optimal code, MLSD is performed in a four-state trellis while a trellis with only two states is used for RSSD, (the number of states required for MLSD of the repetition code, cf. Figure 2.6). We observe that state reduction causes only a small performance degradation. In particular, the gains from code optimization are also well preserved for RSSD.

C) Overview of Results for QSFC: Tables 2.2-2.4 provide an overview of the numerically evaluated performance gains obtained with optimized DBST-CPM for $N_T = 2$

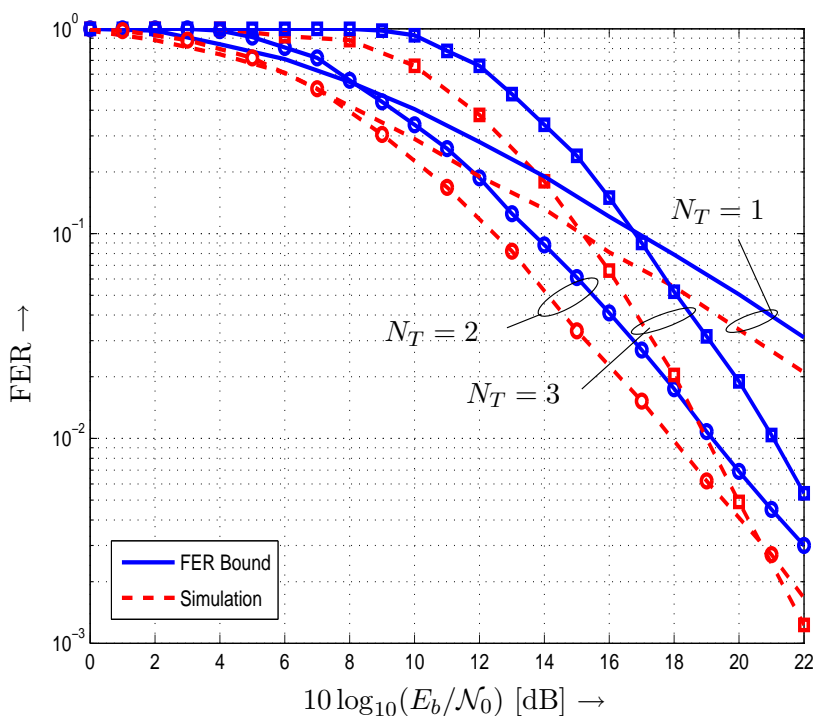


Figure 2.8: FER vs. $10 \log_{10}(E_b/\mathcal{N}_0)$ for 1REC pulse, $h = 1/2$, and $M = 4$. DBST-CPM ($N_T = 2$) with repetition code and optimal code. MLSD and RSSD with CSI for the QSFCC.

and $N_T = 3$ antennas and a variety of CPM formats. In particular, the popular 1REC, 2RC, and 3RC CPM pulse shapes (for 2RC and 3RC CPM, the frequency pulse $g(t)$ is a raised cosine pulse of length $L = 2$ and $L = 3$, respectively, cf. [42]), constellation sizes $M = 4$ and $M = 8$, and modulation indices of $h = 1/2, 1/3$, and $1/4$ are considered. The tables present the optimum codes \mathcal{C} for $N_T = 2$ and $N_T = 3$ and the associated performance gains compared to repetition codes, with respect to the required $10 \log_{10}(E_b/\mathcal{N}_0)$ to obtain an FER of 10^{-2} .

These tables show that depending on the number of transmit antennas and the modulation format gains between 0.7 dB and 5 dB are possible by using an optimally selected code. A direct comparison of the performance of single antenna transmission and the

performance of the ST coding scheme is difficult due to the non-linear relationship of the normalized CPM bandwidth ($B_{99\%}T$) and parameters M and h . However, we will make one comparison here to illustrate the benefits of the proposed ST coding scheme. The quaternary 2RC DBST-CPM scheme with $N_T = 2$ and $h = 1/4$ (see Table 2.2) has a normalized bandwidth of $B_{99\%}T = 1.24$. A binary 2RC single-antenna scheme with $h = 1/2$ has the same data rate and the normalized bandwidth is $B_{99\%}T = 1.05$, i.e., quite comparable to that of DBST-CPM. DBST-CPM achieves a FER of 10^{-2} at 19.2 dB, whereas the single-antenna scheme requires 28.0 dB. This is a significant performance improvement of more than 8 dB.

Non-coherent Detection

In this section, we will present performance results for the different fading channel models introduced in Section 2.1 and non-coherent detection employing the branch metrics described in Section 2.3.3. In all cases, the first two symbols of each frame are assumed to be known at the receiver to allow for an initialization of the reference symbol defined in Eq. (2.36). The filter length used for the reference symbol is gradually increased from 2 to N_d at the beginning of each frame until the N_d^{th} symbol is received.

Figure 2.9 shows the performance results for the QSFC and non-coherent detection with different values of N_d . DBST-CPM with the optimal ST code and with the repetition code are compared for $N_T = 2$. The respective curves for coherent detection are included as a reference. We would like to emphasize that the number of states for non-coherent detection is the same as that for coherent detection (see Section 2.3.3). As can be seen, the FER curves for non-coherent detection closely approach those for coherent detection with increasing N_d . Hence, code optimization based on the MLSD bound for coherent detection also yields results relevant for the case of non-coherent detection. The repetition code yields a somewhat faster convergence with increasing N_d , since in this case DBST-CPM

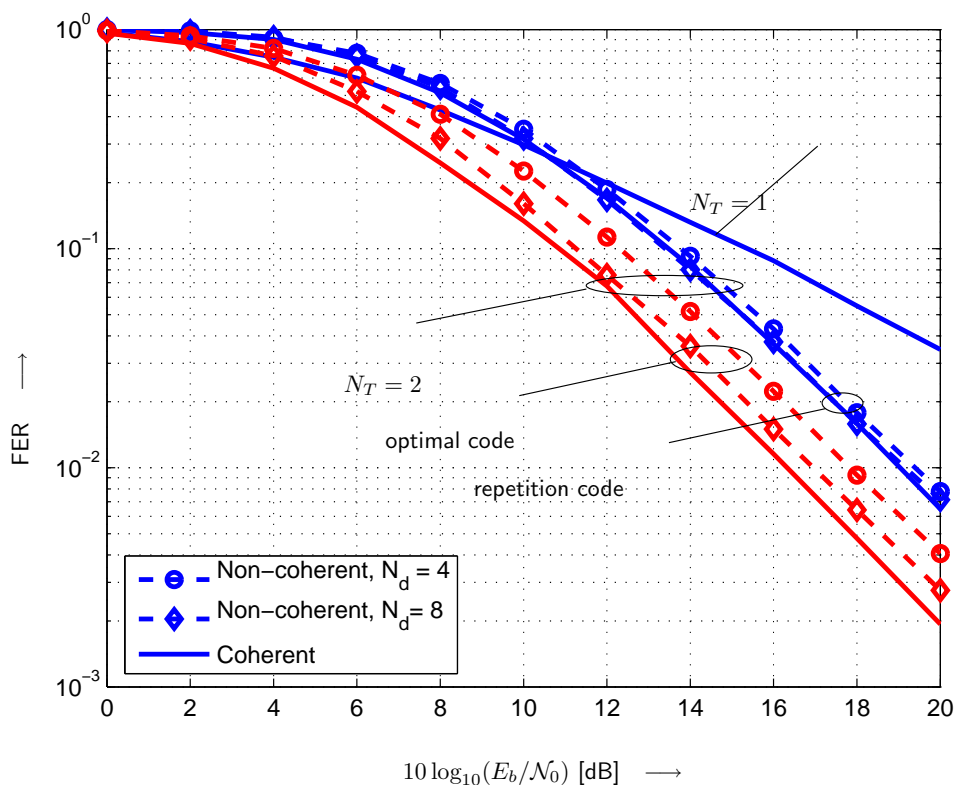


Figure 2.9: FER vs. $10 \log_{10}(E_b/N_0)$ for 1REC impulse, $h = 1/2$, and $M = 4$. DBST-CPM ($N_T = 2$) with repetition code and optimal code. Coherent detection with CSI and non-coherent detection without CSI for the QSFC. 2-state trellis for repetition code, 4-state trellis for optimal code.

has a trellis with only $p = 2$ phase states, whereas $p^{N_T} = 4$ phase states are present for the optimal code design (cf. Figure 2.6).

For the same DBST-CPM scheme, Figure 2.10 shows the performances for the optimal and the repetition ST codes for the QSFC channel with phase noise of variance $\sigma_{\Delta}^2 = 0.01$. $N_d = 2$ and $N_d = 5$ are chosen for non-coherent detection. We observe that although both codes suffer from a performance degradation compared to ideal coherent detection, the optimal code still outperforms the repetition code by approximately the same margin as for coherent detection.

Finally, the performance of DBST-CPM with the same codes as above is shown for a

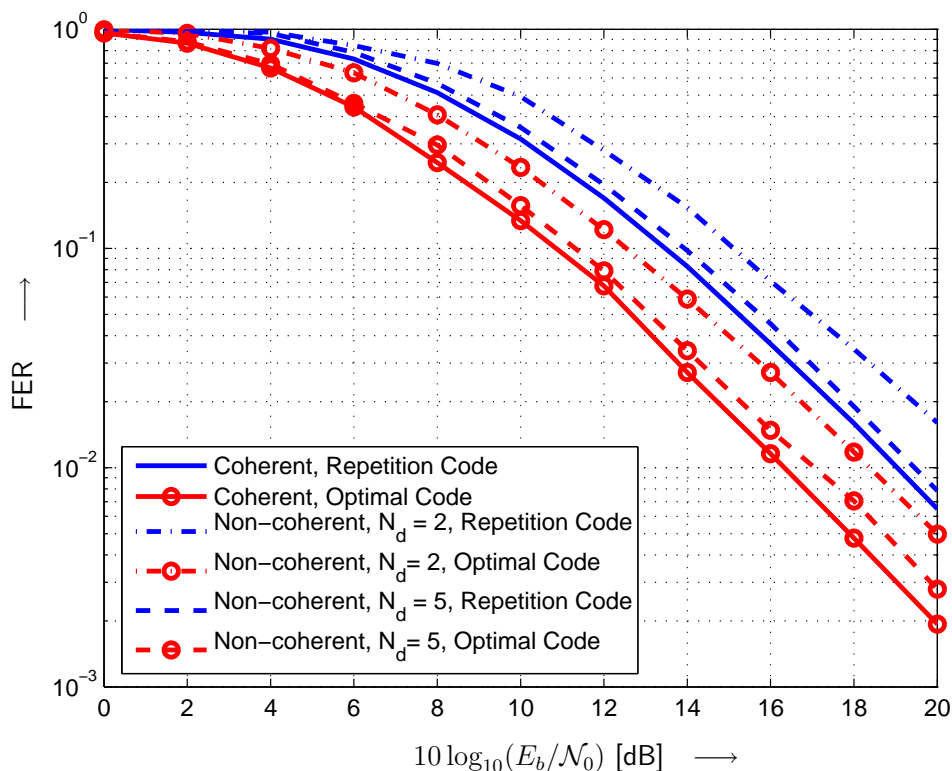


Figure 2.10: FER vs. $10 \log_{10}(E_b/N_0)$ for 1REC pulse, $h = 1/2$, and $M = 4$. DBST-CPM ($N_T = 2$) with repetition code and optimal code. Coherent detection with CSI and non-coherent detection without CSI for the QSFC with phase noise with variance $\sigma_{\Delta}^2 = 0.01$. 2-state trellis for repetition code, 4-state trellis for optimal code.

continuous fading channel in Figure 2.11. The fading bandwidth is adjusted to $B_f T = 0.03$ and $N_d = 2$ and $N_d = 14$ are chosen for non-coherent detection. We observe that, different from the QSFC, the performance gain offered by the optimal DBST-CPM code over the repetition code continues to increase for SNRs up to 30 dB. For this fading scenario, gain becomes fixed, i.e., the curves run parallel, only at very high SNR. It can further be seen that the improvement due to the optimal ST code predicted from considering coherent detection is closely realized also for non-coherent detection with appropriately chosen N_d , which confirms the relevance of the conducted code optimization. Of course, a gap in absolute power efficiency between coherent and non-coherent remains for this relatively

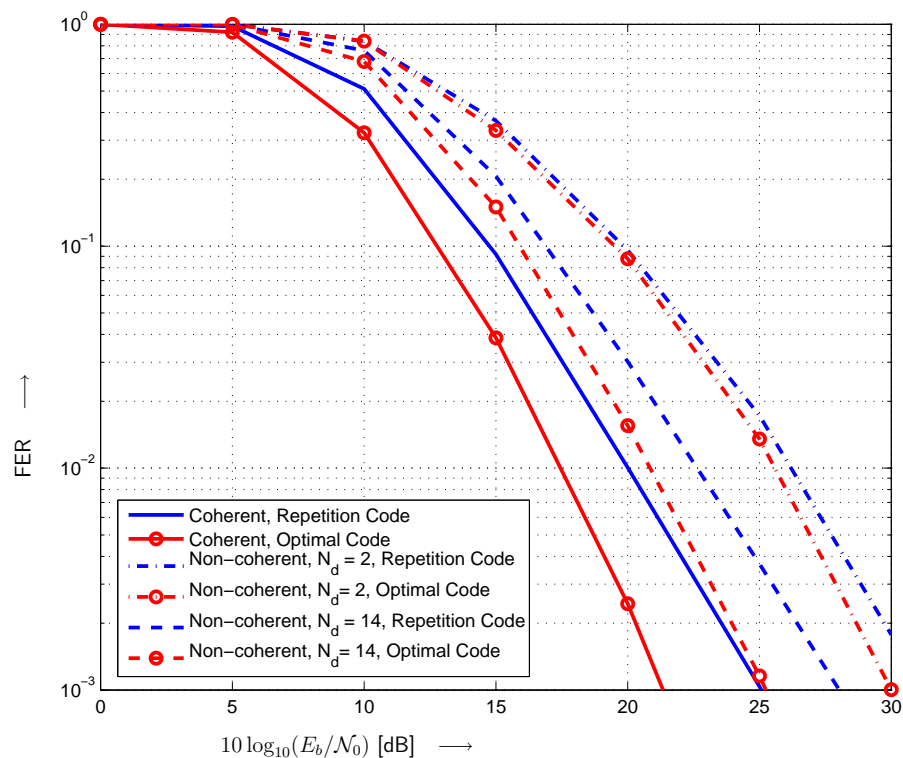


Figure 2.11: FER vs. $10 \log_{10}(E_b/N_0)$ for 1REC pulse, $h = 1/2$, and $M = 4$. DBST-CPM ($N_T = 2$) with repetition code and optimal code. Coherent detection with CSI and non-coherent detection without CSI for the continuous fading channel with normalized bandwidth $B_f T = 0.03$. 2-state trellis for repetition code, 4-state trellis for optimal code.

fast fading environment. We note however that coherent detection with perfect CSI is only an idealized model, which cannot be realized in practice.

Comparison with ST-CPM Schemes from the Literature

Although the main advantage of the proposed DBST-CPM is its flexibility with respect to the CPM parameters and the number of antennas, it is insightful to compare the power efficiency of DBST-CPM with those of less flexible but also non-coherent detectable schemes from the literature for the same/similar bandwidth efficiency. In particular, we consider the ST-CPM schemes devised by Pande, Huh, and Krogmeier [3] (PHK scheme) and Pan-

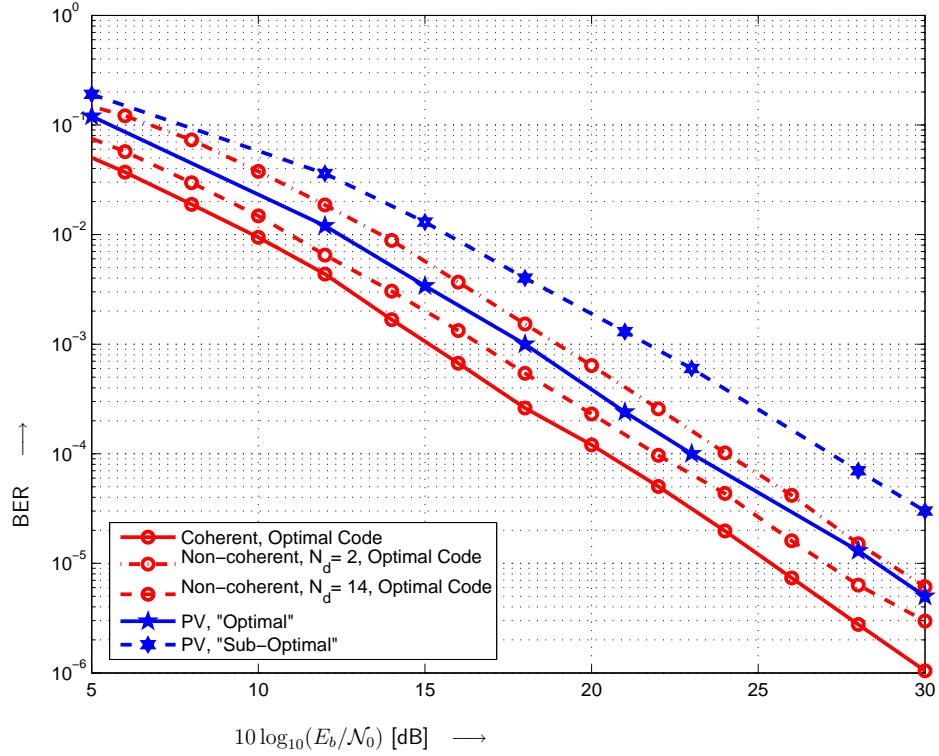


Figure 2.12: BER vs. $10 \log_{10}(E_b/N_0)$ for DBST-CPM and the PV scheme [2], both with $N_T = 2$. DBST-CPM: 1REC pulse, $h = 1/2$, and $M = 4$. PV ST-CPM: 1REC pulse, $h = 1/2$, and $M = 4$ (“sub-optimal”) and $M = 8$ (“optimal”). Data rate is 1 bit per symbol duration T in all cases. Non-coherent detection without CSI for the continuous fading channel with normalized bandwidth $B_f T = 0.001$. As reference: DBST-CPM and coherent detection with CSI.

caldi and Vitetta [2] (PV scheme), which are designed for $N_T = 2$ and full response CPM and its special case CPFSK, respectively.

First, we consider the PV scheme for which bit-error rate (BER) results were presented in [2, Figure 1] for a continuous fading channel with $B_f T = 0.001$ and the parameters $N_T = 2$, $N_R = 1$, 1REC pulse, $h = 1/2$, and both $M = 4$ and $M = 8$. The PV schemes with $M = 4$ and $M = 8$ were referred to as “optimal” and “suboptimal” in [2], and the data rate is 1 bit per symbol duration T in both cases. In Figure 2.12, we show the BER for the PV scheme and for DBST-CPM with the same parameters but $M = 4$ only, i.e., DBST-CPM has the same bandwidth efficiency as the PV scheme with $M = 4$, and

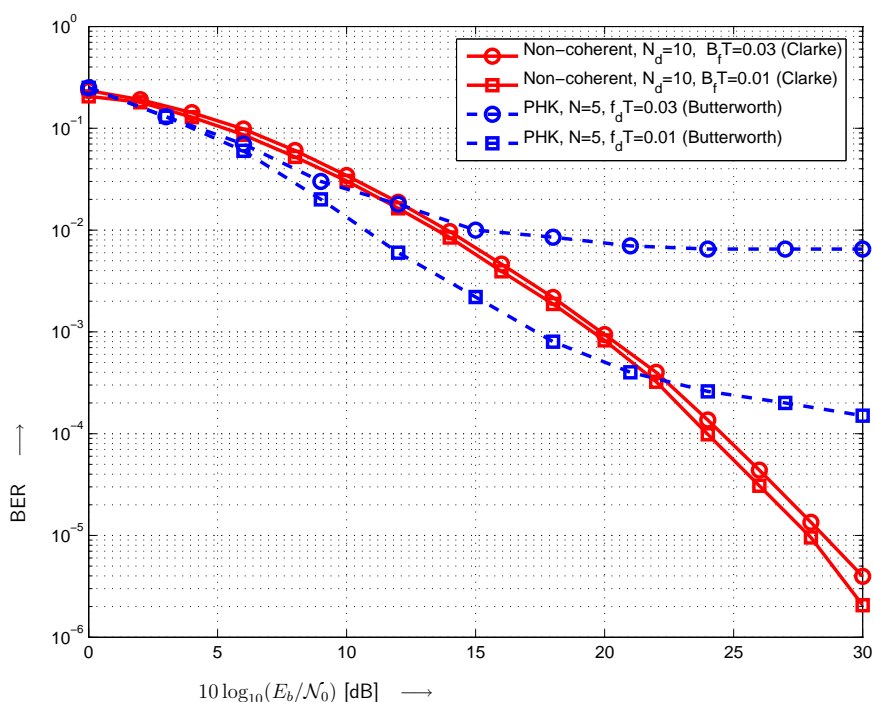


Figure 2.13: BER vs. $10 \log_{10}(E_b/N_0)$ for DBST-CPM and the PHK scheme [3], both with $N_T = 2$. DBST-CPM: 1REC pulse, $h = 1/4$, and $M = 4$. PHK ST-CPM: 1REC pulse, $h = 1/2$, and $M = 2$. Data rate is 1 bit per symbol duration T in all cases. Non-coherent detection without CSI for the continuous fading channel with normalized bandwidth $B_f T = f_d T = 0.01$ and $B_f T = f_d T = 0.03$ according to Clarke’s model for DBST-CPM and a third order Butterworth spectrum for PHK scheme. $N_d = 10$ for DBST-CPM corresponds to $N = 5$ for the PHK scheme.

a higher bandwidth efficiency than the PV scheme with $M = 8$, due to the bandwidth expansion of CPM with $M = 8$. It can be seen that DBST-CPM outperforms the PV schemes with $M = 4$ and $M = 8$ in terms of BER, i.e., it is advantageous both in power and in bandwidth efficiency. It is difficult to compare the detection complexities for DBST-CPM and the PV scheme, since the latter employs a “codeword-by-codeword” detection, where a codeword corresponds to an M -ary ST-CPM symbol. As a coarse indicator of complexity, we mention that the number of (branch) metric calculations needed per data symbol is 16 for DBST-CPM, and 4 and 8 for the PV scheme with $M = 4$ and $M = 8$, respectively.

Next, we consider the PHK scheme and MSK, i.e., 1REC pulse, $M = 2$ and $h = 1/2$, for which results were presented in [3, Figure 5] for $N_T = 2$, $N_R = 1$ and continuous fading. The data rate of this PHK scheme is 1 bit per symbol duration T . In order to achieve the same data rate we use quaternary DBST-CPM. We further choose a 1REC pulse and $h = 1/4$, whose normalized CPM bandwidth is $B_{99\%}T = 1.44$, which is reasonably close to the $B_{99\%}T = 1.18$ of MSK used in [3]. The spectrum of the fading process in [3] has a third order Butterworth characteristic with 3 dB bandwidth f_dT , which is different from the fading spectrum according to Clarke considered in this paper. Still, we compare BER curves from [3, Figure 5] with those for DBST-CPM and the Clarke fading model with $B_fT = f_dT = 0.01$ and 0.03 , respectively, in Figure 2.13. The curves from [3, Figure 5] with detection parameter $N = 5$ are plotted in Figure 2.13, which corresponds to non-coherent detection with $N_d = 10$ for DBST-CPM. It is interesting to observe that the PHK scheme suffers from a significantly higher error floor as compared to DBST-CPM. This difference in error floor can be attributed to (a) the orthogonal ST-code structure of the PHK scheme, which is more sensitive to channel variations than the diagonal code structure adopted for DBST-CPM, and (b) the superior non-coherent detector developed for DBST-CPM. We note that the error floor is a function of the fading bandwidths B_fT and f_dT , which are adjusted to the same values in Figure 2.13. The performance difference for lower SNR values could be due to the different fading processes considered.

2.4 Conclusions

In this chapter, we have presented and analyzed two ST-CPM coding schemes. In Section 2.2, we proposed a simple OSTBC scheme for CPM. The advocated burst-based approach allows the straightforward combination of any CPM format with ODs. After an appropriate combining at the receiver, the same detection techniques as in case of single-antenna

transmission can be applied. The proposed scheme entails a lower complexity than all previously proposed ST coding schemes for CPM and yields a better performance for the important case of $N_T = 2$ transmit antennas. For $N_T > 2$ transmit antennas OSTBC for CPM suffers from the same rate loss as all ST coding schemes based on ODs.

In Section 2.3, we proposed the DBST-CPM scheme for power-efficient transmission over fading channels. The design was inspired by DSTM for linear modulation employing diagonal signal matrices and, similar to DSTM, enables non-coherent detection without CSI. We devised a low-complexity receiver design including branch metrics for reduced-state non-coherent sequence detection of DBST-CPM and different fading channels. To facilitate code selection we derived an upper bound for the FER of DBST-CPM and proposed an efficient algorithm for finding the optimal DBST-CPM code. Numerical and simulation results showed that the upper bound accurately predicts the performance of DBST-CPM for coherent detection in a QSFC. Similarly, the numerical and simulation results showed that the proposed code optimization yields significant improvements in power efficiency for all channel models, and for both coherent and non-coherent detection.

Table 2.1: Pseudo-code for distance spectrum calculation for DBST-CPM.

Input: $[N_T, N_f, p_{\max}, \text{CPM parameters}]$ Generate list of difference sequences $\gamma_1 \dots \gamma_J$, J is the number of difference sequences List of error events (length n) $\mathcal{L} = \emptyset$ List of error events (length $n + 1$) $\mathcal{L}' = \emptyset$ for ($n = 1, \dots, N_f$) $I_n = 1$ (Number of error sequences of length n) $\mathcal{L} = \mathcal{L}'$ $\mathcal{L}' = \emptyset$ for ($i = 1, \dots, I_n$) Select next error sequence e_i from \mathcal{L} for ($j = 1, \dots, J$) Extend e_i by γ_j Calculate $\Delta, A(\Delta)$ if (e_i is simple and $p(\Delta) \leq p_{\max}$) if (e_i can be merged with another entry in \mathcal{L}') Update $A(\Delta)$ for the matching entry in \mathcal{L}' else Add e_i to \mathcal{L}' end if end if end for end for end for
--

Table 2.2: Optimized DBST-CPM for $N_T = 2$ and $M = 4$. Gain with respect to repetition code considering an FER of 10^{-2} .

$M = 4$	1REC		2RC		3RC	
	Gain	Optimal Code	Gain	Optimal Code	Gain	Optimal Code
$h = \frac{1}{2}$	2.3	$-3, -1$ $-1, +3$ $+1, -3$ $+3, +1$	2.0	$-3, -1$ $-1, +3$ $+1, -3$ $+3, +1$	1.2	$-3, -1$ $-1, +3$ $+1, -3$ $+3, +1$
$h = \frac{1}{3}$	1.6	$-3, -3$ $-1, -1$ $+1, +3$ $+3, +1$	1.5	$-3, -1$ $-1, +3$ $+1, -3$ $+3, +1$	1.9	$-3, -1$ $-1, +3$ $+1, -3$ $+3, +1$
$h = \frac{1}{4}$	1.6	$-3, -1$ $-1, +3$ $+1, -3$ $+3, +1$	1.7	$-3, -1$ $-1, +3$ $+1, -3$ $+3, +1$	2.0	$-3, -1$ $-1, +3$ $+1, -3$ $+3, +1$

Table 2.3: Optimized DBST-CPM for $N_T = 2$ and $M = 8$. Gain with respect to repetition code considering an FER of 10^{-2} .

$M = 8$	1REC		2RC		3RC	
	Gain	Optimal Code	Gain	Optimal Code	Gain	Optimal Code
$h = \frac{1}{2}$	0.7	$-7, -7$ $-5, -5$ $-3, -1$ $-1, -3$ $+1, +5$ $+3, +1$ $+5, +3$ $+7, +7$	1.1	$-7, -7$ $-5, -1$ $-3, -5$ $-1, +7$ $+1, +1$ $+3, +5$ $+5, -3$ $+7, +3$	4.0	$-7, -5$ $-5, +3$ $-3, -1$ $-1, -7$ $+1, +7$ $+3, +1$ $+5, -3$ $+7, +5$
$h = \frac{1}{3}$	2.1	$-7, -7$ $-5, -5$ $-3, -1$ $-1, -3$ $+1, +1$ $+3, +3$ $+5, +7$ $+7, +5$	2.2	$-7, -7$ $-5, +5$ $-3, -1$ $-1, +3$ $+1, -3$ $+3, +1$ $+5, -5$ $+7, +7$	1.4	$-7, -7$ $-5, -1$ $-3, -5$ $-1, +1$ $+1, +7$ $+3, +3$ $+5, -3$ $+7, +5$
$h = \frac{1}{4}$	2.2	$-7, -5$ $-5, -1$ $-3, +5$ $-1, -7$ $+1, +3$ $+3, +7$ $+5, -3$ $+7, +1$	2.2	$-7, -7$ $-5, -5$ $-3, +7$ $-1, -1$ $+1, +5$ $+3, -3$ $+5, +3$ $+7, +1$	3.8	$-7, -7$ $-5, -3$ $-3, +3$ $-1, -1$ $+1, +5$ $+3, -5$ $+5, +1$ $+7, +7$

Table 2.4: Optimized DBST-CPM for $N_T = 3$ and $M = 4$. Gain with respect to repetition code considering an FER of 10^{-2} .

$M = 4$	1REC		2RC	
	Gain	Optimal Code	Gain	Optimal Code
$h = \frac{1}{2}$	5.0	+1, -3, +1 +3, -1, -3 -3, +1, +3 -1, +3, -1	2.4	-1, -3, +1 +3, -1, -3 +1, +1, +3 -3, +3, -1
$h = \frac{1}{3}$	3.3	-3, -3, +3 -1, +3, -1 +1, -1, +1 +3, +1, -3	4.2	-3, -3, -3 -1, -1, -1 +1, +1, +1 +3, +3, +3
$h = \frac{1}{4}$	3.1	-1, -3, +1 +3, -1, -3 +1, +1, +3 -3, +3, -1	3.0	-1, -3, +1 +3, -1, -3 +1, +1, +3 -3, +3, -1

Chapter 3

Distributed ST-CPM

When a network consists of a large number of wireless devices with the ability to relay transmissions, cooperation among these devices has been shown to improve the error performance and capacity of the wireless system [22]-[60]. In fact, it is possible for cooperative networks to achieve gains in the fading channel equal to those for devices with co-located antennas when nodes are positioned favorably, and the correct relay protocols are used [61]. In distributed relay applications (for example sensor networks) wireless devices are often battery-powered with stringent cost and energy constraints. In this environment, distributed ST codes employing linear modulation can produce a prohibitively large power drain at the linear power amplifier due to their high peak-to-average power ratios (PAPRs) [62]. Therefore, in this chapter we extend the concept of distributed space-time (ST) codes to transmission with continuous phase modulation (CPM) [42]. As always, CPM is a natural fit under energy constrained conditions due to its constant-envelope property that enables the use of energy-efficient and inexpensive nonlinear power amplifiers.

Node cooperation can take one of two forms: coordinated cooperation, or uncoordinated cooperation [21, 60, 63]. If coordinated cooperation is employed, cooperating nodes know which nodes are participating as source, destination and relay nodes, and standard ST codes optimized for co-located antennas can be used for relaying among the known devices. On the other hand, if uncoordinated transmission is employed the cooperating nodes (source, destination, and relays) are unaware of which nodes are active and participate in the transmission, and ST codes need to be designed correspondingly.

In this chapter the distributed ST-CPM codes we design are intended for use in a network employing uncoordinated node cooperation. The proposed codes are the product of two components: a ST code matrix (each relay node encodes the same information with the same ST code), and a unique signature vector. We adopt the diagonal block-based ST-CPM codes proposed in Chapter 2 for the underlying ST code, and we provide appropriate design rules for signature vector construction and efficient numerical methods for generation of signature vector sets. Employing the decode-and-forward (DF) protocol, assuming statistically identical relay-destination fading channels, and time synchronous transmission, the proposed distributed ST-CPM codes are found to provide a diversity order $d = \min\{N_S, N_c\}$ when N_S relay nodes are active and the ST-CPM codes are designed for N_c co-located antennas. Furthermore, the proposed distributed codes are also shown to incur only small losses in coding gain with respect to co-located antenna systems.

To the best of our knowledge, the proposed scheme is the first to present a distributed ST code for general CPM transmission, and thus to demonstrate that and how distributed ST processing for constant envelope signaling can be accomplished. While the proposed distributed ST-CPM scheme has a constant PAPR of one, the PAPR problem of linear modulations is only compounded when ST coding is applied. Thus, in the later portion of the chapter we analyze the energy savings made possible by switching to a CPM based distributed ST code using both the Class AB power amplifier used for linear modulation, and the more energy efficient Class C amplifier. This analysis shows definitively that the distributed ST-CPM scheme offers energy savings.

The chapter begins with an introduction to the relay network setup in Section 3.1. Then, in Section 3.2 the proposed distributed ST-CPM scheme is presented, and detection at the destination node is discussed. In Section 3.3, the energy consumption of the proposed distributed ST-CPM is analyzed and compared with the energy consumption of a

distributed ST scheme built upon linear modulation. Section 3.4 concludes the chapter.

3.1 Relay Network Setup

We consider a network consisting of a (possibly large) number $(N + 2)$ of nodes. During communication between two nodes, i.e. the source and destination node, the other N nodes act as potential relays for the signal transmitted from the source. We label each of the relay nodes $n \in \mathcal{N}$, $\mathcal{N} \triangleq \{1, 2, \dots, N\}$. We assume that the network employs DF relaying and an error detecting code, for example a cyclic redundancy check (CRC) code [21, 22, 60]. Under these assumptions the active subset of relay nodes, i.e. those that were able to correctly decode the received message, is *a priori* unknown. More explicitly, we apply an uncoordinated approach in the sense that the source-destination pair has no knowledge of which nodes act as relays, and the relay nodes have no knowledge of the source-destination pair or of which other nodes are participating relay nodes. We assume, however, that the clocks of the nodes are sufficiently synchronized and that the maximal distance between relay nodes satisfies $d_{\max} \ll c \cdot T$, where c is the speed of light and T is the symbol duration, so that all relay signals are received synchronously at the destination node. The source-relay and relay-destination channels are modeled as quasi-static frequency-nonselctive fading channels, which is an appropriate model for many distributed relay networks such as wireless sensor networks (WSNs) for monitoring, detection, and automation (cf. e.g. [22]-[60] where the same assumptions have been made).

Let us now consider the relay step. Due to coding with an $N_c \times N_c$ ST-CPM code as explained below, signals are organized in vectors of length N_c . Denoting the transmit signal of relay n by the vector function $\mathbf{s}_n(t) \triangleq [s_{n,1}(t), s_{n,2}(t), \dots, s_{n,N_c}(t)]^T$ and the channel gain

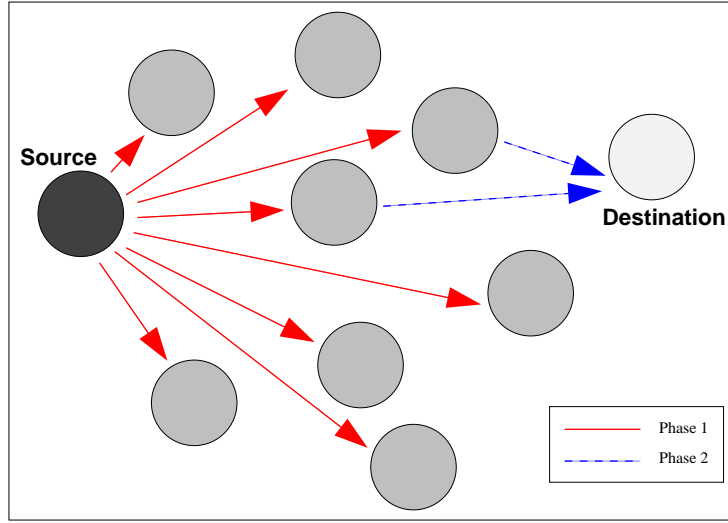


Figure 3.1: Two phase transmission in the relay network.

to the destination node by h_n , the received signal at the destination node is given by

$$\mathbf{r}(t) = \sum_{n \in \mathcal{S}} g_n \mathbf{s}_n(t) + \mathbf{n}(t), \quad (3.1)$$

where $\mathcal{S} = \{n_1, n_2, \dots, n_{N_S}\} \subseteq \mathcal{N}$ is the *a priori* unknown subset of active relay nodes of size $N_S \triangleq \text{card}\{\mathcal{S}\}$. Note that \mathcal{S} can change with the active source-destination pair, and between frames of data transmitted between the same source-destination pair. The channel gains g_n are modelled as for the QSFC (i.e. independently and identically distributed (i.i.d.) zero-mean complex Gaussian random variables with unit variance), and the noise term $\mathbf{n}(t) \triangleq [n_1(t), n_2(t), \dots, n_{N_c}(t)]^T$ is modelled as an independent additive white Gaussian noise (AWGN) vector process with power spectral density \mathcal{N}_0 .

3.2 Distributed ST-CPM for Relay Transmission

The distributed ST-CPM scheme that we propose consists of two components: an ST-CPM code that is common to all network nodes and signature vectors that are assigned

uniquely to each network node. This structure is inspired by [21], where distributed ST codes for linear modulation were devised. More specifically, if the signature vectors are $N_c \times 1$ unit-norm vectors $\boldsymbol{\kappa}_n = [\kappa_n[1], \dots, \kappa_n[N_c]]^T \in \mathcal{K}$, $n \in \mathcal{N}$, where \mathcal{K} denotes the set of all signature vectors, the relay signals are generated as

$$\mathbf{s}_n(t) = \sqrt{\rho_S} \mathbf{S}(t, \mathbf{a}) \boldsymbol{\kappa}_n, \quad n \in \mathcal{S}, \quad (3.2)$$

where $\rho_S \triangleq N_c/N_S$ ensures that, for purposes of a fair comparison, the total transmitted energy in any given symbol period is independent of the number of active nodes, and where $\mathbf{S}(t, \mathbf{a})$ is given in (2.30). Because of the block-diagonal properties of $\mathbf{S}(t, \mathbf{a})$, signal $\mathbf{s}_n(t)$ maintains the continuous-phase, constant envelope properties after $\boldsymbol{\kappa}_n$ is applied. The resulting signal is given by

$$\begin{aligned} \mathbf{s}_n(t) = & \sqrt{\rho_S} [x_1(t) \kappa_n[1], x_2(t - N_f T) \kappa_n[2], \dots \\ & \dots, x_{N_c}(t - (N_c - 1) N_f T) \kappa_n[N_c]]^T. \end{aligned} \quad (3.3)$$

Hence, by design, $\mathbf{s}_n(t)$ is a CPM signal for blocks of N_f consecutive symbols. As for the ST-CPM schemes given in Chapter 2 transitions between blocks should *not* be regarded as a violation of the CPM property since these are analogous to transitions between frames in CPM-type systems like GSM and Bluetooth. Hence, signature vectors can take the general form

$$\boldsymbol{\kappa}_n = [\kappa_n[1], \kappa_n[2], \dots, \kappa_n[N_c]]^T, \quad \|\boldsymbol{\kappa}_n\|_2^2 = 1, \quad 1 \leq n \leq N. \quad (3.4)$$

If, however, the constant-envelope property is desired throughout the entire transmission cycle, “constant-envelope” (ce) signature vectors

$$\boldsymbol{\kappa}_n^{\text{ce}} = \frac{1}{\sqrt{N_c}} [e^{j\phi_n[1]}, e^{j\phi_n[2]}, \dots, e^{j\phi_n[N_c]}]^T, \quad 1 \leq n \leq N, \quad (3.5)$$

are preferable. Of course, the unit-norm constraint is satisfied, i.e., $\|\boldsymbol{\kappa}_n^{\text{ce}}\|_2^2 = 1$. Optimization of the signature vectors is discussed in Section 3.2.2.

3.2.1 Detection of the Distributed ST-CPM Signals

Defining $\mathbf{K}_S \triangleq [\boldsymbol{\kappa}_{n_1}, \boldsymbol{\kappa}_{n_2}, \dots, \boldsymbol{\kappa}_{n_{N_S}}]$ and $\mathbf{g}_S \triangleq [g_{n_1}, g_{n_2}, \dots, g_{n_{N_S}}]^T$ we can re-write the received signal (3.1) as

$$\mathbf{r}(t) = \sqrt{\rho_S} \mathbf{X}(t) \mathbf{K}_S \mathbf{g}_S + \mathbf{n}(t) = \mathbf{X}(t) \mathbf{g}_S^{\text{eff}} + \mathbf{n}(t), \quad (3.6)$$

where $\mathbf{g}_S^{\text{eff}} \triangleq \sqrt{\rho_S} \mathbf{K}_S \mathbf{g}_S$ is an $N_c \times 1$ column vector. We observe that, from the destination node's perspective, distributed ST-CPM is seen as ST-CPM with co-located antennas and an effective channel $\mathbf{g}_S^{\text{eff}}$. Hence, coherent detection schemes (with estimation of $\mathbf{g}_S^{\text{eff}}$) and non-coherent detection schemes (without estimation of $\mathbf{g}_S^{\text{eff}}$) as devised in Chapter 2 are immediately applicable. In particular, complexity for detection (and channel estimation) remains the same as for ST-CPM with co-located antennas.

3.2.2 Optimization of Distributed ST-CPM

In this section, we consider the optimization of distributed ST-CPM. To this end, we first derive a suitable performance criterion. Based on this criterion, it is shown that optimization of the ST-CPM code and the signature vectors can be separated. Hence, next a numerical method for the optimization of the signature vector set \mathcal{K} is presented.

Performance Criteria for Optimization of Distributed ST-CPM As is common for ST transmission with co-located antennas [10] we choose the pairwise error probability (PEP) as the optimization criterion for distributed ST-CPM. Following the method described in [4], the Chernoff bound for the average PEP between two signals $\mathbf{x}(t)$ and $\tilde{\mathbf{x}}(t)$

can be derived as

$$P(\mathbf{x}(t) \rightarrow \tilde{\mathbf{x}}(t)) \leq \left(\prod_{i=1}^{r(\mathbf{A})} \frac{1}{\lambda_i(\mathbf{A})} \right) (4\mathcal{N}_0)^{-r(\mathbf{A})}, \quad (3.7)$$

where $\mathbf{A} \triangleq \rho_S \mathbf{K}_S^H \mathbf{V} \mathbf{K}_S$, and $\lambda_i(\mathbf{A})$ and $r(\mathbf{A})$ are the non-zero eigenvalues, and the number of non-zero eigenvalues of matrix \mathbf{A} , respectively. The $N_c \times N_c$ matrix \mathbf{V} is given by $\mathbf{V} = \text{diag}\{\Delta_1, \Delta_2, \dots, \Delta_{N_c}\}$ where $\Delta_i \triangleq \int_0^{N_f T} |x_i(t) - \tilde{x}_i(t)|^2 dt$. For use as design tools, and in a manner similar to [10], we define

$$d \triangleq r(\mathbf{A}) \quad \text{and} \quad G \triangleq \left(\prod_{i=1}^{r(\mathbf{A})} \lambda_i(\mathbf{A}) \right)^{1/r(\mathbf{A})}, \quad (3.8)$$

as the *diversity order* and *coding gain* of the distributed ST-CPM code, respectively.

Diversity Order: The maximum diversity order d is achieved when both \mathbf{V} and \mathbf{K}_S have full rank. When the number of active users is greater than the signature vector length, $N_S \geq N_c$, the diversity order is given by $d = r(\mathbf{K}_S^H \mathbf{V} \mathbf{K}_S) = N_c$ [64], and is guaranteed by proper *independent* design of the ST-CPM code and the signature vector set \mathcal{K} . When $N_S < N_c$ code design is more complicated because the ST-CPM code and the signature vectors must be jointly optimized [21]. In this case, the achievable diversity order is $d \geq N_S - (N_c - N_S)$ [64]. However, as for the linear-modulation case studied in [21], we found that signature vector sets \mathcal{K} designed assuming $N_S = N_c$ perform well for any N_S , achieving $d = N_S$ for $N_S < N_c$.

An important parameter in the optimization of signature vector sets is the number of users that we *assume* to be active, which we will denote as N_a . Once N_a has been selected the *maximum* diversity is unaffected by the true number of active users and is limited to $d = \min\{N_a, N_c\}$. We shall assume $N_a = N_c$ for the design of all signature set vector sets

\mathcal{K} .

Coding Gain: If we assume that the maximum diversity design criterion has been satisfied, i.e. both \mathbf{V} and $\mathbf{K}_{\mathcal{S}}$ have full rank, and $N_{\mathcal{S}} \geq N_c$, the coding gain can be re-written as [64]

$$\begin{aligned} G &= \rho_{\mathcal{S}} \left(\prod_{n_c=1}^{N_c} \lambda_{n_c}(\mathbf{K}_{\mathcal{S}}^H \mathbf{V} \mathbf{K}_{\mathcal{S}}) \right)^{1/N_c} \\ &= \rho_{\mathcal{S}} (\det\{\mathbf{V}\} \det\{\mathbf{K}_{\mathcal{S}} \mathbf{K}_{\mathcal{S}}^H\})^{1/N_c}. \end{aligned} \quad (3.9)$$

Equation (3.9) shows that optimizing the distributed ST-CPM code (by minimizing the bound on the maximum PEP in (3.7)), can be achieved by separately optimizing each of the component codes, i.e. the ST-CPM code and the signature vector set \mathcal{K} . The design of the ST-CPM code in [4] guarantees that \mathbf{V} is of full rank and maximizes $\det\{\mathbf{V}\}$, and therefore, we need only concentrate on the design of the signature vector set \mathcal{K} . In particular, the pertinent performance parameter given a subset \mathcal{S} of active nodes is the signature set coding gain (see (3.9))

$$K_{\mathcal{S}} \triangleq \det\{\mathbf{K}_{\mathcal{S}} \mathbf{K}_{\mathcal{S}}^H\}. \quad (3.10)$$

Before we move on to the actual optimization, it is useful to define the average distribution loss [21] as

$$L_{\text{ave}}(N_{\mathcal{S}}) \triangleq \frac{1}{K} \sum_{\mathcal{S}, \text{card}\{\mathcal{S}\}=N_{\mathcal{S}}} (\rho_{\mathcal{S}} K_{\mathcal{S}}^{1/N_c})^{-1}, \quad (3.11)$$

where $(\rho_{\mathcal{S}} K_{\mathcal{S}}^{1/N_c})^{-1}$ quantifies the loss in coding gain for distributed ST-CPM with a particular subset \mathcal{S} of $N_{\mathcal{S}}$ active nodes compared to ST-CPM with co-located antennas and $K \triangleq \binom{N}{N_{\mathcal{S}}}$ is the number of subsets $\mathcal{S} \in \mathcal{N}$.

Signature Vector Set Optimization Based upon the previous discussion, it follows that we can define the optimum signature set \mathcal{K}_{opt} as

$$\mathcal{K}_{\text{opt}} = \underset{\mathcal{K}}{\operatorname{argmax}} \left\{ \min_{\substack{\mathcal{S} \\ \operatorname{card}\{\mathcal{S}\}=N_a}} \{K_{\mathcal{S}}\} \right\}, \quad (3.12)$$

where the optimization is constrained

$$\text{subject to } \|\boldsymbol{\kappa}_n\|_2^2 = 1, \quad 1 \leq n \leq N \quad (3.13)$$

$$\text{subject to } \boldsymbol{\kappa}_n^{\text{ce}} = \frac{1}{\sqrt{N_c}} [e^{j\phi_n[1]}, e^{j\phi_n[2]}, \dots, e^{j\phi_n[N_c]}]^T, \quad (3.14)$$

$$1 \leq n \leq N$$

for the general set and the constant envelope set, respectively. Note that the cost function $K_{\mathcal{S}}$ is not convex in $\mathbf{K}_{\mathcal{S}}$, and thus the above optimization problem may have local minima.

We propose simulated annealing in tandem with a gradient search for numerical solution of the optimization problem. In particular, similar to a proposed simulated annealing algorithm for continuous spaces in [56, Ch. 10.9] we add a positive, logarithmically distributed random variable, proportional to the annealing temperature T_A , to the value of our optimization metric $K_{\mathcal{S}}$ and then use this value to determine which subset $\mathbf{K}_{\mathcal{S}}$ should be adapted. Once this subset is chosen, we employ a simple gradient algorithm for the update. This process is repeated in a number of iterations. While the adaptation in each iteration is not optimal, through simulated annealing the overall system is allowed to slowly converge to the global maximum. We select the simulated annealing algorithm for optimization of the signature vector sets, and show that the resulting sets provide performance approaching that of co-located antenna, however, any algorithm appropriate for the non-convex, continuous space optimization could be used to generate the signature sets.

For the general set, the vectors $\boldsymbol{\kappa}_n$ are directly updated and the constraint (3.13) is enforced after the update, as in [21]. The corresponding gradient is given by (assuming \mathbf{K}_S is an $N_c \times N_c$ full-rank matrix)

$$\boldsymbol{\Upsilon}_S = \frac{\partial K_S}{\partial \mathbf{K}_S^*} = K_S (\mathbf{K}_S^H)^{-1} \quad (3.15)$$

where \mathbf{K}_S^* is a matrix that contains the complex conjugate of the elements of \mathbf{K}_S .

For constant envelope sets we found that intrinsic incorporation of the constraint (3.14) into the search yields best results. Hence, the update is performed on the set $\boldsymbol{\Phi}_S \triangleq [\phi_{n_1}, \phi_{n_2}, \dots, \phi_{N_{N_S}}]^T$ of phase vectors $\phi_n \triangleq [\phi_n[1], \phi_n[2], \dots, \phi_n[N_c]]$. The gradient of K_S with respect to $\boldsymbol{\Phi}_S$ is defined as

$$\boldsymbol{\Upsilon}_S^{\text{ce}} = \frac{\partial K_S}{\partial \boldsymbol{\Phi}_S} = \frac{\partial K_S}{\partial \vec{\mathbf{K}}_S} \frac{\partial \vec{\mathbf{K}}_S}{\partial \boldsymbol{\Phi}_S} + \frac{\partial K_S}{\partial \vec{\mathbf{K}}_S^*} \frac{\partial \vec{\mathbf{K}}_S^*}{\partial \boldsymbol{\Phi}_S}, \quad (3.16)$$

where $\vec{\mathbf{K}}_S \triangleq \text{vec}\{\mathbf{K}_S\}$, $\vec{\mathbf{K}}_S^* \triangleq \text{vec}\{\mathbf{K}_S^H\}$, and

$$\begin{aligned} \frac{\partial K_S}{\partial \vec{\mathbf{K}}_S} &= K_S \text{vec}\{(\mathbf{K}_S^T)^{-1}\}, & \frac{\partial \vec{\mathbf{K}}_S}{\partial \boldsymbol{\Phi}_S} &= (j) \text{diag}\{\vec{\mathbf{K}}_S\}, \\ \frac{\partial K_S}{\partial \vec{\mathbf{K}}_S^*} &= K_S \text{vec}\{(\mathbf{K}_S^H)^{-1}\}, & \frac{\partial \vec{\mathbf{K}}_S^*}{\partial \boldsymbol{\Phi}_S} &= (-j) \text{diag}\{\vec{\mathbf{K}}_S^*\}. \end{aligned}$$

The pseudo-code for the proposed simulated annealing algorithm for solving the optimization problem in (3.12)-(3.14) is given in Figure 3.2. Initial and final values for the algorithm variables were found by experimentation [56]. The initial constant envelope set is chosen as an harmonic frame with optimized coefficients, cf. [65].

Finally, we note that an alternative to the deterministic generation of signature vector sets is the random selection of signature vectors at each node [21, 66]. This may be desirable in situations where the number of nodes is highly dynamic. We therefore also consider

the use of random sets whose constraints are equivalent to those for the deterministic general and constant envelope sets, i.e., the random vectors are uniformly distributed on a complex hypersphere [constraint (3.13)] and their elements have a uniform phase distribution [constraint (3.14)], respectively.

3.2.3 Simulation Results

In this section, we present simulation results for the proposed distributed ST-CPM codes employing signature sets designed with the algorithm in Figure 3.2 and the random generation method, respectively. In the following, we will refer to these sets as deterministic and random sets, respectively. First, we will consider the average distribution loss, L_{ave} [Eq. (3.11)], and the role that this expression can play as an indicator of the performance of the different signature vector sets. Then, we will evaluate the average bit error rate (BER) for relay communication with distributed ST-CPM. Finally, we compare distributed ST-CPM with the linear-modulation scheme from [21]. For space limitations, we restrict ourselves to ST-CPM with $N_c = 2$ and signature sets optimized for $N_a = N_c = 2$.

In Figure 3.3, the average distribution losses of deterministic and random sets are shown for $N_S = 2, 3$ and 5 active nodes (the acronym “CE” indicates constant envelope sets). The distribution loss for random sets is independent of the number of total nodes because each node randomly generates its own signature vector when it becomes active. The deterministic general sets consistently yield the lowest average distribution loss. Furthermore, Figure 3.3 shows that as the number of active nodes, N_S , is increased the performance losses incurred by enforcing the constant envelope criterion becomes less significant. Random sets appear an efficient alternative for relatively large numbers of nodes. However, we note that results for the average distribution loss may not completely characterize the performance of randomly generated signature sets. More specifically, although the performance

1. Initialization:

Set $i = 0, T_A = T_0, \mu = \mu_0$

Generate an initial set of $N_c \times 1$ vectors

Gen: κ_n are random vectors with $\|\kappa_n\|_2 = 1$

CE: κ_n^{ce} are from an optimized harmonic frame [65]

2. Find worst set \mathcal{S}_{\min} :

$$\mathcal{S}_{\min} = \underset{\substack{\mathcal{S} \\ \text{card}\{\mathcal{S}\}=N_a}}{\text{argmin}} \{G_{\mathcal{S}} - T_A \log(\text{rand}(1))\}$$

$$K'_{\mathcal{S}_{\min}} = K_{\mathcal{S}_{\min}}$$

3. Adaptation:

Gen: $K'_{\mathcal{S}_{\min}} = K_{\mathcal{S}_{\min}} + \mu \Upsilon_{\mathcal{S}_{\min}}$

CE: $\Phi'_{\mathcal{S}_{\min}} = \Phi_{\mathcal{S}_{\min}} + \mu \Upsilon_{\mathcal{S}_{\min}}^{\text{ce}}$

4. Update Signature Set:

Gen: $\kappa_n = \frac{\kappa'_n}{\|\kappa'_n\|_2}, \quad n \in \mathcal{S}_{\min}$

CE: $\kappa_n^{\text{ce}} = \frac{1}{\sqrt{N_c}} \left[e^{j\phi'_n[1]}, \dots, e^{j\phi'_n[N_c]} \right]^T, n \in \mathcal{S}_{\min}$

5. Check Update:

Recalculate $K_{\mathcal{S}_{\min}}$

If $\frac{|K_{\mathcal{S}_{\min}} - K'_{\mathcal{S}_{\min}}|}{|K_{\mathcal{S}_{\min}}|} > \epsilon$ then $\mu := \lambda\mu$ and goto 2.

6. Update Annealing:

If $T_A > T_f$, set $T_A := (1 - \zeta)T_A$ and goto 2, otherwise goto 7.

7. End:

κ_n or $\kappa_n^{\text{ce}}, 1 \leq n \leq N$, is the desired set $\mathcal{K}_{\text{anneal}}$.

Gen : general signature set

CE: constant envelope signature set

$\mu_0 = 10^{-2}, \lambda = 1 - 10^{-5}, \epsilon = 10^{-5}, T_0 = 10^{-2}, T_f = 10^{-6}, \zeta = 0.7$

rand(1) returns one sample of a $[0, 1)$ uniformly distributed random variable

Figure 3.2: Annealing algorithm for signature set generation.

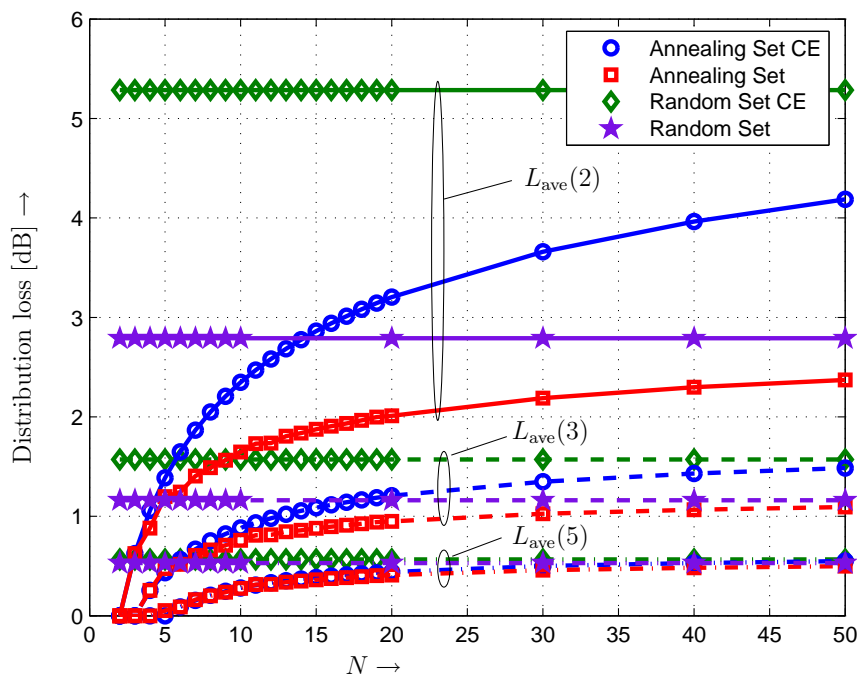


Figure 3.3: Average distribution losses as a function of the total number of nodes N , and the number of active nodes $N_S = 2, 3, 5$. Deterministic signature vector sets optimized for $N_a = N_c = 2$ active nodes and random signature vector sets are considered. ‘CE’ indicates constant envelope sets.

of the randomly generated signature sets may be comparable to the performance of the deterministically generated signature sets on average, when transmissions are considered on individual basis random signature sets have a high probability of producing a higher distribution loss than the *worst-case* distribution loss of a deterministic set. Therefore, randomly generated sets may only be desirable for highly dynamic networks.

We now turn to BER results. We assume that all relay nodes have an equal probability of being active and the BER is averaged with respect to the fading gain distribution. As an illustration we adopt the CPM scheme with the parameters $M = 4, h = 1/4$ and a 1REC phase pulse. The underlying ST-CPM code is given in [4, Table I] for $N_c = 2$ co-located antennas, resulting in a diversity order $d = 2$. Unless stated otherwise, optimal coherent

detection of ST-CPM is assumed.

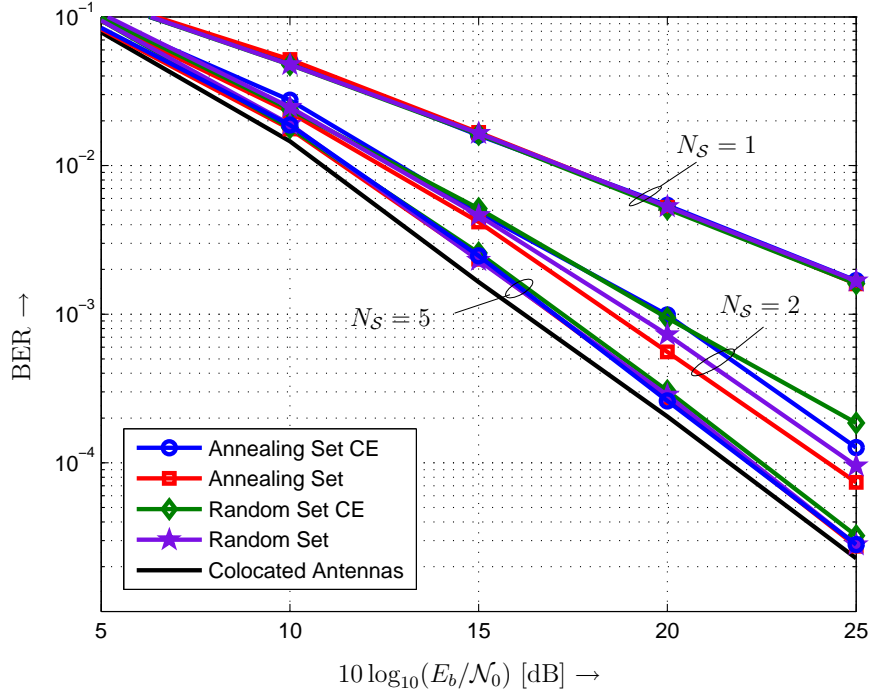


Figure 3.4: Average BER of a distributed ST-CPM code versus $10 \log_{10}(E_b/N_0)$ for a network with $N = 30$ nodes and different numbers of active nodes N_S . Deterministic signature vector sets optimized for $N_a = N_c = 2$ active nodes and random signature vector sets are considered. ‘CE’ indicates constant envelope sets. The ST-CPM code is optimized for $N_c = d = 2$ with the CPM parameters $M = 4$, $h = 1/4$, and a 1REC phase pulse as given in [4, Table I].

First, we only consider the relay phases, i.e., transmission from relay nodes to the destination node. Figure 3.4 shows the average BER vs. E_b/N_0 ($E_b = E_s N_c / \log_2(M)$ denotes the received energy per bit) for the distributed ST-CPM scheme with $N = 30$. Results for deterministic and random sets are shown. For comparison purposes the results for co-located antennas are also included. This figure illustrates that both signature set designs yield a network BER performance that approaches that of one node with $N_c = 2$ co-located antennas when $N_S \geq N_c$. The simulation results also confirm the performance ordering of the different signature set designs given by the distribution loss results shown

in Figure 3.3. More specifically, the results in Figure 3.3 predict losses for the constant envelope set, the general random set, and the constant envelope random set of 0.6, 1.3, and 3.1 dB with respect to the designed general set for $N_S = 2$, and similarly the BER results in Figure 3.4 indicate losses of 0.6, 1.3, and 2.3 dB when $E_b/\mathcal{N}_0 = 25$ dB. The single discrepancy may be attributed to the fact that the distribution loss was derived under the assumption of high SNR. Furthermore, while the distributed ST-CPM scheme always maintains a diversity order of $d = N_c$ when $N_S \geq N_c$, we have found from simulations for various values of $N_c > 2$, which cannot be shown due to space constraints, that a diversity order equal to the number of active user $d = N_S$ is achieved when $N_S < N_c$.

Next, we consider two phase transmission in a distributed network. In the first phase, a relay node conserves energy by listening for transmission from the source node with probability p_l . In the second phase, nodes that were listening in the first phase and able to correctly decode the source's transmission retransmit to the destination node (i.e. the number of active nodes (N_S) in the second phase is random). The average received energy per bit at each listening relay node is assumed to equal E_b . Figure 3.5 shows the results for a two phase network composed of $N = 30$ nodes. Nodes in this network listen with probability $p_l = 1/3, 1/5$, and $1/7$. We observe that the signature sets provide very similar performances, which closely approach that for the co-located antenna system. For example, for $p_l = 1/3$ and $p_l = 1/5$ the respective BER curves run parallel, i.e. full diversity is achieved by the distributed system, and the losses are only 0.5, and 1.1 dB with respect to a co-located antenna system.

The above example considered transmission with a spectral efficiency of $2/3$ bit/s/Hz, which is likely sufficient for many network applications with low-power transceivers. If higher spectral efficiencies are desired, the proper choice of the parameters M , h , and pulse shape $q(t)$ is critical for ST-CPM, since, different from linear modulation, the signal

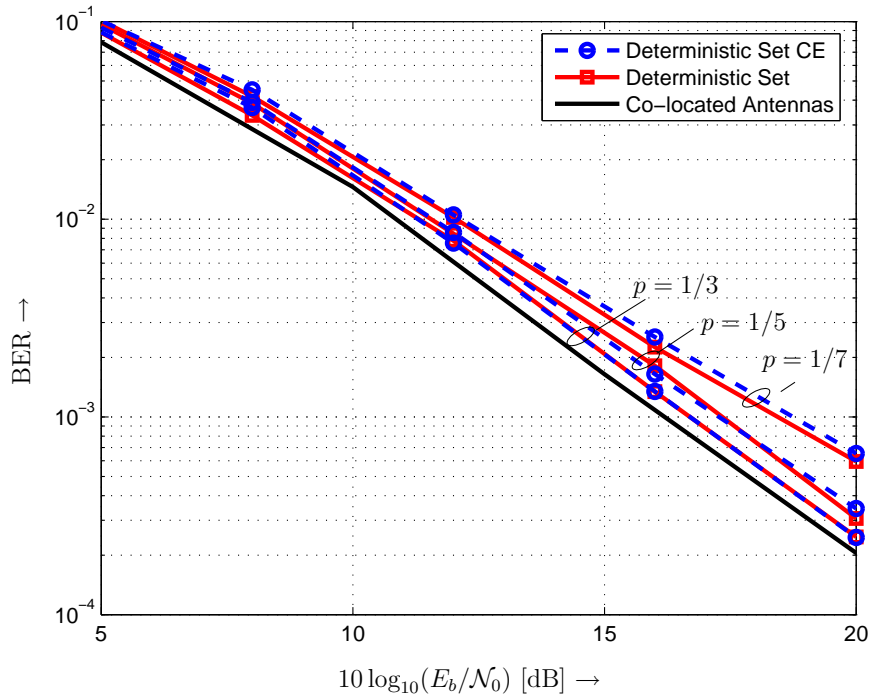


Figure 3.5: Average BER of a distributed ST-CPM code versus $10 \log_{10}(E_b/\mathcal{N}_0)$ for a network with $N = 30$ nodes where the number of active nodes N_S depends on the probability p that any given node is listening for the source's transmission. Deterministic signature vector sets optimized for $N_a = N_c = 2$ active nodes and random signature vector sets are considered. 'CE' indicates constant envelope sets. The ST-CPM code is optimized for $N_c = d = 2$ with the CPM parameters $M = 4$, $h = 1/4$, and a 1REC phase pulse as given in [4, Table I].

bandwidth increases with M . Favorable parameter combinations are given in [67, Tables 5.2-5.4]. At the same time, the PAPR advantage of ST-CPM over linear ST modulation increases with larger spectral efficiency, which renders distributed ST-CPM an interesting solution also for this scenario.

3.3 Energy Consumption of Distributed ST Coding Methods

In this section, we analyze the energy savings made possible if the modulation technique underlying a distributed ST coding scheme is switched from linear modulation to CPM. The energy savings that are offered by CPM are savings of energy in the hardware of the device; the constant-envelope property of CPM guarantees a PAPR of one and allows for the use of non-linear, energy-efficient components. Typically, the performance of similar communication schemes is compared with respect to the received radiant energy. If, however, we wish to perform a fair comparison of linear modulation (LM) schemes with CPM schemes, we must perform this comparison with respect to both the energy that is radiated *and* the energy that is consumed by device hardware. Indeed, recently, some effort has been made to evaluate and compare schemes based upon both transmitted and circuit energy usage [68]-[71]. These efforts have taken two different approaches: analysis of the power consumption of the entire transceiver [68], and analysis of the power consumption of a specific element of the transceiver [69]-[71]. Cui *et al.* [68] adopted the first approach and analyzed the total energy consumption of a transmitter and receiver for coded and uncoded M -ary Quadrature Amplitude Modulation (MQAM) and M -ary Frequency-Shift Keying (MFSK) systems in order to minimize overall energy consumption by optimizing constellation size and transmission time. In this case, synthesizing the entire transceiver becomes a concern; state-of-the art components can be selected from the literature, however their inter-operability cannot be guaranteed. Therefore, Li-Chung and Krogmeier [69], Liang *et al.* [70], and Rapp [71] chose to study the energy consumption of a single element of the transceiver - the power amplifier, which is one of the largest consumers of energy in the transmitter. Practical power amplifiers have non-linear characteristics (resulting in

signal distortion) and, depending on classification, can consume varying amounts of energy in relation to the required transmitted power. The authors of these works compared the energy consumption of LM and CPM schemes in a traditional communication context (single transmitter, single receiver, adjacent channel interference, and an additive white Gaussian noise (AWGN) channel). In addition, since the publication of these works power amplifiers with a higher degree of linearity and a lower energy consumption have become available.

In this section, we study the energy consumption of the power amplifier for the distributed ST coding scheme proposed earlier in the chapter, and a distributed ST coding scheme built upon linear modulation (distributed ST-LM) [21]. We perform a detailed study of the performance of the distributed schemes in the context of an ad-hoc sensor network, using state-of-the-art power amplifier models, and a channel model appropriate for a wireless sensor network. These performance comparisons quantitatively show that distributed ST-CPM offers significant performance gains over distributed ST-LM based schemes for a variety of power amplifier implementations.

3.3.1 Distributed ST Coding Overview

In this section, we briefly overview the distributed ST-LM coding scheme [21] that we use for comparison. Then we introduce the power amplifier characteristics relevant to the distributed ST-LM, and distributed ST-CPM coding schemes. We assume the same relay network as outlined in Section 3.1.

Distributed ST-LM Code The distributed ST-LM [21] and ST-CPM [72] codes considered here have very similar constructions. The distributed ST-LM code also consists of a ST matrix containing the information from the source node, and a signature vector unique to the individual relay node, $n \in \mathcal{N}$. Active relay nodes employing the distributed

ST-LM code transmit the following signal in successive $N_B \geq N_c$ symbol intervals ²

$$\mathbf{s}_n[k] = \sqrt{\rho_S} \mathbf{B}[k] \boldsymbol{\kappa}_n, \quad n \in \mathcal{S}, \quad (3.17)$$

where $\mathbf{s}_n[k] \triangleq [s_{n,1}[k] s_{n,2}[k] \cdots s_{n,N_B}[k]]^T$, $k \in \mathbb{Z}$ is a discrete time index, $\rho_S = N_c$ is a normalization constant and $\mathbf{B}[k] \in \mathcal{B}$ is an $N_B \times N_c$ matrix. The signature vectors, $\boldsymbol{\kappa}_n \in \mathcal{G}$, $n \in \mathcal{N}$ are unit-norm $\|\boldsymbol{\kappa}_n\|_2^2 = 1$ vectors of length N_c where \mathcal{G} denotes the set of signature vectors. The code \mathcal{B} is normalized such that $\mathcal{E}\{\mathbf{B}^H[k] \mathbf{B}[k]\} = (N_B/N_c) \mathbf{I}_{N_c}$. Thus, the average energy transmitted per node and symbol interval is $\mathcal{E}\{\mathbf{s}_n^H[k] \mathbf{s}_n[k]\}/N_B = 1$.

After the signal $\mathbf{s}_n[k]$ is generated it is fed into a root raised cosine filter with roll-off factor α (we assume $\alpha = 0.5$) to limit the signal bandwidth. This filtered signal is input into a gain unit and multiplied by a factor, γ , to give the signal an average power of \bar{P}_{in} and then fed into the power amplifier. After amplification the signal is perturbed by fading and AWGN. The filtered, the amplified, and the received signals are given by

$$s_n^{\text{F}}(t) = \sum_{k=-\infty}^{\infty} \sum_{i=1}^{N_B} s_{n,i}[k] f(t - (kN_B + i - 1)T), \quad (3.18)$$

$$s_n^{\text{A}}(t) = \mathcal{F}(|\gamma s_n^{\text{F}}(t)|) \frac{s_n^{\text{F}}(t)}{|s_n^{\text{F}}(t)|}, \quad (3.19)$$

$$r(t) = \sum_{n \in \mathcal{S}} (g_n s_n^{\text{A}}(t)) + n(t), \quad (3.20)$$

respectively. Here, T is the symbol duration, $\mathcal{F}(\cdot)$ is an amplification function that is dependent upon the power amplifier (described in Section 3.3.2), $f(t)$ denotes the impulse response of the root raised cosine filter, the channel gains g_n are modelled as independently and identically distributed (i.i.d.) zero-mean complex Gaussian random variables with unit variance, and the noise term $n(t)$ is modelled as a zero mean AWGN process with

²Note that the normalization constant has been modified from [21, see Eq. (1)] to allow for fair comparison of power consumption in the power amplifier.

power spectral density \mathcal{N}_0 . The received signal is filtered by another root raised cosine filter (matched to the transmit filter) and sampled. Maximum-likelihood decoding for the underlying ST code is used to decide on the transmit symbols (see [21] for details).

Distributed ST-CPM Code The details of the distributed ST-CPM scheme are given in Section 3.2. The ‘constant envelope’ signature set is employed. When $E_s = 1$, (i.e. the energy per symbol is set to one) the average transmitted energy per node and symbol interval is $\mathcal{E}\{\int_0^{N_f T} \mathbf{s}_n^H(t) \mathbf{s}_n(t) dt\} / N_f = 1$.

The CPM signal $\mathbf{s}_n(t)$ given in (3.2) is input into a gain unit to give the signal an average power of \bar{P}_{in} before amplification. Thus, the amplified signal, given by the vector $\mathbf{s}_n^A(t) \triangleq [s_{n,1}^A(t), s_{n,2}^A(t), \dots, s_{n,N_c}^A(t)]^T$, and the received signal are given by

$$s_{n,i}^A(t) = \mathcal{F}(|\gamma s_{n,i}(t)|) s_{n,i}(t), \quad 1 < i < N_c, \quad (3.21)$$

$$\mathbf{r}(t) = \sum_{n \in \mathcal{S}} (g_n \mathbf{s}_n^A(t)) + \mathbf{n}(t), \quad (3.22)$$

respectively, and $\mathbf{n}(t) \triangleq [n_1(t), n_2(t), \dots, n_{N_c}(t)]$.

3.3.2 Power Amplifier Modeling

The study of CPM for low power applications is usually motivated by the ability to use high efficiency, non-linear Class C amplifiers instead of the lower efficiency, highly linear Class A, or AB amplifiers that are typically used for linear modulations. However, the performance of a power amplifier can not be characterized by one parameter. The efficiency of the power amplifier is completely dependant upon its operating point (see Section 1.2.2 for more details). Therefore, to get a true measure of the energy consumption savings that a switch to a CPM based scheme will yield from an efficiency perspective we need to analyze the power amplifier over its entire operating range. For this purpose, in this work

we consider a low power Class AB power amplifier designed for mobile wireless terminals using the IEEE 802.11a and 802.11n standards and utilizing a low supply voltage [5], and a low power Class C amplifier [6]. The transfer characteristics of these amplifiers are shown in Figure 3.6 [5] and Figure 3.7 [6]. These characteristics include drain efficiency (η), power added efficiency (PAE), output power (P_{out}), dc power supplied to the power amplifier (P_{dc}), and power gain ($P_{\text{out}} - P_{\text{in}}$ (dB)) all plotted with respect to input power. For both power amplifiers shown in these figures drain efficiency and power added efficiency are *functions* of input power. In fact, drain efficiency values vary from 0 – 24% for the Class AB power amplifier and from 5 – 56% for the Class C amplifier.

Amplifier linearity also motivates the study of the power amplifier over its entire operating range. Obviously, the Class C amplifier operates primarily as a non-linear device (although it may have a region of linear operation at low power, see Figure 3.7), however, the Class AB amplifier also has a region of non-linear operation (see Figure 3.6). Non-linear amplification causes signal distortion and bandwidth expansion for linear modulations. Although these effects do not render operation in these regions impossible, performance losses due to non-linear amplification of a linear signal often mean that power amplifiers employ a *back-off* region in which they do not operate. These problems are compounded for distributed ST codes employing linear modulations because signal multiplexing leads to large values of PAPR. Distributed ST-LM schemes can compensate for large PAPR values by using a more linear power amplifier (increased energy cost) or by employing a larger back-off region (reducing the maximum output power of the power amplifier resulting in a smaller region of coverage). Employing CPM avoids the energy consumption/coverage range tradeoff.

Thus, due to the dependence of the efficiency and linearity of the power amplifier upon the operating point of the power amplifier we study of the performance of the amplifier

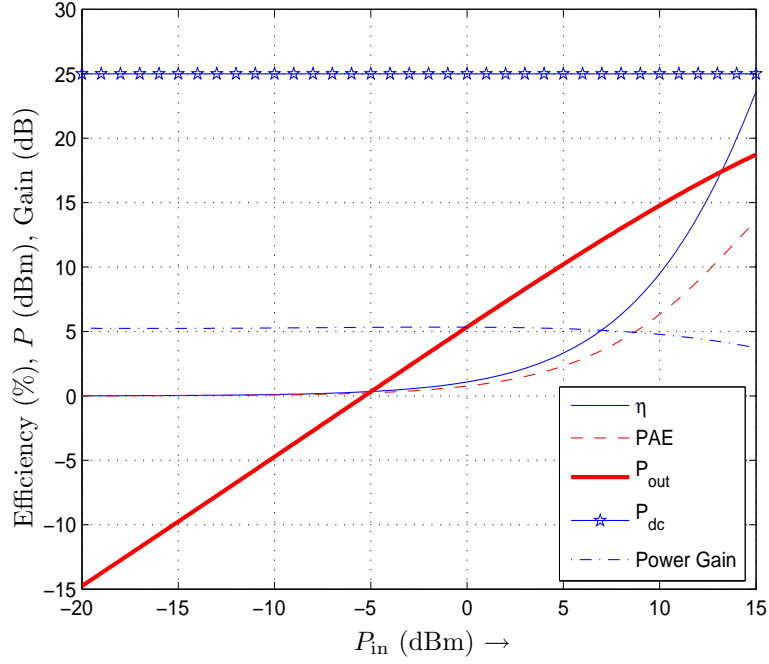


Figure 3.6: Drain efficiency, η , (%), power added efficiency, PAE, (%), output power, P_{out} , (dBm), dc power supplying the power amplifier, P_{dc} , (dBm), and power gain - output power minus input power (dB) vs. input power for the Class AB power amplifier designed by Carls *et al.* [5].

over its entire transfer characteristic. In general form, the input signal (that determines the voltage/power of the power amplifier output) is given by

$$v_{in}(t) = V_{in}(t) \cos(2\pi f_c t + \theta_{in}(t)), \quad (3.23)$$

where $V_{in}(t)$ is the non-negative envelope of the input signal, f_c is the carrier frequency, and $\theta_{in}(t)$ is the phase of the input signal. The resulting RF output of the power amplifier is given by

$$v_{out}(t) = \mathcal{F}(V_{in}(t)) \cos(2\pi f_c t + \theta_{in}(t)), \quad (3.24)$$

where the transformation $\mathcal{F}(\cdot)$ is dependent upon the structure and properties of the par-

ticular power amplifier, and $P_{\text{in}}(t) = (V_{\text{in}}(t))^2$, and $P_{\text{out}}(t) = \mathcal{F}^2(V_{\text{in}}(t))$ (P_{out} as a function of P_{in} , independent of time, is shown for the Class AB and Class C power amplifiers in Figs. 3.6 and 3.7, respectively). We note that the power amplifiers used in this chapter, from the recent references [5, 6], cause only amplitude distortion in contrast to the power amplifiers used in [69] and [71] which cause both phase and amplitude distortion.

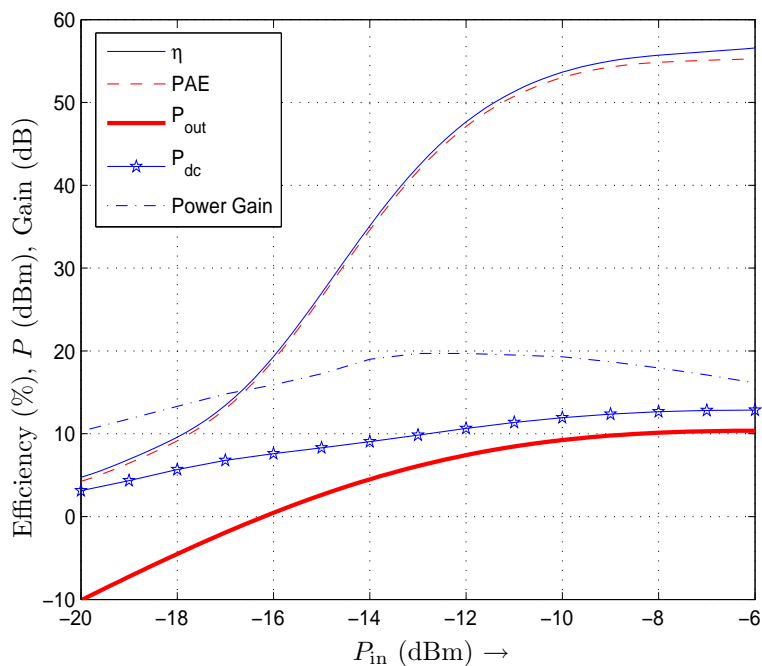


Figure 3.7: Drain efficiency, η , (%), power added efficiency, PAE, (%), output power, P_{out} , (dBm), dc power supplying the power amplifier, P_{dc} , (dBm), and power gain - output power minus input power (dB) vs. input power for the Class C power amplifier designed by Cao *et al.* [6].

3.3.3 Energy Consumption Analysis

When comparing different communication schemes it is conventional to use E_b/\mathcal{N}_0 as a performance metric, where E_b is the received energy per bit. However, in applications where device lifetime is an important consideration (e.g. wireless sensor networks) we seek

a performance metric that includes both the energy that is radiated by a device, and the energy that is consumed by the device's hardware. In this section, we will investigate one previously proposed metric (total power amplifier energy) and use it as a springboard to propose a new, more generic performance metric (transmission distance).

Total Energy To provide a performance indicator that encompassed both transmitted energy and energy consumed by hardware Liang *et al.* [70] proposed total energy per transmitted bit (where total energy refers to the total energy used by the power amplifier), which is given by

$$\begin{aligned}
 E_t &= \frac{\bar{P}_t}{R_b} = \frac{(\bar{P}_{\text{dc}} + \bar{P}_{\text{in}})}{R_b} \\
 &= \frac{\bar{P}_{\text{out}}(1 + (1 - \text{PAE})P_{\text{dc}}/\bar{P}_{\text{out}})}{R_b} \\
 &\triangleq E_{b'} + E_c
 \end{aligned} \tag{3.25}$$

where $E_{b'} \triangleq \bar{P}_{\text{in}}/R_b$ is the transmitted energy per bit, E_c denotes the energy that is consumed in the amplifier in order to transmit a bit with energy $E_{b'}$, and R_b denotes the bit rate.

The authors of [69]-[71] evaluate the performance of their communication schemes using the ratio of total energy E_t to total losses N_L , where N_L includes path loss, and the noise power spectral density \mathcal{N}_0 . Thus, the ratio $E_{b'}/N_L$ is equivalent to the received signal-to-noise ratio E_b/\mathcal{N}_0 . The ratio E_t/N_L is generated using a two step process. First, bit error rate (BER) curves are generated for a range of values of total loss N_L and over the operating range of the amplifier (P_{in}). Then, using these curves values of maximum allowable total loss N_L are found for given input powers P_{in} and a target BER. Unlike E_b/N_0 , the resulting values of E_t/N_L are dependent upon P_{in} . Thus, inherent in each value of E_t/N_L is information pertaining to the input/output characteristic of the power

amplifier and a strict limitation on transmission loss. A comparison of different power amplifiers is hampered because information regarding the efficiency of the amplifier (i.e., radiated energy $E_{b'}$ vs. circuit energy E_c) and the total loss N_L is obscured because of the ratio form of this metric. Therefore, in the next section, we introduce a new performance metric based upon transmission distance.

Transmission Distance In order to determine the maximum possible transmission distance of the communication scheme, we first look to the minimum permissible received power allowable for a targeted BER, which is characterized by the receiver sensitivity. The required receiver sensitivity is given by

$$P_{\text{req}}(\text{BER}, P_{\text{in}}) = \mathcal{N}_0 + N_F + 10 \log_{10}(B) + E_{b'}(P_{\text{in}}) - N_L(\text{BER}, P_{\text{in}}) + R_b \quad (\text{dB}), \quad (3.26)$$

where \mathcal{N}_0 , N_F , and B are the thermal noise power for a 1 Hz noise equivalent bandwidth (-174 dBm), the receiver noise figure, and the noise equivalent bandwidth, respectively. As previously mentioned $E_{b'}$ is the energy at the output of the power amplifier, and N_L is the total system loss (path loss, and noise power spectral density). If the power amplifier transmits with energy $E_{b'}$ and the receiver has a sensitivity $P_{\text{req}}(\text{BER}, P_{\text{in}})$ then the maximum loss the system can tolerate while maintaining a given BER is

$$\begin{aligned} L_{\text{max}}(\text{BER}) &= E_{b'}(P_{\text{in}}) + R_b - P_{\text{req}}(\text{BER}, P_{\text{in}}) + G \quad (\text{dB}), \\ &= N_{L(\text{max})}(\text{BER}, P_{\text{in}}) - \mathcal{N}_0 - N_F + G \quad (\text{dB}), \end{aligned} \quad (3.27)$$

where G includes any gains and losses generated by the transmitter or receiver, and $N_{L(\text{max})}$ is the signal loss allowable in order to achieve a given BER at a set input power to the power amplifier. Attenuation during transmission is given by the general path loss model

[73]

$$PL = 10n \log \left(\frac{d}{d_0} \right) + PL(d_0) + X_\sigma \quad (\text{dB}), \quad (3.28)$$

where $PL(d_0) = 20 \log \left(\frac{4\pi d_0}{\lambda} \right)$ is the path loss at a reference distance d_0 that is in the far field of the transmitting antenna (we assume a small antenna and a value of $d_0 = 1$ m [73]), and λ, n , and X_σ are the wavelength of the transmitted signal, the path loss exponent, and a log-normal fading shadowing term given by a zero mean Gaussian random variable. Therefore, the maximum allowable path loss is a function of BER and power amplifier input power, and is given by

$$PL_{\max}(\text{BER}) = L_{\max}(\text{BER}) \quad (\text{dB}). \quad (3.29)$$

Thus, we can upper bound the transmission distance for a target BER at a given input power by

$$d_{\max}(\text{BER}, P_{\text{in}}) = d_0 10^{\left(\frac{N_{L(\max)}(\text{BER}, P_{\text{in}}) + G - N_T - N_F - 10 \log_{10}(B) - PL(d_0) - X_\sigma}{10n} \right)} \quad (\text{dB}). \quad (3.30)$$

3.3.4 Simulations

In this section, we compare the performance of the distributed ST-LM and distributed ST-CPM schemes outlined in Sections 3.3.1. These distributed ST schemes employ different classes of state-of-the-art power amplifiers as described in Section 3.3.2. The performance comparisons are performed using BER and the maximum transmission distance metric detailed in Section 3.3.3.

We assume that the network we employ is populated by $N = 30$ potential relay nodes, that all relay nodes have an equal probability of being active, and that BER is averaged with respect to fading gain distribution. The ST codes are designed for a signature vector

length of $N_c = 2$. The distributed ST-LM scheme uses BPSK modulation, Alamouti's ST block-code (STBC), and a signature set generated using a gradient search [21]. The normalized bandwidth of the BPSK signal after it has passed through the root raised cosine filter is $BT = 1.5$. To obtain the same data rate for the distributed ST-CPM scheme, the CPM parameters are chosen as $M = 4, h = 1/4$, and a 1REC phase pulse was used, which has a normalized bandwidth of $B_{99\%}T = 1.54$. The underlying ST-CPM code is given in Table 2.1.

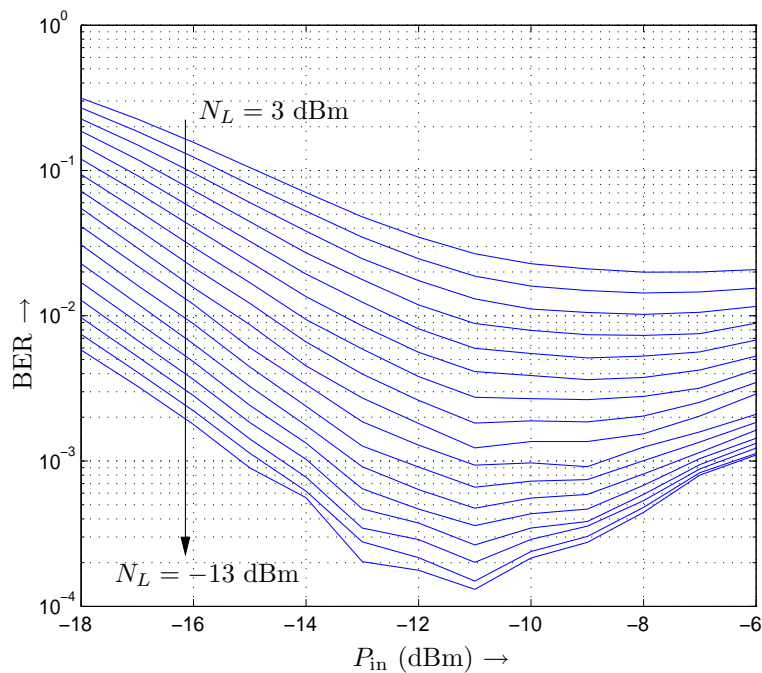


Figure 3.8: BER performance vs. input power P_{in} (dBm) of the distributed ST-LM code for different values of total loss (N_L). Class C amplifier [6].

BER Figure 3.8 shows the average BER performance vs. amplifier input power P_{in} (dBm) of the distributed ST-LM coding scheme for different values of total loss (N_L) when the Class C amplifier is employed [6]. For this example, $N_s = 5$ of the 30 potential relay nodes are active in any given transmission. The curves shown in Figure 3.8 are convex in

shape.

Initially, increasing the input power has the expected effect of reducing the incidence of bit errors, however, continuing to increase the input power towards the maximum operating point of the amplifier sees the number of bit errors increase once again. The increase in bit errors occurs because the amplifier operates as a non-linear device at high values of input power, and non-linear amplification causes signal distortion and bandwidth expansion for schemes based upon linear modulation. Increasing the size of the distributed ST-LM block code, \mathcal{B} , and the length of the signature vector, κ , has the effect of increasing the PAPR of the resulting signal, $\mathbf{s}(t)$, and thereby lowering the point at which the BER performance begins to degrade. In contrast, while the performance of the ST-CPM scheme at low input power resembles that of the ST-LM scheme, at high input power and for BERs greater than 10^{-4} the BER of the ST-CPM remains constant rather than increasing as the ST-LM scheme does. Finally, we note that the results for the distributed ST-LM employing a Class AB amplifier are similar in shape to those shown in Figure 3.8, with a less pronounced BER degradation near the amplifier's maximum operating point.

Transmission Distance We assume operation in the ISM band at 2.4 GHz and $d_0 = 1$ m which gives $PL(d_0) = 40.05$ dB. We set $G = 20.4$ dB and $N_F = 19.0$ dB as specified by [74], which details a receiver front-end design for wireless sensor networks. Values of the path loss exponent, n , are dependent upon the environment in which the network operates. In an office environment the value of n can vary from $n = 1.9$ to $n = 6.3$ [75], and the value of X_σ can vary from $X_\sigma = 3.0$ to $X_\sigma = 14.1$ dB [73]. We select $n = 2.5$ and $X_\sigma = 3.0$ dB for the results shown here. Following the IEEE 802.11 standard, we assume a symbol duration of $4 \mu\text{s}$. We note that any change in the parameters selected here will change the margin of performance improvement from one scheme to another but not the relative performance ordering.

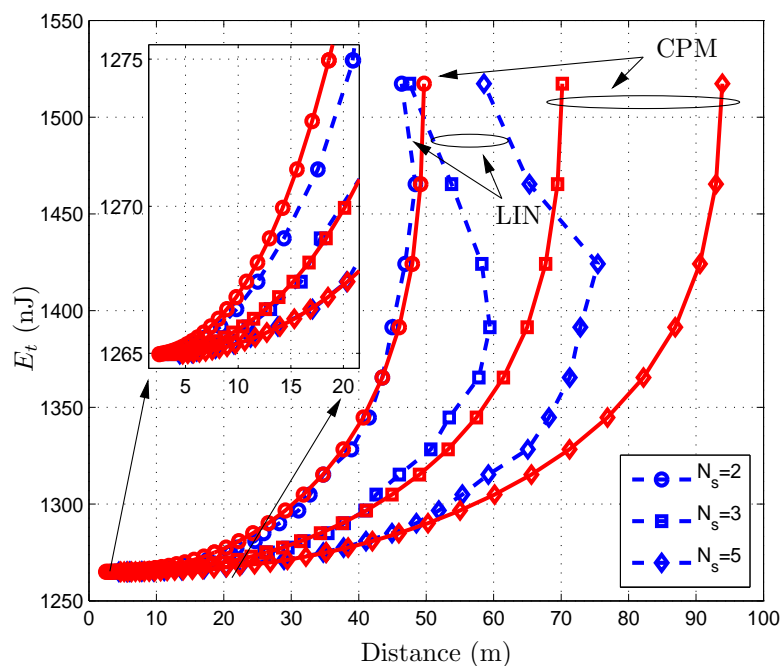


Figure 3.9: Total energy (nJ) per active node, per symbol vs. maximum transmission distance (m) to achieve a BER of 10^{-3} for a distributed ST-LM scheme ('LIN') and a distributed ST-CPM scheme ('CPM'). The number of active nodes includes $N_s = 2, 3,$ and 5 . A Class AB amplifier [5] is employed.

First, we consider the upper bound on transmission distance (m) vs. total energy consumption (nJ) per symbol in order to achieve a BER of 10^{-3} . Results for the Class AB power amplifier are shown in Figure 3.9, and for the Class C power amplifier in Figure 3.10. Results for the distributed ST-LM scheme are denoted 'LIN' and results for the distributed ST-CPM coding scheme are denoted 'CPM'. Curves for $N_s = 2, N_s = 3,$ and $N_s = 5$ active nodes are shown. Note that for the purpose of comparing the results of a differing number of active nodes the total energy consumption shown in the following figures is per active node, however, the corresponding transmission distances reflect the total energy transmitted by all active nodes (i.e. the results for $N_s = 5$ have a factor $5/2$ higher total energy consumption than those for $N_s = 2$). Figures 3.9 and 3.10 clearly illustrate the negative effects of operating the distributed ST-LM scheme in the non-linear region of the

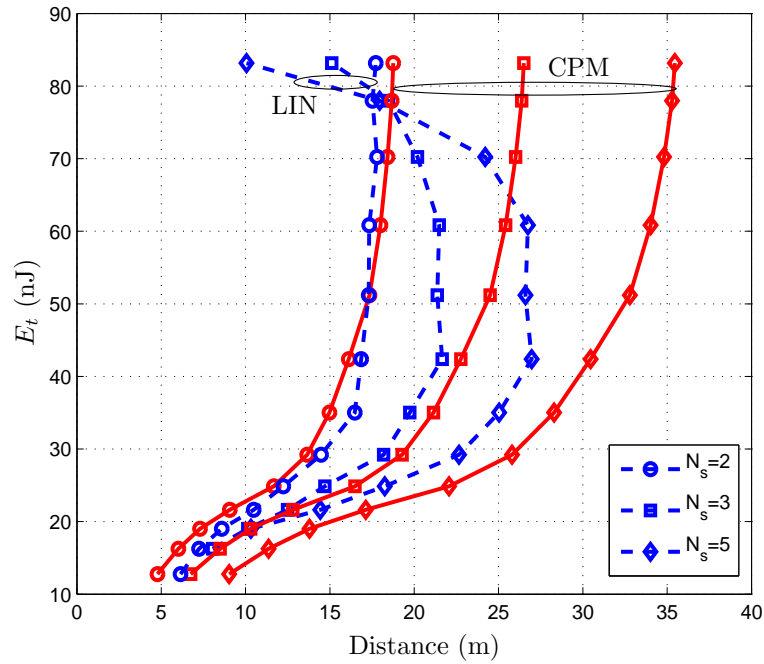


Figure 3.10: Total energy (nJ) per active node, per symbol vs. maximum transmission distance (m) to achieve a BER of 10^{-3} for a distributed ST-LM scheme ('LIN') and a distributed ST-CPM scheme ('CPM'). The number of active nodes includes $N_s = 2, 3,$ and 5 . A Class C amplifier [6] is employed.

amplifier. After an initial expansion in the range of coverage of the distributed ST-LM scheme, the coverage range begins to *shrink* with increasing transmit energy. It should be noted that although the performance loss is worse for the less linear Class C amplifier the highly linear Class AB amplifier also suffers a performance loss. In Figure 3.10, we see that the performance of the distributed ST-LM scheme in the saturation range of the amplifier actually worsens as the number of active nodes increases. This performance loss occurs because each of the active nodes is transmitting and amplifying a unique signal (due to the use of the signature vector). Therefore, as the number of active nodes increases so too does the likelihood that one or more of the active nodes will transmit a signal with a high PAPR. At the receiver the resulting signal, which is the summation of the N_s unevenly amplified signals, suffers the effects of both magnitude and phase distortion for which the

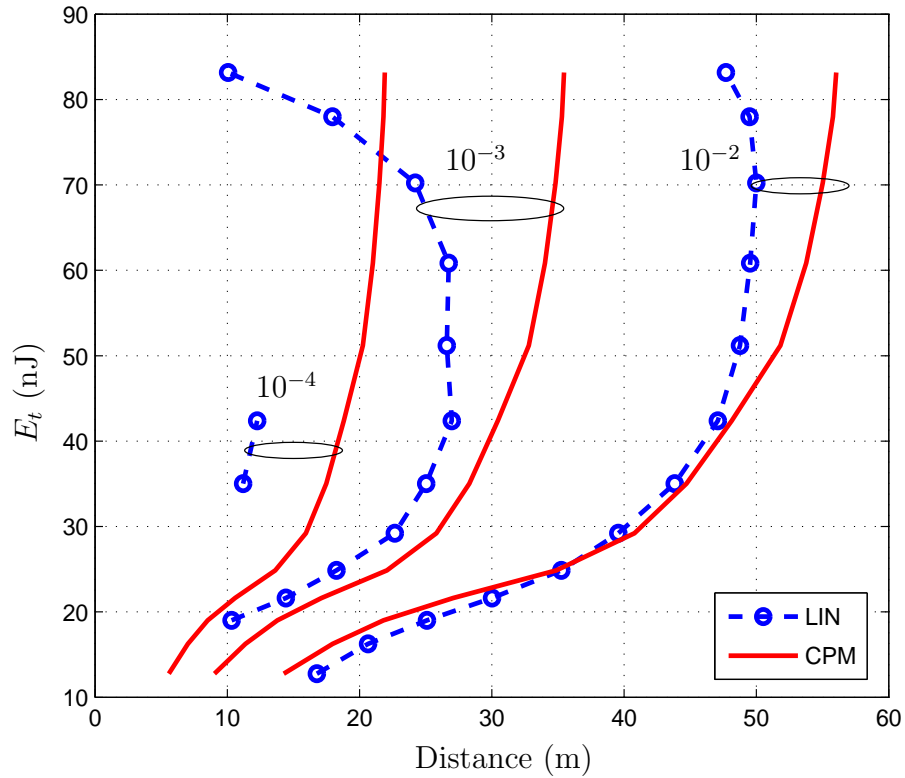


Figure 3.11: Total energy (nJ) per active node, per symbol vs. maximum transmission distance (m) for $N_s = 5$ active nodes and for a distributed ST-LM scheme ('LIN') and a distributed ST-CPM scheme ('CPM'). Results are shown for BERs of 10^{-2} , 10^{-3} , and 10^{-4} . A Class C amplifier [6] is employed.

coherent detection scheme (using only information about the channel and the signature vectors) is unable to correct. In contrast, the performance of the distributed ST-CPM scheme does not deteriorate in the saturation region of either of the power amplifiers.

More specifically, the results for the Class AB power amplifier shown in Figure 3.9 indicate that the CPM based scheme outperforms the distributed ST-LM scheme when the power amplifier is operated at mid to high power levels. In fact, the CPM based scheme increases the range of the distributed ST coding scheme by 1.3 m (2.6% of total range), 10.8 m (15.4%), and 18.5 m (19.7%) for $N_s = 2, 3$, and 5, respectively. When the power amplifier is operated at low power the linear based scheme offers a slight performance

improvement over the CPM based scheme. However, in this power range the CPM based scheme requires minimal additional energy to provide comparable performance, i.e. at most 6.4 nJ, 2.0 nJ, and 0.4 nJ per symbol for $N_s = 2, 3$, and 5 active nodes, respectively.

Next, we consider the performance of the Class C power amplifier shown in Figure 3.10. Using the Class C power amplifier, the CPM based scheme extends the range of the distributed ST coding scheme by 0.9 m (4.8% of total range), 4.9 m (18.5%), and 8.4 m (23.7%) for $N_s = 2, 3$, and 5, respectively. In this case, the distributed ST-LM scheme outperforms the CPM based scheme at low power only for $N_s = 2$ and not at all for $N_s = 3$ and 5. This single performance gap can be closed by an addition of 10.0 nJ per symbol to the CPM based scheme. As a final note on Figs. 3.9 and 3.10, we observe that while recognizing that the Class AB and Class C amplifiers used in this work have been designed for different purposes, the larger transmission distances made possible by selecting the Class AB power amplifier come at the cost of a large increase in energy consumption.

Finally, we consider the performance of the ST-LM and ST-CPM schemes for different BERs employing the Class C amplifier and $N_s = 5$ active nodes. Figure 3.11 shows the performance of both schemes for average BERs of 10^{-2} , 10^{-3} , and 10^{-4} . The CPM scheme offers energy savings of 18.8 nJ, 10.0 nJ, and 23.2 nJ per symbol at the maximum operating range of the linear based scheme for BERs of 10^{-2} , 10^{-3} , and 10^{-4} , respectively. In addition, the CPM based scheme increases the range of the distributed ST coding scheme by 6.0 m (10.7% of total range), 8.4 m (23.7%), and 9.6 m (43.8%) for BERs of 10^{-2} , 10^{-3} , and 10^{-4} , respectively.

3.4 Conclusions

In this chapter, we have proposed a distributed ST-CPM code that enables uncoordinated node cooperation in wireless networks together with energy-efficient CPM transmission.

The devised distributed ST-CPM scheme is a combination of the diagonal ST-CPM code proposed in Chapter 2, which is shared by all nodes and signature vectors that are uniquely assigned to nodes. A numerical method for the optimization of signature vectors sets has been developed. Applying optimized signature vectors, the performance of the proposed distributed ST-CPM scheme is close to that achievable with co-located antennas.

Reduced energy consumption is the primary motivation for selecting a CPM based scheme. Therefore, in the second portion of this chapter, we investigated the energy consumption of a distributed ST-LM scheme and the proposed distributed ST-CPM schemes when these schemes employ practical non-linear Class AB and Class C amplifiers. The distributed ST schemes were compared using the total energy (radiated and used in hardware) required to supply a target BER at a maximum transmission distance. For a relay network composed of $N = 30$ possible relay nodes, the comparisons showed that the linear based scheme outperforms the CPM based scheme when the power amplifiers are operated at low power, but that at low power the performance gap can be closed by the addition of a very small amount of energy (0 to 10.0 nJ per symbol for the relay configurations considered here). At high power the CPM based scheme offers significant energy savings, and extended coverage for both types of power amplifiers (from 2.6% to 43.8%). Performance gains were shown to increase with the number of active relay nodes N_s .

The considerable energy savings and extended coverage range provided by the proposed distributed ST-CPM coding make this scheme an excellent candidate for application in *ad-hoc* networks, such as sensor networks.

Chapter 4

Concatenated Coding for Space–Time Coding with Continuous Phase Modulation

Since Shannon published his landmark paper [76] placing an upper limit on channel capacity information and coding theorists have sought to find codes that will approach the Shannon limit. In 1966, Forney proposed concatenating codes together, an idea that produced codes which reduced the bit error rate (BER) exponentially, whilst only increasing the decoding complexity algebraically. The next innovation in the field of concatenated codes was the Turbo code, which used parallel concatenation and an interleaver. The interleaver further reduced error rate by negating the effects of fading over consecutive sequences of data. These systems could employ iterative decoding, which involved the exchange of soft information about the transmitted bits, so that each decoder could improve on the soft bit estimates with each exchange of information. As a result Turbo codes produced practical systems that perform close to the Shannon limit. In [77], Benedetto *et al.* showed that serially concatenated systems could provide performance results equal, and in some cases superior to those achievable with Turbo codes. Serially concatenated codes can sequentially combine coding (as an outer element) and modulation (as an inner element). If the inner encoder is recursive in nature then increasing the length of the interleaver improves the performance of the concatenated code (yielding an interleaver gain).

In this chapter, we investigate a serially concatenated system employing space–time (ST) continuous phase modulation (CPM) as the inner code, and a class of simple block codes called double parity check (DPC) codes [24] as the outer code. We are motivated in this investigation by the recursive nature of CPM that makes it an excellent fit for a serially concatenated decoding scheme, and by the energy efficiency offered by ST–CPM. We have opted to pair ST-CPM with the DPC class of codes because the DPC codes have a low decoding complexity, and have been shown to enable performance approaching capacity when combined with differential phase-shift keying (DPSK). We study the performance of the serially concatenated ST-CPM system using two different channel models. First, we look at the additive white Gaussian noise (AWGN) channel model traditionally used to study the performance of concatenated codes. Then, in order to further motivate of the selection of ST–CPM as the inner encoding element we study the performance of the concatenated scheme over the quasi-static fading channel (QSFC).

Serially concatenated systems that are built upon single antenna CPM have been investigated by a number of research groups, for example [7], [78] and [79]. In most instances these systems employ a convolutional code as the inner code together with a fairly simple CPM scheme for the outer code. Additionally, serially concatenated ST–CPM systems have received some study. Zhang and Fitz [8] proposed an adaptive soft-output demodulator for ST coded CPM that performed joint channel estimation and data detection. They examined the performance of this demodulator in an interleaved ST–CPM system to evaluate the impact of iterative decoding on channel estimation. Their iterative system consisted of a convolutional outer code and a CPM delay diversity scheme for the inner code. Subsequently, Bokolamulla and Aulin [9] designed an optimum symbol-by-symbol iterative detector for serially concatenated ST–CPM. Their system employs previously designed full rank ST–CPM codes and uses a frequency offset to ensure orthogonality. The

frequency offsets introduce bandwidth expansion and are the result of an exhaustive search possible only for fast fading channels. Furthermore, Gabrowska *et al.* [23] have proposed a serially concatenated ST–CPM code for which the outer code is once again a convolutional code. The code has rate 1, and is designed such that the N_T encoded sequences at the output of the convolutional encoder are the sequences that are modulated and transmitted over each of the N_T transmit antenna. Orthogonality is ensured by designing the N_T encoded and interleaved signals to be independent by employing a Gram–Schmidt linear decomposition of the CPM waveforms. Using this technique the complexity of the receiver is increased because the CPM waveform is approximated by $L(M-1)+1$ linear waveforms.

In this chapter, we investigate serially concatenated ST–CPM codes that maintain the constant-envelope properties that are at the heart of the energy savings offered by CPM. We will employ EXIT charts to pair CPM with a class of parity check block codes called Double Parity Check (DPC) codes, which were originally designed for use with differential-phase shift keying (DPSK) [24]. The DPC class of codes are an excellent companion code for ST–CPM as they have a low computational cost (minimizing overall energy consumption) and yet provide performance that is close to capacity.

4.1 Concatenated Coded Transmission System

In this section, we briefly overview the structure and operation of a concatenated code. A block diagram of the serial concatenated encoder employed in this chapter is shown in Figure 4.1. The outer DPC encoder receives at its input the binary bits \mathbf{u} . These bits are processed by the outer DPC encoder into the bit sequence \mathbf{c} . The encoded bits \mathbf{c} are input to an interleaver and are output as the bit sequence \mathbf{c}_{int} . The interleaver bits are input to the ST–CPM inner encoder, which converts the bit sequence to the symbol sequence \mathbf{a} and outputs the CPM waveform $\mathbf{S}(t, \mathbf{a})$ [see Section 2.30 for details]. As in Section 2.30,

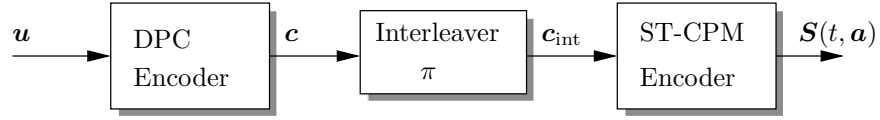


Figure 4.1: Block diagram of a serially concatenated transmission system.

we assume that the ST-CPM system has N_T transmit antennas and N_R receive antennas.

A block diagram of the iterative decoder is shown in Figure 4.2. The ST-CPM inner decoder has two inputs: the received signal $\mathbf{r}(t)$, and the *a priori* information generated by the outer DPC decoder. The received signal is given by Eq. (2.2), which is repeated here for clarity,

$$\mathbf{r}(t) = \mathbf{G}(t)\mathbf{S}(t, \mathbf{a}) + \mathbf{n}(t), \quad 0 \leq t < N_T N_f T \quad (4.1)$$

assuming the QSFC outlined in Section 2.1. The noise term $\mathbf{n}(t)$ is a vector consisting of N_R independent zero mean AWGN processes with power spectral density \mathcal{N}_0 . The filtered received signal for D receive filters is given by

$$\mathbf{R}[n] = \begin{bmatrix} r_1^{(1)}[n] & r_1^{(2)}[n] & \cdots & r_1^{(D)}[n] \\ r_2^{(1)}[n] & r_2^{(2)}[n] & \cdots & r_2^{(D)}[n] \\ \vdots & & & \vdots \\ r_{N_R}^{(1)}[n] & r_{N_R}^{(2)}[n] & \cdots & r_{N_R}^{(D)}[n] \end{bmatrix}, \quad (4.2)$$

where the elements $r_{n_r}^{(d)}[n]$ of $\mathbf{R}[n]$ are given in (2.31).

During the first iteration the inner decoder only uses the received signal because no *a priori* information is available from the outer decoder. For every other iteration the *a priori* bit information received from the outer encoder is converted into *a priori* symbol information and used in conjunction with the received signal to generate the *a posteriori* probability (APP) of the bit sequence \mathbf{c}_{int} . Before the APPs are passed to the de-interleaver and then to the outer decoder, any *a priori* information used to generate these probabilities must be removed. If the *a priori* information generated by the outer encoder is included

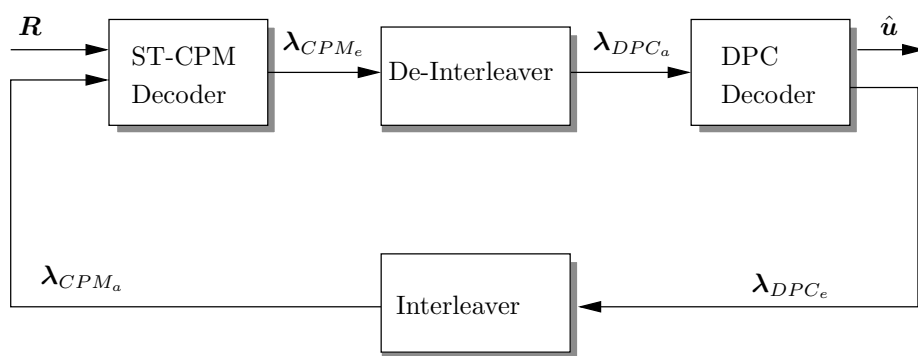


Figure 4.2: Block diagram of a serially concatenated transmission system.

in the bit probability information supplied to the outer encoder incorrect bit decisions may be reinforced causing a complete failure of the iterative decoder. Once the *a priori* information has been removed from the APP, the resulting *extrinsic* information, λ_{CPM_e} is passed to the de-interleaver. The de-interleaved extrinsic information becomes the *a priori* input to the outer decoder, λ_{DPC_a} . The outer decoder processes the *a priori* sequence λ_{DPC_a} and outputs the extrinsic bit sequence λ_{DPC_e} . The extrinsic information sequence λ_{DPC_e} can either be re-interleaved and used in another iteration cycle, or combined with the *a priori* information sequence λ_{CPM_e} to produce hard decisions on the transmitted bit sequence.

Having outlined the structure and operation of the serially concatenated ST–CPM system, we now overview how the information is exchanged and some mathematical tools for generating this information. A compact means of communicating both the decisions and the reliability of the decisions is the log likelihood ratio (LLR) given by

$$L(u) \triangleq \log \left(\frac{p(u = 0 | (inputs))}{p(u = 1 | (inputs))} \right), \quad (4.3)$$

where *inputs* refers to all inputs to the inner or outer decoder. Following the methods used in [24] we treat the LLR generated by one decoder as *a priori* information at the input

of the subsequent decoder. In the case of the ST–CPM decoder the LLR information is treated as *a priori* information about the encoded symbol and is used in conjunction with the information received over the channel (see Section 4.1.3 for more details). In the case of the DPC decoder the LLR information is the only input (see 4.1.1 for more details).

Processing the LLR values requires the decoding units to generate the LLR of the modulo-2 addition of two information bits. This operation is called the boxplus and is denoted by the \boxplus notation. Using the $u[i]$ to denote a generic information bit, the probability of the modulo-2 addition of two information bits is given by

$$p(u[i] \oplus u[k] = 0) = p(u[i] = 1)p(u[k] = 1) + (1 - p(u[i] = 1))(1 - p(u[k] = 1)) \quad (4.4)$$

where we can calculate $p(u[i] = 1)$ from (4.3) as $p(u[i] = 1) = \frac{e^{L(u[i])}}{(1+e^{L(u[i])})}$. Using the above the boxplus operation is defined by

$$\begin{aligned} L(u[i]) \boxplus L(u[k]) &\triangleq L(u[i] \oplus u[k]) \\ &= \log \left(\frac{1 + e^{L(u[i]) + L(u[k])}}{e^{L(u[i])} + e^{L(u[k])}} \right), \end{aligned} \quad (4.5)$$

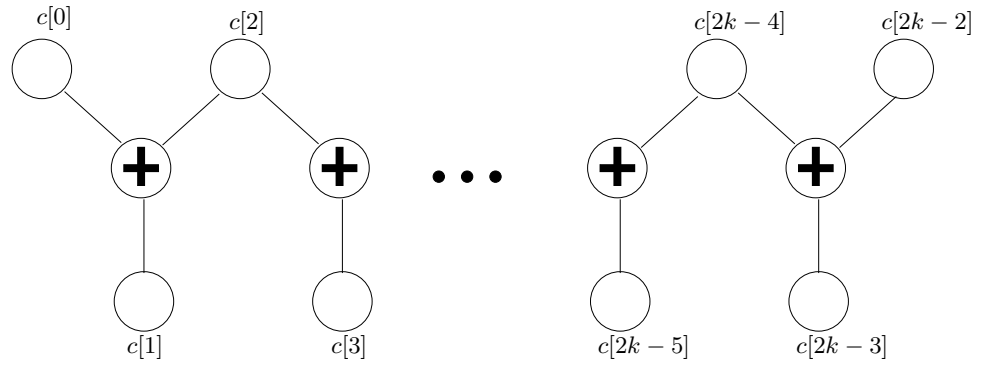
where the following boxplus operations yield

$$L(u[i]) \boxplus \infty = L(u[i]), \quad (4.6)$$

$$L(u[i]) \boxplus -\infty = -L(u[i]), \quad (4.7)$$

$$L(u[i]) \boxplus 0 = 0. \quad (4.8)$$

To minimize the complexity of the decoding algorithm and to preserve the integrity of the


 Figure 4.3: The structure of the DPC I rate $k/(2k - 1)$ code.

LLR information we define [77]

$$\begin{aligned} \max_{i=1, \dots, K}^* (L(u[i])) &= \log \left(\sum_{i=1}^K e^{L(u[i])} \right) \\ &= \max_{i=1, \dots, K} (L(u[i])) + \delta(L(u[1]), \dots, L(u[K])) \end{aligned} \quad (4.9)$$

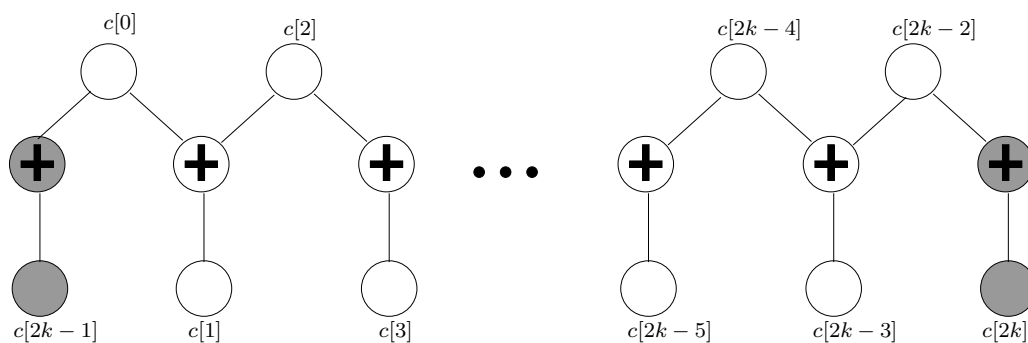
for the addition of LLR information, where $\delta(L(u[1]), \dots, L(u[K]))$ is a correction term added to the max operation that is recursively calculated, i.e.,

$$\delta(a, b) = \log(1 + e^{-|a-b|}), \quad (4.10)$$

$$\delta(a, b, c) = \log(1 + e^{-|\delta(a,b)-c|}). \quad (4.11)$$

4.1.1 Double Parity-Check (DPC) Codes

DPC codes were introduced by Mitra and Lampe [24] for use in a serially concatenated system with multi-level DPSK. The capacity approaching performance of DPC codes with DPSK, combined with their low decoding complexity make these codes an excellent candidate for concatenated with CPM and ST–CPM. In this section, for ease of reference we briefly overview the structure of these DPC codes. The outer encoder shown in Figure 4.2 accepts N_b bits at its input, which are denoted as $[u[0], \dots, u[N_b - 1]]$, and outputs


 Figure 4.4: The structure of the DPC II rate $k/(2k+1)$ code.

N_{DPC} bits at its output, which are denoted as $[c[0], \dots, c[N_{\text{DPC}} - 1]]$. The DPC code is a block code that processes the frame of input bits in blocks, with a code rate of k/n (i.e. $N_{\text{DPC}} = (n/k)N_b$). The DPC codes proposed in [24] can be separated into two classes, denoted as DPC I and DPC II. The DPC I class of codes has rate $r = k/n = k/(2k-1)$. As the length k of the block of input bits is increased the rate of the DPC I class of codes approaches $1/2$. Mathematically, the code bits are given by

$$\begin{aligned}
 c[2i] &= u[i], \\
 c[2i+1] &= u[2i] \oplus u[2i+2].
 \end{aligned} \tag{4.12}$$

The Tanner graph for the DPC I code is shown in Figure 4.3, where the even-indexed code bits ($c[0], c[2], \dots, c[2k-2]$) represent the data bits input to the encoder, and the odd-indexed code bits ($c[1], c[3], \dots, c[2k-3]$) represent the parity bits generated by the modulo-2 addition of the adjacent two input data bits. The minimum Hamming distance of the DPC I class of codes is $d_{\min} = 2$ because the data bits that begin and terminate the block of data that is input to the DPC encoder only affect the value of one parity bit each (in contrast to all of the other input data bits that affect the value of two parity bits). The low weight errors that result from a small minimum Hamming distance cause the onset of an error floor at low signal-to-noise ratio (SNR). Therefore, the authors of [24] proposed

a second class of DPC codes (DPC II) with a lower data rate $r = k/(2k + 1)$ but a larger minimum Hamming distance, $d_{\min} = 3$. The minimum Hamming distance of the DPC II code is increased over that of the DPC I code by adding two extra parity bits that have only one input. The Tanner graph for the DPC II group of codes is shown in Figure 4.4, and mathematically the DPC II code is generated by

$$\begin{aligned} c[2i] &= u[i], \\ c[2i + 1] &= u[2i] \oplus u[2i + 2] \\ c[2k - 1] &= u[0] = c[0], \\ c[2k] &= u[k] = c[2k - 2]. \end{aligned} \tag{4.13}$$

Once again, as the length k of the block of input bits is increased the rate of the DPC II class of codes approaches $1/2$.

Soft Decoding of DPC Codes

The Tanner graphs shown in Figures 4.3 and 4.4 confirm that both codes are cycle free. Therefore, message passing decoding is optimum for both codes. Message passing decoding for the DPC codes is accomplished using a conventional forward/backward (FB) algorithm with the following forward and backward recursion metrics

$$f[i] = (f[i - 1] + \lambda_{\text{DPC}_a}(c[2i - 2])) \boxplus \lambda_{\text{DPC}_a}(c[2i - 1]), \tag{4.14}$$

$$b[i] = (b[i + 1] + \lambda_{\text{DPC}_a}(c[2i + 2])) \boxplus \lambda_{\text{DPC}_a}(c[2i + 1]), \tag{4.15}$$

where $\lambda_{\text{DPC}_a}(c[i])$ is the *a priori* information about bit $c[i]$ that is passed to the FB algorithm from the ST–CPM BCJR decoder (described in 4.1.3) in form of a log-likelihood ratio (LLR). A Tanner graph showing the generation of the forward and backward re-

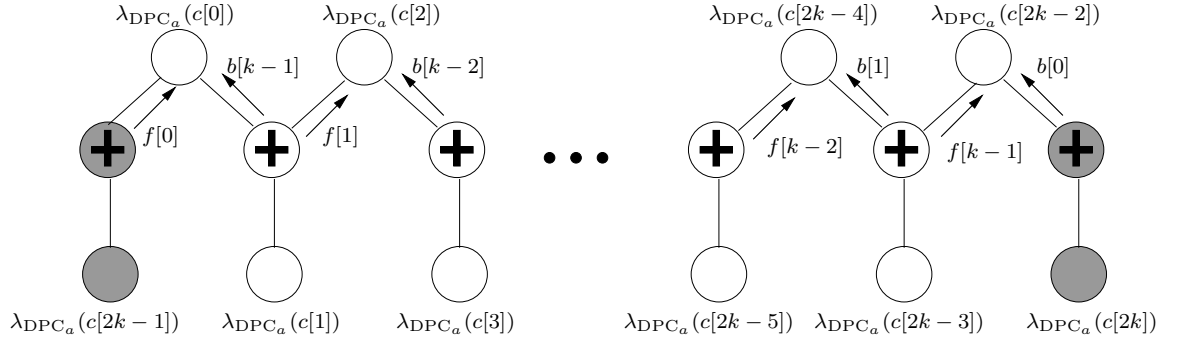


Figure 4.5: Generation of the forward and backward recursion metrics ($f[i]$ and $b[i]$) for DPC I and DPC II.

cursion metrics is given in Figure 4.5. The initial and final values of the forward and backward recursion metrics are $f[0] = 0$, and $b[k-1] = 0$, respectively, for DPC I, and $f[0] = \lambda_{\text{DPC}_a}(c[2k-1])$, and $b[k-1] = \lambda_{\text{DPC}_a}(c[2k])$, respectively, for DPC II. The FB algorithm outputs the extrinsic *a posteriori* probabilities of the data bits

$$\lambda_{\text{DPC}_e}(c[2i]) = f[i] + b[i], \quad (4.16)$$

and of the parity bits

$$\lambda_{\text{DPC}_e}(c[2i+1]) = (f[i] + \lambda_{\text{DPC}_a}(c[2i-1])) \boxplus (b[i] + \lambda_{\text{DPC}_a}(c[2i-2])), \quad (4.17)$$

The *a posteriori* probabilities for the two additional parity bits required for the DPC II code are generated by

$$\lambda_{\text{DPC}_e}(c[2k-1]) = \lambda_{\text{DPC}_a}(c[0]) + \lambda_{\text{DPC}_e}(c[0]) - \lambda_{\text{DPC}_a}(c[2k-1]) \quad (4.18)$$

$$\lambda_{\text{DPC}_e}(c[2k]) = \lambda_{\text{DPC}_a}(c[2k-3]) + \lambda_{\text{DPC}_e}(c[2k-3]) - \lambda_{\text{DPC}_a}(c[2k]) \quad (4.19)$$

After the bit LLRs have been generated they are passed through the interleaver and input to the ST-CPM decoder, and used to generate symbol LLRs that can be used in the

	00	01	10	11
Ungerboeck (UL)	−3	−1	+1	+3
Gray1 (GL1)	−3	−1	+3	+1
Gray2 (GL2)	−3	+1	+3	−1

Table 4.1: Symbol labeling for $M = 4$.

ST-CPM decoder.

4.1.2 ST-CPM

For the inner encoder, we adopt the diagonal block-based ST-CPM scheme detailed in Chapter 2. As shown in Figure 4.2 the ST-CPM encoder receives the bits $[c_{\text{int}}[0], \dots, c_{\text{int}}[N_{\text{DPC}} - 1]]$ and outputs the symbols $[a_{n_t}[0], \dots, a_{n_t}[N_f - 1]]$ on $1 \leq n_t \leq N_T$ antenna. However, the bit-to-symbol mappings that were optimal for the non-iterative system used in Chapter 2 are not optimal for the iterative decoding system that we consider here. In fact, even in the case of one transmit antenna the bit-to-symbol mapping has significant influence on the performance of the iterative system, (we will examine in detail the role of symbol labeling in Section 4.2). For $M = 4$, we can generate the mutual information transfer characteristics for all 24 possible labelings and determine those that are unique. For the CPM schemes used as examples in this work, three distinct labelings were identifiable: traditional Ungerboeck (or natural) labeling (UL), and two types of Gray labeling ((GL1) and (GL2)). These mappings are given in Table 4.1.

For $M = 8$, rather than re-examine the $8!$ different mapping possibilities, we will study the performance of several mappings that have been shown to have superior performance in iterative coding schemes employing PSK modulation. In particular, six different labelings are considered. These labelings include Ungerboeck labeling (UL), Gray labeling (GL), Antigray labeling (AGL), Semi-set partitioning labeling (SSPL) [80], Howard and Schlegel

	000	001	010	011	100	101	110	111
Ungerboeck (UL)	−7	−5	−3	−1	+1	+3	+5	+7
Gray (GL)	−7	−5	−1	+7	+3	+1	+5	−3
Antigray (AGL)	−7	+7	−5	+5	+3	−3	+1	−1
Semi-Set Partitioning (SSPL)	−7	+3	−3	+7	+1	−5	+5	−1
Howard and Schlegel (HSL)	−7	+7	−5	+1	−3	−1	+5	+3
Nuriyev and Anastosopoulos (NAL)	−7	+7	−1	+1	+3	−3	+5	−5

Table 4.2: Symbol labeling for $M = 8$.

labeling (HSL) [81], and Nuriyev and Anastosopoulos labeling (NAL) [82]. These mappings are given in Table 4.2. In addition, when we consider transmission over multiple transmit antenna we will consider only the repetition code, i.e. the same symbol labeling applied to antennas $n_t = 1, \dots, N_T$. Selecting the repetition code allows a simple EXIT chart analysis of the different symbol labelings, and allows for a simple lower bounding of the outage probability of the scheme when the QSFC is considered. In addition, we will show that when the repetition code is used with optimal symbol labeling over the QSFC the resulting scheme yields performance near the lower bound on outage probability.

4.1.3 Soft Decoding of ST–CPM

The object of the soft decoding algorithm employed by the ST–CPM decoder is to use both the received signal and the *a priori* information provided by the DPC decoder to generate the *a posteriori* probability $\Pr\{a_1[i] = m | \mathbf{R}\}$, where $\mathbf{R} = [R[0], \dots, R[N_f]]$. Note that, the DBST-CPM scheme given in Chapter 2 fixes the symbols transmitted over antennas $n_t = 2 \dots N_T$ with respect to the symbols transmitted over antenna $n_t = 1$ and the ST-CPM code \mathcal{C} , therefore it sufficient to refer to the symbols transmitted over antenna $n_t = 1$. As shown in Figure 4.2, these APP symbol probabilities can then be converted into APP bit probabilities, de-interleaved and then recycled as the input to the outer (DPC) decoder. The BCJR algorithm [83] is the optimal trellis based soft-output algorithm for

estimating the probabilities $\Pr\{a_1[i] = m|\mathbf{r}\}$. In this case the BCJR algorithm operates on the ST–CPM trellis discussed in Section 2.3.3.

The iterative decoder employs LLRs, therefore it suffices to calculate the joint probability of the transmitted symbol $a_1[i]$ and the received signal frame \mathbf{R} , given by

$$p(a_1[i] = m, \mathbf{R}) = \sum_{s_i} \sum_{s_{i-1}} \alpha_{i-1}(s_{i-1}) \gamma_m(s_i, s_{i-1}) \beta_i(s_i) \quad (4.20)$$

where $\alpha_{i-1}(s_{i-1})$ is denoted as the forward metric, $\beta_i(s_i)$ is denoted as the backward metric, and $\gamma_m(s_i, s_{i-1}) = p(\mathbf{R}[i], s_i, a_1[i] = m | s_{i-1})$, $m \in \{-M + 1, -M + 3, \dots, M - 1\}$ is denoted as the branch transition metric. The branch transition metric is the probability of transitioning from state s_{i-1} to state s_i when the symbol transmitted is $a_1[i] = m$ can also be expressed as

$$\gamma_m(s_i, s_{i-1}) = p(\mathbf{R}[i] | a[i] = m, s_i, s_{i-1}) P(s_i | s_{i-1}) \quad (4.21)$$

where $p(\mathbf{R}[i] | a[i] = m, s_i, s_{i-1})$ is the conditional probability of the received signal $\mathbf{R}[i]$ given that the symbol $a[i] = m$ was transmitted starting in state s_i and finishing in state s_{i-1} , and $P(s_i | s_{i-1}) = \lambda_{\text{CPM}_a}(a_1[i] = m)$ is the *a priori* probability of the transition from state s_{i-1} to state s_i , or equivalently the *a priori* probability of the symbol $a[i] = m$. The forward metric, α_i , which is the probability of transitioning from the beginning of the frame to the state s_i , is given by

$$\begin{aligned} \alpha_i(s_i) &= p(s_i, \mathbf{R}_0^i), \\ &= \sum_{s_{i-1}} \sum_m \gamma_m(s_i, s_{i-1}) \alpha_{i-1}(s_{i-1}), \end{aligned} \quad (4.22)$$

where \mathbf{R}_0^{i-1} denotes the vector $[\mathbf{R}[0] \cdots \mathbf{R}[i - 1]]$. Similarly, the backward metric, $\beta_i(s_i)$,

which is the probability of transitioning from the end of the frame to the state s_i , is given by

$$\begin{aligned}\beta_i(s_i) &= p(\mathbf{R}_i^{N_f-1} | s_i), \\ &= \sum_{s_{i+1}} \sum_m \gamma_m(s_{i+1} s_i) \beta_{i+1}(s_{i+1}).\end{aligned}\quad (4.23)$$

The initialization of α and β is dependent on the initial and final states of the ST–CPM trellis. The termination state of the trellis is unknown and therefore the values of $\beta_i(s_i)$ corresponding to the final state of the trellis ($\beta_{N_f-1}(s_{N_f-1})$) are uniformly initialized. In contrast, the initial state of the trellis is assumed to be known and the probability of this state is set to one, while the probability of the other states ($\alpha_0(s_0)$) is set to zero.

In Section 2.3.3, we defined the branch metric for the Viterbi decoder as the cross-correlation of the received signal and the filtered signal element $\rho_{n_t}(\mathbf{d}[i])$, where $\mathbf{d}[i]$ is an ‘address vector’ composed of the L most recent M -ary data symbols $a[i]$, and the N_T p -ary phase states that contain the phase information for each of the n_t antenna that has been accumulated over symbols transmitted from the beginning of the frame to the $L - 1$ most recent symbol. For clarity we will restate the address vector $\mathbf{d}[i]$ here

$$\mathbf{d}[i] \triangleq [\Upsilon_1[i - L], \dots, \Upsilon_{N_T}[i - L], \mathbf{a}[i - L + 1], \dots, \mathbf{a}[i]].\quad (4.24)$$

In order to derive the probability $p(\mathbf{R}[i] | a[i] = m, s_i, s_{i-1})$ we must slightly redefine the expression for the signal element $\rho_{n_t}(t, \mathbf{d}[i])$ filtered by the matched filter bank specified by the vector $\mathbf{h}_D(t)$ (see Eq. (1.20)). The filtered signal elements used by the BCJR algorithm are given by

$$\rho_{n_t}^B(\mathbf{d}[i]) = \int_0^T \rho_{n_t}(t, \mathbf{d}[i]) \mathbf{h}_D^*(t) dt,\quad (4.25)$$

where $\rho_{n_t}(t, \mathbf{d}[i])$ is the signal element transmitted over antenna n_t in the period $iT + (n_t -$

1) $N_f T \leq t < (i + 1)T + (n_t - 1)N_f T, 0 < i < N_f$ corresponding to the address vector $\mathbf{d}[i]$.

If we assume coherent detection the probability $p(\mathbf{r}|a_1[i] = m, s_i, s_{i-1})$ can be written as

$$\begin{aligned}
 p(\mathbf{R}|a_1[i] = m, s_i, s_{i-1}) &= \\
 &= \frac{1}{(\pi\sigma^2)^{N_T}} \prod_{n_t=1}^{N_T} \prod_{n_r=1}^{N_R} \exp \left((\mathbf{r}_{n_r}[i + (n_t - 1)N_f] g_{n_r n_t}^*[i + (n_t - 1)N_f] - \boldsymbol{\rho}_{n_t}^B(\mathbf{d}[i]))^H C^{-1} \right. \\
 &\quad \left. (\mathbf{r}_{n_r}[i + (n_t - 1)N_f] g_{n_t n_r}^*[i + (n_t - 1)N_f] - \boldsymbol{\rho}_{n_t}^B(\mathbf{d}[i])) \right). \tag{4.26}
 \end{aligned}$$

where $\mathbf{r}_{n_r}[i]$ denotes the filtered signal received on antenna n_r [see Section 2.3.3].

The BCJR algorithm as it has been presented is computationally complex and can become unstable when small probability values are generated. In logarithmic form the BCJR algorithm is computationally less complex and numerically stable. The branch transition metric in logarithmic form can be written as

$$\begin{aligned}
 \Gamma_m(s_i, s_{i-1}) &= \log(\gamma_m(s_i, s_{i-1})), \\
 &= \sum_{n_t=1}^{N_T} \sum_{n_r=1}^{N_R} \left((\mathbf{r}_{n_r}[i + (n_t - 1)N_f] g_{n_r n_t}^*[i + (n_t - 1)N_f] - \boldsymbol{\rho}_{n_t}^B(\mathbf{d}[i]))^H C^{-1} \right. \\
 &\quad \left. (\mathbf{r}_{n_r}[i + (n_t - 1)N_f] g_{n_t n_r}^*[i + (n_t - 1)N_f] - \boldsymbol{\rho}_{n_t}^B(\mathbf{d}[i])) \right) \\
 &\quad + \lambda_{\text{CPM}_a}(a_1[i] = m) + K, \tag{4.27}
 \end{aligned}$$

where $\lambda_{\text{CPM}_a}(a_1[i])$ are the *a priori* symbol LLRs that are generated from the bit LLRs $\boldsymbol{\lambda}_{\text{DPC}_e}$ that are produced by the DPC decoder. Thus, if $\Omega_{n_t}[m], 1 \leq m \leq M$ is the data mapping for input symbol m on antenna n_t then the *a priori* information on symbol $a_1[i]$ is given by

$$\lambda_{\text{CPM}_a}(a_1[i] = m) = \max_{j: a_1^j[i]=1}^* (\lambda_{\text{DPC}_e}(\Omega_1[c^{\text{int}}[i \log_2 M + j]])) \quad 0 \leq i < N_f, \tag{4.28}$$

Note that we need only to generate extrinsic information for $n_t = 1$ because the probability of $a_{n_t}[i] = \Omega_{n_t}[c^{\text{int}}[i \log_2 M + j]]$ is independent of the antenna and of the data mapping.

Similarly, we can write the forward and backward metrics in logarithmic form

$$\begin{aligned} A_i(s_i) &= \log(\alpha_i(s_i)) = \log\left(\sum_{s_{i-1}} \sum_m \exp(\log(\gamma_m(s_i, s_{i-1}))) + \log(\alpha_{i-1}(s_{i-1}))\right), \\ &= \max_{s_{i-1}, m}^* (\Gamma_m(s_i, s_{i-1}) + A_{i-1}(s_{i-1})), \end{aligned} \quad (4.29)$$

and

$$\begin{aligned} B_i(s_i) &= \log(\beta_i(s_i)) = \log\left(\sum_{s_{i+1}} \sum_m \exp(\log(\gamma_m(s_{i+1}, s_i))) + \log(\beta_{i+1}(s_{i+1}))\right), \\ &= \max_{s_{i+1}, m}^* (\Gamma_m(s_{i+1}, s_i) + B_{i+1}(s_{i+1})). \end{aligned} \quad (4.30)$$

Using the above equations we can write the APP probability of a symbol as

$$APP(a_1[i] = m) = \max_{s_i, s_{i-1}}^* [A_{i-1}(s_{i-1}) + \Gamma_m(s_i, s_{i-1}) + B_i(s_i)]. \quad (4.31)$$

If we denote the bits that comprise the symbol $a_1[i]$ as $[a_1^1[i], a_1^2[i], \dots, a_1^{\log_2 M}[i]]$, then we can write the LLR of bit $a_1^j[i]$ as

$$L(a_1^j[i]) = \sum_{a_1[i]: a_1^j[i]=0} APP(a[i] = m) - \sum_{a_1[i]: a_1^j[i]=1} APP(a[i] = m), \quad 0 < j \leq \log_2 M. \quad (4.32)$$

Before the LLR given above is passed through the de-interleaver and then to the DPC decoder the *a priori* information supplied to the ST–CPM decoder must be removed to leave only extrinsic information. The extrinsic information about the DPC coded, interleaved

bit $a_1^j[i] = c^{\text{int}}[i \log_2 M + j]$ generated by the BCJR algorithm for ST–CPM is

$$\lambda_{\text{CPM}_e}(c^{\text{int}}[i \log_2 M + j]) = L(a_1^j[i]) - \lambda_{\text{CPM}_a}(c^{\text{int}}[i \log_2 M + j]), \quad 0 \leq i < N_f, 0 < j \leq \log_2 M. \quad (4.33)$$

4.2 Analysis and Design of Concatenated ST–CPM Using EXIT Charts

In general, the performance of an iterative decoding scheme can be characterized by a BER curve with three distinct regions. At low SNR the BER shows minimal improvement with increasing SNR. At some threshold SNR the BER drops distinctly, in what is often called the waterfall region. Finally, as SNR is increased beyond the threshold SNR the iterative decoding scheme will at some point encounter an error floor. The threshold SNR at which the scheme enters the waterfall region, and the SNR at which the scheme encounters the error floor are both parameters that are dependent upon the design of the inner and outer codes.

Several methods have been proposed to predict the performance of an iterative decoding scheme, and in particular the SNR at the onset of the waterfall region. One of the proposed methods is density evolution [84]. Density evolution involves calculation of the probability density functions (pdfs) of the information that is exchanged between the decoding units. By tracking the evolution of these pdfs and using a thresholding mechanism density evolution is able to predict the SNR at which the waterfall region begins. Several simpler methods have been proposed that are also very accurate in predicting the onset of the waterfall region. One of these methods is the EXIT chart [85] which focuses on the exchange of mutual information (i.e. a single parameter of the pdf instead of the

entire pdf) between the inner and outer decoding units. Using the EXIT chart approach allows for analysis of the individual component decoders, rather than requiring a study of the entire iterative decoder. Once the relationship between the mutual information at the input and output of the component decoders has been established, the performance of the overall operation of the iterative decoder can be examined; the mutual information at the output of the ST–CPM decoder is the mutual information at the input of the DPC decoder and, similarly, the mutual information at the output of the DPC decoder is the mutual information at the input of the ST–CPM decoder. Note that an ideal interleaver (which ensures that consecutive bits are independent) has no impact on the exchange of mutual information.

In the following, we overview the method used to generate the mutual information transfer characteristics of the inner and outer codes. Next, we create a sample EXIT chart for the AWGN channel and explain how the EXIT chart can be used to predict the performance of the concatenated code. We conclude the section, by detailing how an EXIT chart can be generated for ST–CPM when a QSFC is considered.

4.2.1 Generation of the Mutual Information Transfer Characteristics

The first step in the generation of the EXIT chart is to establish the relationship between the mutual information at the input and output of the component decoders. Here, we will briefly overview the mathematical background of the EXIT chart [85]. We will assume a generic decoder that receives a signal r , that is generated by an input symbol u plus a Gaussian random variable n with zero mean and variance σ_n^2 (i.e. $r = u + n$). This system corresponds to transmitting the concatenated coded signal over an AWGN channel. The

LLR generated by this signal is given by

$$L[r] = \log \left(\frac{r|u=0}{r|u=1} \right) = \frac{2}{\sigma_n^2}(u+n). \quad (4.34)$$

In [85], ten Brink noted that simulation results indicate that the probability density functions of the extrinsic information generated by the decoding units that make up the iterative decoder tend towards Gaussian-like distributions as the number of iteration is increased. This means that the *a priori* input to a decoding unit has a Gaussian-like distribution. In addition, when the interleaver length is large the *a priori* LLR information is uncorrelated with information received over the channel. Therefore, the *a priori* LLR information at the input of the inner decoder is modelled as a Gaussian variable

$$\lambda_a = \mu_a u + n_a, \quad (4.35)$$

where n_a is a Gaussian random variable with zero mean, and variance σ_a^2 , and $\mu_a = \sigma_a^2$. The conditional probability density of this *a priori* LLR information is given by

$$p_{\lambda_a}(\xi|U=u) = \frac{\exp\left(-\frac{(\xi - \frac{\sigma_a^2}{2}u)^2}{2\sigma_a^2}\right)}{\sqrt{2\pi}\sigma_a}. \quad (4.36)$$

The mutual information between the *a priori* LLR λ_a and the transmitted bits U is given by

$$I_a(\sigma_a) = I(U; \lambda_a) = \frac{1}{2} \sum_{u=-1,+1} \int_{-\infty}^{+\infty} \log_2 \left[\frac{2p_{\lambda_a}(\xi|U=u)}{p_{\lambda_a}(\xi|U=-1) + p_{\lambda_a}(\xi|U=+1)} \right] p_{\lambda_a}(\xi|U=x) d\xi, \quad (4.37)$$

and substituting (4.36) this can be written as

$$I_a(\sigma_a) = 1 - \int_{-\infty}^{+\infty} \frac{\exp\left(-\frac{(\xi - \frac{\sigma_a^2}{2})^2}{2\sigma_a^2}\right)}{\sqrt{2\pi}\sigma_a} \log_2 [1 + \exp(-\xi)] d\xi. \quad (4.38)$$

To simplify future calculations we define

$$J(\sigma) \triangleq I_a(\sigma_a = \sigma), \quad (4.39)$$

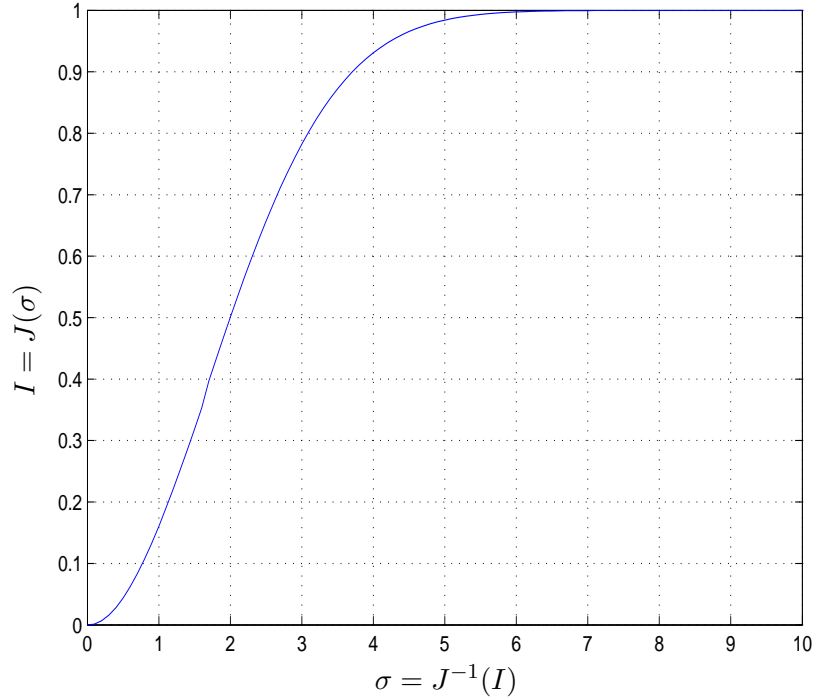
$$\lim_{\rho \rightarrow 0} J(\sigma) = 0, \quad \lim_{\sigma \rightarrow \infty} J(\sigma) = 1, \sigma > 0. \quad (4.40)$$

The expression for mutual information as a function of input noise variance given in (4.39) cannot be expressed in closed form. Therefore, for the purposes of computer simulation we use an approximation furnished by the non-linear least squares Marquardt-Levenberg algorithm [86, 87]. Employing this approximation, evaluation of $J(\sigma)$ is split into two intervals: $0 \leq \sigma \leq \sigma_{tp}$, and $\sigma_{tp} < \sigma < 10$, where $\sigma_{tp} = 1.6363$. The approximation for $J(\sigma)$ is given by

$$J(\sigma) \approx \begin{cases} a_{J,1}\sigma^3 + b_{J,1}\sigma^2 + c_{J,1}\sigma & 0 \leq \sigma \leq \sigma_{tp} \\ 1 - \exp[a_{J,2}\sigma^3 + b_{J,2}\sigma^2 + c_{J,2}\sigma + d_{J,2}] & \sigma_{tp} < \sigma < 10 \\ 1 & \sigma \geq 10 \end{cases} \quad (4.41)$$

where

$$\begin{aligned} a_{J,1} &= -0.0421061, & b_{J,1} &= 0.209252, & c_{J,1} &= -0.00640081, \\ a_{J,2} &= -0.00181491, & b_{J,2} &= -0.142675, & c_{J,2} &= -0.0822054, & d_{J,2} &= 0.0549608. \end{aligned} \quad (4.42)$$


 Figure 4.6: Plot of the $J(\sigma)$ function.

Similarly, the inverse of the function $J(\sigma) = J^{-1}(I)$ is evaluated in two intervals: $0 \leq I \leq I_{tp}$, and $I_{tp} < I < 1$, where $I_{tp} = 0.3646$. The approximation of $J^{-1}(I)$ is given by

$$J^{-1}(I) \approx \begin{cases} a_{\sigma,1}I^2 + b_{\sigma,1}I + c_{\sigma,1}\sqrt{I} & 0 \leq I \leq I_{tp} \\ -a_{\sigma,2} \cdot \log[-b_{\sigma,2}(I - 1)] - c_{\sigma,2}I & I_{tp} < I < 1 \end{cases} \quad (4.43)$$

where

$$\begin{aligned} a_{\sigma,1} &= 1.09542, & b_{\sigma,1} &= 0.214217, & c_{\sigma,1} &= 2.33727, \\ a_{\sigma,2} &= 0.706692, & b_{\sigma,2} &= 0.386013, & c_{\sigma,2} &= -1.75017. \end{aligned} \quad (4.44)$$

The $J(\sigma)$ function is shown in Figure 4.6. Having analyzed the relationship between the variance term σ_a^2 and the *a priori* mutual information, I_a , at the input of a decoder we now consider the relation between the mutual information of the extrinsic information at

the output of the decoder, I_e , and the variance term σ_a^2 . The mutual information of the extrinsic information at the output of the decoder can be written as

$$\begin{aligned} I(\boldsymbol{\lambda}_{\text{CPM}_e}; C_{\text{int}}) &= 1 - \int_{-\infty}^{+\infty} p_{\boldsymbol{\lambda}_{\text{CPM}_e}}(\xi | C_{\text{int}} = 1) \log_2[1 + \exp(-\xi)] d\xi, \\ I(\boldsymbol{\lambda}_{\text{DPC}_e}; C) &= 1 - \int_{-\infty}^{+\infty} p_{\boldsymbol{\lambda}_{\text{DPC}_e}}(\xi | C = 1) \log_2[1 + \exp(-\xi)] d\xi. \end{aligned} \quad (4.45)$$

As described in [85], the probability distributions $p_{\boldsymbol{\lambda}_{\text{CPM}_e}}(\xi | C_{\text{int}} = 1)$ and $p_{\boldsymbol{\lambda}_{\text{DPC}_e}}(\xi | C = 1)$ given in (4.45) are generated by simulation. Mutual information is measured for different values of σ_a^2 , by applying the Gaussian random variable given in (4.35) as the *a priori* input to the decoder. Using the time averages (an arbitrarily close approximation of (4.45)) mutual information is given by

$$\begin{aligned} I_{\text{CPM}_e} &= I(\boldsymbol{\lambda}_{\text{CPM}_e}; C_{\text{int}}) \approx 1 - \frac{1}{N_{\text{DPC}}} \sum_{n=1}^{N_{\text{DPC}}} \log_2(1 + e^{-c_{\text{int}}[n] \boldsymbol{\lambda}_{\text{CPM}_e}(c_{\text{int}}[n])}), \\ I_{\text{DPC}_e} &= I(\boldsymbol{\lambda}_{\text{DPC}_e}; C) \approx 1 - \frac{1}{N_{\text{DPC}}} \sum_{n=1}^{N_{\text{DPC}}} \log_2(1 + e^{-c[n] \boldsymbol{\lambda}_{\text{DPC}_e}(c[n])}), \end{aligned} \quad (4.46)$$

where the approximations are valid when pdfs for the LLR are both symmetric, i.e.,

$$p_{\boldsymbol{\lambda}_{\text{CPM}_e}}(\xi | X = 1) = p_{\boldsymbol{\lambda}_{\text{CPM}_e}}(-\xi | X = 0), \quad p_{\boldsymbol{\lambda}_{\text{DPC}_e}}(\xi | X = 1) = p_{\boldsymbol{\lambda}_{\text{DPC}_e}}(-\xi | X = 0), \quad (4.47)$$

and consistent, i.e.,

$$p_{\boldsymbol{\lambda}_{\text{CPM}_e}}(\xi | X = 1) = p_{\boldsymbol{\lambda}_{\text{CPM}_e}}(-\xi | X = 1) \exp(\xi), \quad p_{\boldsymbol{\lambda}_{\text{DPC}_e}}(\xi | X = 1) = p_{\boldsymbol{\lambda}_{\text{DPC}_e}}(-\xi | X = 1) \exp(\xi). \quad (4.48)$$

Having evaluated $I_e(\sigma_a)$ ($I_e(\sigma_a, E_b/\mathcal{N}_0)$ for the outer decoder), and $I_a(\sigma_a)$ we can determine the extrinsic information transfer function $I_e = T(I_a)$ (or $I_e = T(I_a, E_b/\mathcal{N}_0)$ in the case of the outer decoder).

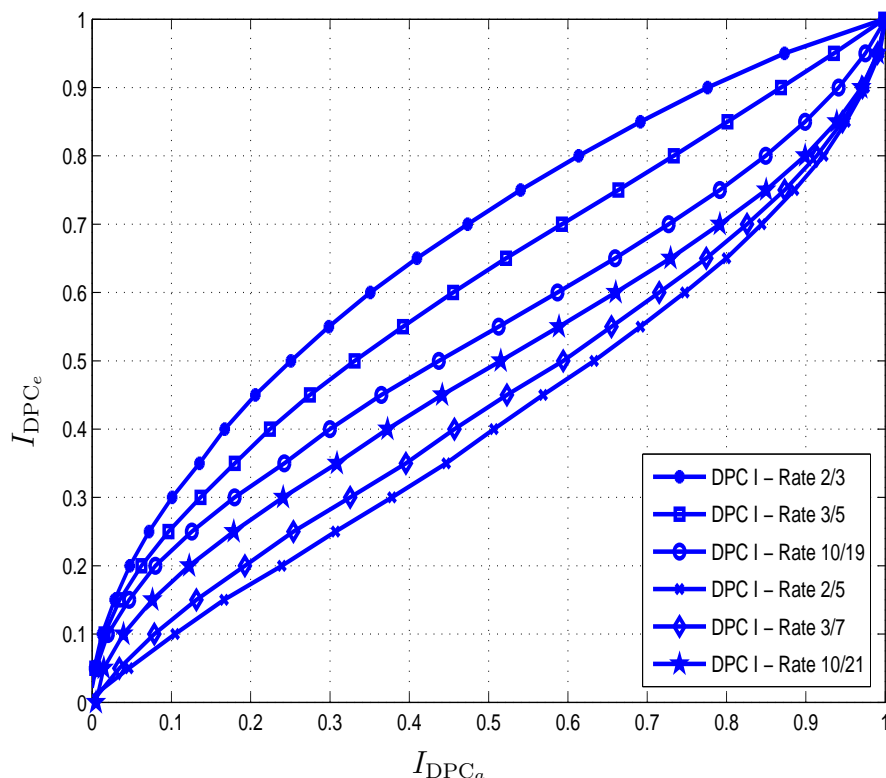


Figure 4.7: Mutual information transfer chart for the DPC codes.

The mutual information transfer chart (I_{DPC_e} vs. I_{DPC_a}) for the DPC I and DPC II classes of codes are shown in Figure 4.7. The figure shows that as the rate of the DPC code is decreased the DPC decoder is able to make better use of the *a priori* mutual information provided to it.

4.2.2 Generation of the EXIT Chart for the AWGN channel

The EXIT chart is generated when the mutual information transfer characteristics of the inner and outer decoders are plotted on the same figure, noting that when the iterative decoder is operating $I_{\text{DPC}_e} = I_{\text{CPM}_a}$ and $I_{\text{CPM}_a} = I_{\text{DPC}_e}$. Figure 4.8, shows an EXIT chart for the ST-CPM code employing $N_T = 1$ transmit antenna, and $M = 4$, $h = 1/4$, a

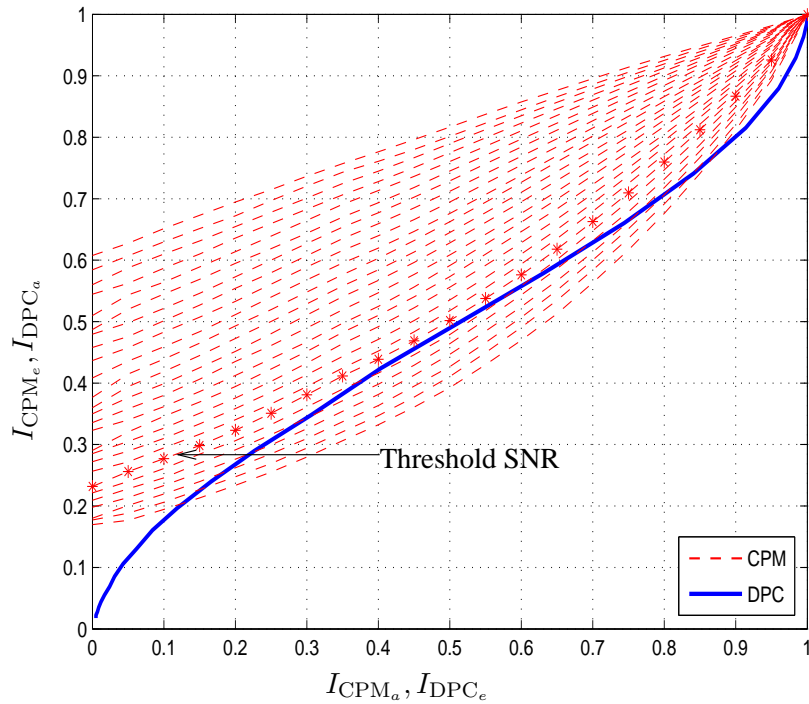


Figure 4.8: EXIT chart depicting the mutual information transfer for the DPC II rate 10/21 code and for the ST–CPM code employing $N_T = 1$ transmit antenna, and $M = 4$, $h = 1/4$, a 1REC pulse with Ungerboeck mapping, and with an SNR (AWGN channel) of ranging from $10 \log_{10}(E_b/N_0) = +0.2$ dB to $+5.2$ dB in increments of 0.2 dB.

1REC pulse, and for the DPC II rate 10/21 code. The extrinsic mutual information at the output of the ST–CPM decoder is dependant not only on the *a priori* mutual information available, but also upon the SNR of the received signal. Figure 4.8 shows results for a SNR, assuming an AWGN channel, ranging from $10 \log_{10}(E_b/N_0) = +0.2$ dB to $+5.2$ dB in increments of 0.2 dB. The SNR at which the mutual information transfer characteristic of the inner decoder no longer intersects the transfer characteristic of the outer decoder is often called the threshold SNR of the scheme. The opening between the inner and outer decoder characteristics is commonly referred to as a ‘tunnel’. The threshold SNR at which the tunnel opens is of interest because it is at this SNR the BER exhibits a sudden and steep decline characteristic to concatenated codes, which is commonly referred to as the

BER ‘waterfall’.

Ideally, the EXIT chart can be used to visualize the exchange of mutual information between the constituent decoders. Figure 4.9 illustrates the decoding trajectory of a typical concatenated system for two different interleaver lengths. The example shown on the right of Figure 4.9 employs a long interleaver (on the order of 10^5 bits [85]). In this example the mutual information exchange proceeds almost exactly as predicted by the EXIT chart. However, due to the shorter interleaver used in the example on the left of Figure 4.9 correlations in the mutual information mean that the gains predicted by the EXIT chart are not realized [85]. In the worst case, a short interleaver will cause the decoding trajectory to terminate before the (1,1) mutual information point is reached and cause an error floor for the scheme. In the best case, the decoding trajectory does reach the (1,1) point, but requires many more iterations than a decoder using a long interleaver.

4.2.3 Generation of the EXIT chart for the Quasi-Static Fading Channel (QSFC)

In this section, we derive an expression for the extrinsic mutual information at the output of the ST–CPM decoder, I_{CPM_e} assuming a QSFC. Note that the extrinsic information at the output of the DPC decoder is not a function of the channel. As previously discussed, we will generate extrinsic mutual information for the ST–CPM under the condition that repetition coding is used on all N_T antenna. Under this condition symbol labeling must still be optimized, however the same labeling is used on all antennas.

Employing maximal ratio combining (MRC) at the receiver (in order to obtain maximum diversity) the instantaneous SNR per bit, γ_b , is given by

$$\gamma_b = \bar{\gamma}_b \sum_{n_r=1}^{N_R} \sum_{n_t=1}^{N_T} |g_{n_r n_t}|^2, \quad (4.49)$$

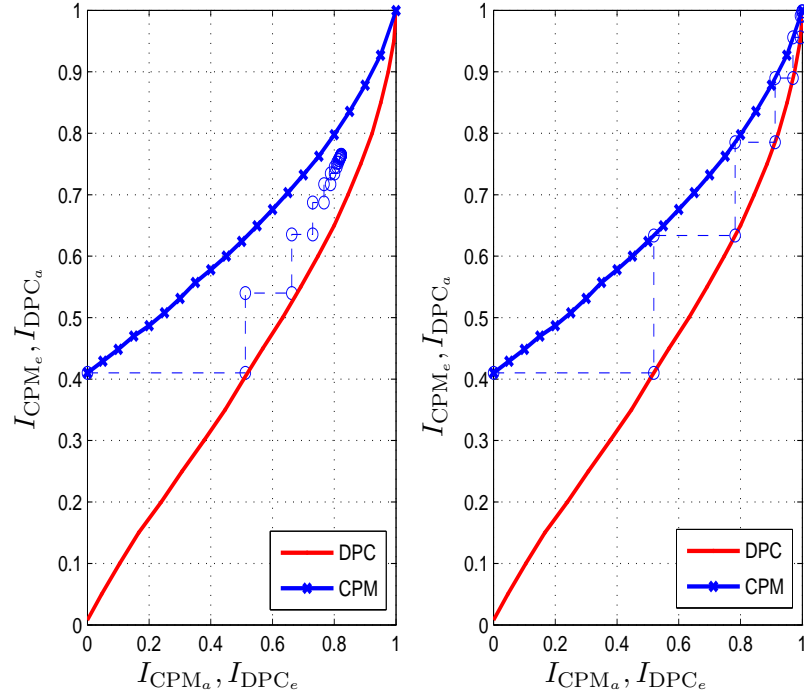


Figure 4.9: Two EXIT charts illustrating the effect of interleaver length on the decoding trajectory. On the left a short interleaver is used, and on the right a long interleaver is used.

where the average SNR $\bar{\gamma}_b$ is given by $\bar{\gamma}_b = E_b/\mathcal{N}_0$. Using this expression for instantaneous SNR we can write an expression for the extrinsic mutual information of a repetition coded ST–CPM signal transmitted over the QSFC as

$$\begin{aligned}
 I_{\text{CPM}_e}^{\text{QSFC}}(\gamma_b) &= \mathcal{E}(I_{\text{CPM}_e}(\bar{\gamma}_b \sum_{n_r=1}^{N_R} \sum_{n_t=1}^{N_T} |g_{n_r n_t}|^2)), \\
 &= \int_{-\infty}^{+\infty} I_{\text{DPC}_e}(\gamma_b) p(\gamma_b) d\gamma_b.
 \end{aligned} \tag{4.50}$$

Under the assumption that the fading on the $N_R N_T$ different channels is statistically independent, the probability density function (pdf) for the sum of $\gamma_b = \sum_{n_r=1}^{N_R} \sum_{n_t=1}^{N_T} \gamma_{b n_r n_t}$ is a chi-squared pdf with $2N_R N_T$ degrees of freedom. Therefore, the expected capacity of

a repetition coded ST–CPM signal is given by

$$I_{\text{CPM}_e}^{\text{QSFC}}(\gamma_b) = \int_{-\infty}^{\infty} I_{\text{CPM}_e}(\gamma_b) \frac{1}{\bar{\gamma}_b^{N_R N_T} (N_R N_T - 1)!} (\gamma_b)^{N_R N_T - 1} e^{-\gamma_b / \bar{\gamma}_b} d\gamma_b. \quad (4.51)$$

4.3 Capacity

The merit of a transmission scheme, such as concatenated coding, is usually proven by comparing the performance of the scheme against some benchmark, such as capacity. Calculating the capacity of a CPM based scheme is not a simple task because of the memory element inherent to CPM. In this section, we first analyze the capacity of ST–CPM transmitted over the AWGN channel, and then look at the capacity of repetition coded ST–CPM transmitted over a QSFC.

4.3.1 AWGN Channel

In order to calculate the capacity of the ST–CPM scheme transmitted over an AWGN channel we adopt the simulation-based information rate computation method proposed in [88] for systems with channel memory. The techniques proposed in [88] are immediately applicable to ST–CPM for which modulation memory takes the place of channel memory. In this section, we assume a single antenna system ($N_T = 1, N_R = 1$). In this case the received signal can be written as $\mathbf{r}[n] = [r^{(1)}[0], \dots, r^{(D)}[N_f - 1]]$, and $\mathbf{r}_i^j = [\mathbf{r}[i], \dots, \mathbf{r}[j]]$, and the transmitted signal sequence can be written as $\mathbf{a} = [a[0], \dots, a[N_f - 1]]$, and $\mathbf{a}_i^j = [a[i], \dots, a[j]]$. The objective of this algorithm is to calculate the mutual information between the transmitted symbols $\mathbf{a} = [a[0], \dots, a[N_f - 1]]$ and the received signal, given by

$$C = I(\mathbf{a}; \mathbf{r}_0^{N_f - 1}) \triangleq \lim_{N_f \rightarrow \infty} \frac{1}{N_f} I(a[0], \dots, a[N_f - 1]; \mathbf{r}[0], \dots, \mathbf{r}[N_f - 1]) \quad (4.52)$$

Under the assumption that these processes and the state process of the CPM trellis, $\mathbf{S} = [S_0, S_1, S_2, \dots]$, satisfy

$$p(\mathbf{a}_0^n, \mathbf{r}_0^n, s_0^n) = p(s_0) \prod_{i=0}^n p(a[i], \mathbf{r}[i], s_{i+1}|s_i), \quad (4.53)$$

and

$$\mathcal{E} (|\log p(\mathbf{r}[1]|s_0, s_1, a[0])|) < \infty \quad (4.54)$$

the sequence $\frac{1}{N_f} \log_2 p(\mathbf{r}_0^{N_f-1})$ converges with probability 1 to the entropy rate $h(\mathbf{r})$. Therefore, the estimated mutual information is given by

$$\hat{I}(\mathbf{a}; \mathbf{r}_0^{N_f-1}) \triangleq -\frac{1}{N_f} \log_2 p(\mathbf{r}_0^{N_f-1}) - h(\mathbf{r}_0^{N_f-1}|\mathbf{a}) \quad (4.55)$$

where $h(\mathbf{r}_0^{N_f-1}|\mathbf{a})$ is known analytically to be $h(N)$, the entropy of a complex Gaussian random variable, given by

$$h(N) = N_T \log_2 (\det(e\pi N_0 \mathbf{C})), \quad (4.56)$$

where \mathbf{C} is the $D \times D$ array of cross-correlations of the basis functions that form the D complex filters used to obtain sufficient statistics at the front-end of the receiver (see Section 1.2.1). The entropy $h(\mathbf{r})$ can be calculated by generating long sequences $\mathbf{a}_0^{N_f-1}$ and $\mathbf{r}_0^{N_f-1}$ ($N_f \geq 10^6$ symbols [83]) and using the forward metric generated by the BCJR algorithm. The probability $p(\mathbf{r}_0^{N_f-1})$ can be found to be [see (4.22), (4.29)]

$$\log \left(p(\mathbf{r}_0^{N_f-1}) \right) = \sum_{s_{N_f-1}} \alpha_{s_{N_f-1}}(s_{N_f-1}). \quad (4.57)$$

where α_{s_i} is given in Section 4.1.3. Commonly, the forward metric is normalized at each step (i.e. each calculation of $\alpha_i(s_i)$) because $\alpha_i(s_i) \rightarrow -\infty$ for long sequences. If the normalization factor λ_i^{norm} is introduced such that $\lambda_i^{\text{norm}} = -\max \lim^*(\sum_{s_n} \alpha_{s_n}(s_n))$, then the probability $p(\mathbf{r}_0^{N_f-1})$ is given by

$$\frac{1}{N_f} \log \left(p(\mathbf{r}_0^{N_f-1}) \right) = -\frac{1}{n} \sum_0^n \lambda_i^{\text{norm}} \quad (4.58)$$

and finally the estimated capacity can be written as

$$\hat{C} = \frac{1}{\log(2)} \frac{1}{N_f} \sum_{i=0}^{N_f-1} \lambda_i^{\text{norm}} - N_T \log_2 (\det(e\pi N_0 \mathbf{C})). \quad (4.59)$$

The estimated capacity vs. SNR for CPM with $M = 4$, a 1REC phase pulse, and with $h = 1/4$ is shown in Figure 4.10. If we correct for the overall rate of the concatenated coding system we can generate the ‘rate distortion’ BER [89], given by

$$\text{BER} = H^{-1} \left(1 - \frac{\hat{C}}{R} \right), \quad \text{BER} \leq 0.5, \quad (4.60)$$

where R is the target rate of the code, and $H^{-1}(x)$ denotes the inverse of the binary entropy function $H(x) = -x \log_2(x) - (1-x) \log_2(1-x)$ [90], which is unique for $\text{BER} \leq 0.5$.

4.3.2 Quasi-Static Fading Channel

Due to the fading nature of the QSFC outage probability, P_{out} , is a more useful measure of performance in this environment than capacity. Outage probability is the probability that the instantaneous capacity of the channel is less than the outage capacity of the channel. For example, if the concatenated ST–CPM scheme under study transmits C_{out} bits/channel use then with probability P_{out} the instantaneous capacity of the channel is less than C_{out} .

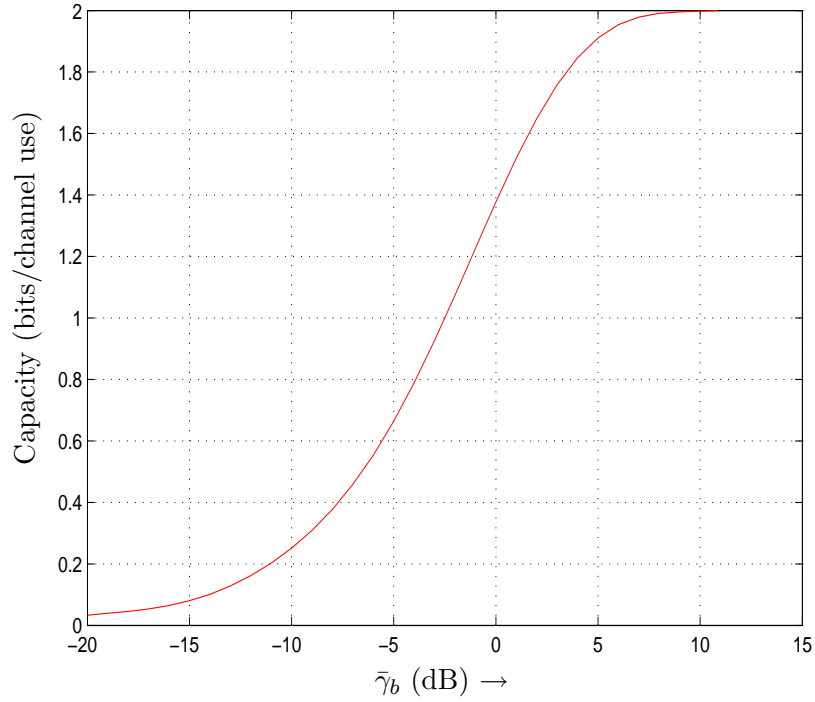


Figure 4.10: Estimated Capacity for $M = 4$ CPM employing a 1REC phase pulse, and with $h = 1/4$.

Thus, the outage probability will provide a lower bound for the frame error rate (FER) of the scheme under study. First, we must find an expression for instantaneous capacity. In a manner similar that used in Section 4.2.3, we can write an expression for the instantaneous capacity of the ST–CPM scheme in the QSFC when repetition coding is employed as

$$\hat{C}_{\text{QSFC}}(\gamma_b) = \hat{C}(\bar{\gamma}_b \sum_{n_r=1}^{N_R} \sum_{n_t=1}^{N_T} |g_{n_r n_t}|^2). \quad (4.61)$$

Then, the outage probability can be written as

$$P_{\text{out}} = \Pr\{(\hat{C}_{\text{QSFC}}(\gamma_b)) < \hat{C}_{\text{out}}\}. \quad (4.62)$$

For a given CPM scheme the estimated capacity can be generated over a range of $\bar{\gamma}_b$ as shown in Figure 4.10. Using these results the SNR required to support desired CPM scheme at capacity, γ_{out} , can be determined. Then, the expression for outage probability can be re-written as

$$P_{\text{out}} = \Pr\left\{\sum_{n_r=1}^{N_R} \sum_{n_t=1}^{N_T} |g_{n_r n_t}|^2 < \frac{\gamma_{\text{out}}}{\bar{\gamma}_b}\right\}, \quad (4.63)$$

The random variable produced by the sum of the squared magnitudes of channel gains has a chi-squared distribution. Thus, finally, using the cumulative density function (cdf) of a chi-squared distribution, we can write the outage probability as

$$P_{\text{out}} = 1 - e^{-\left(\frac{\gamma_{\text{out}}}{\bar{\gamma}_b}\right)} \sum_{n=0}^{N_R N_T - 1} \frac{1}{n!} \left(\frac{\gamma_{\text{out}}}{\bar{\gamma}_b}\right)^n. \quad (4.64)$$

4.4 Results and Discussion

In this section we employ the EXIT chart to select the best symbol labelings for a select group of ST–CPM concatenated codes. The BER performances of these symbol labelings are compared to appropriate capacity limits derived in Section 4.3.1 in the case of the AWGN noise channel, and similarly the appropriate outage probabilities derived in Section 4.3.2 in the case of the block fading channel. We conclude the section with a comparison of the performance of the proposed scheme and pre-existing concatenated CPM, and ST–CPM schemes.

4.4.1 The AWGN Channel

In this section, we consider the performance of single antenna ST–CPM concatenated with the DPC codes, for $M = 2, 4$ and 8-ary CPM schemes. We attempt to minimize the

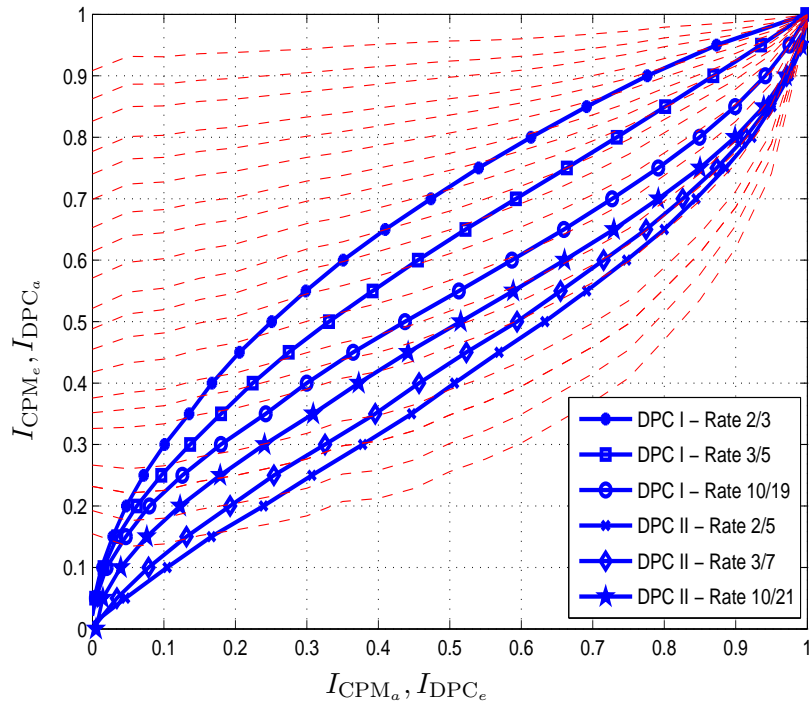


Figure 4.11: The mutual information transfer characteristics of a select group of DPC I and DPC II codes, and MSK (CPM: $M = 2$, 1REC phase pulse and $h = 1/2$) with E_b/\mathcal{N}_0 in steps of 0.5 dB.

complexity of the ST–CPM for each value of M , using the 1RC, 1REC, and 2RC waveforms. We employ a pseudo-random (S-random) spread interleaver, which has been shown to yield performance superior to many random interleavers [91]. Using the performance analysis presented in this section we will show that the DPC class of codes are a good fit for concatenation with CPM. Analysis of multiple transmit and receive antenna is reserved for the block fading channel, and is given in Section 4.4.2.

First, we consider binary CPM. The EXIT chart displaying the mutual information transfer characteristics for MSK ($M = 2$, a 1REC phase pulse, and $h = 1/2$) and for DPC I, and DPC II class codes are shown in Figure 4.11. The MSK transfer characteristics are shown for a range of values of received SNR. From the characteristics shown in the figure

DPC Code	$h = 1/2$	
	Capacity (dB)	Threshold SNR (dB)
Code I - 2/3	1.21	3.39*
Code I - 3/5	0.86	2.27*
Code I - 10/19	0.44	1.39
Code II - 2/5	-0.02	1.23
Code II - 3/7	0.034	1.31
Code II - 10/21	0.22	1.44

Table 4.3: SNR to achieve capacity vs. threshold SNR from EXIT chart analysis for MSK. Note that (*) denotes schemes whose EXIT chart tunnel opens after the ‘threshold’ SNR given in this Table.

it is evident that SNR required to open a tunnel between the DPC II class of codes and MSK is less than is required for the DPC I codes. In fact, due to the shape of the MSK mutual information transfer characteristic the SNR required to completely open a tunnel between the MSK and DPC I transfer characteristics is much higher than is needed for the DPC II codes. However, increasing SNR gradually opens the EXIT chart tunnel for MSK and the DPC I codes. Thus, although the BER performance of MSK concatenated with the DPC I codes does not exhibit the waterfall characteristic until a higher SNR is reached than its DPC II counterpart, the BER performance improves significantly with increasing SNR. The EXIT chart predicts the onset of the BER waterfall at 1.23, 1.38, and 1.42 dB for MSK and the DPC II rate 2/5, 3/7, and 10/21 codes respectively. The EXIT chart tunnel does not completely open until SNRs of 6.26, 3.21, and 1.79 dB for MSK and the DPC I rate 2/3, 3/5, and 10/19 rate codes, respectively. However, the tunnels for the MSK and DPC I rate codes (most notably the 2/3 and 3/5 rate codes) are mostly open at significantly lower SNRs. If we define the threshold SNRs to be the SNR at which a BER of 10^{-3} is reached then the threshold SNRs and the SNR for transmission at capacity for MSK are given in Table 4.3.

DPC Code	$h = 1/3$		$h = 1/4$	
	Capacity (dB)	Threshold SNR (dB)	Capacity (dB)	Threshold SNR (dB)
Code I - 2/3	1.61	3.81*	2.96	2.39*
Code I - 3/5	1.17	2.30*	2.27	3.97**
Code I - 10/19	0.84	1.74	1.69	3.09
Code II - 2/5	-0.02	1.23	0.78	2.38
Code II - 3/7	0.08	1.13	0.93	2.48
Code II - 10/21	0.32	1.42	1.27	2.52

Table 4.4: SNR to achieve capacity vs. threshold SNR from EXIT chart analysis for binary 1REC with $h = 1/3$ and $h = 1/4$. Note that (*) denotes schemes whose EXIT chart tunnel opens after the ‘threshold’ SNR given in this Table.

The simulated BER performance of MSK concatenated with the DPC codes is shown in Figure 4.12 (non-bold curves). An interleaver of 8000 bits is employed. Rate distortion capacity curves (bold curves) are also shown for reference in Figure 4.12. The performance of the DPC II codes (shown on the right of the figure) is well predicted by the EXIT chart. The 2/3, and 3/5 rate DPC I codes (shown on the left of the figure) do not exhibit the very sharp BER waterfall characteristic, but do demonstrate a substantial BER drop with increasing SNR as the EXIT chart opens. All of the DPC I codes have error floors. We note, even at high SNR the tunnel between the MSK transfer characteristic and the characteristics of the DPC I codes is not very large. Table 4.4 contains the SNR needed to achieve capacity and the threshold SNRs for binary, 1REC, with $h = 1/3$, and $h = 1/4$. Note again, a BER of 10^{-3} determines the threshold SNR. In general, the performance of the ST-CPM code with the DPC II class of codes is superior to that of the DPC I class of codes (particularly the rate 2/3, and rate 3/5 codes. Therefore, in the remainder of this chapter we will employ the DPC II class of codes.

Next, we consider 4-ary CPM. The EXIT chart for CPM with $M = 4$, $h = 1/4$, a 1REC phase pulse and the rate 10/21 DPC II code is shown in Figure 4.13. The threshold

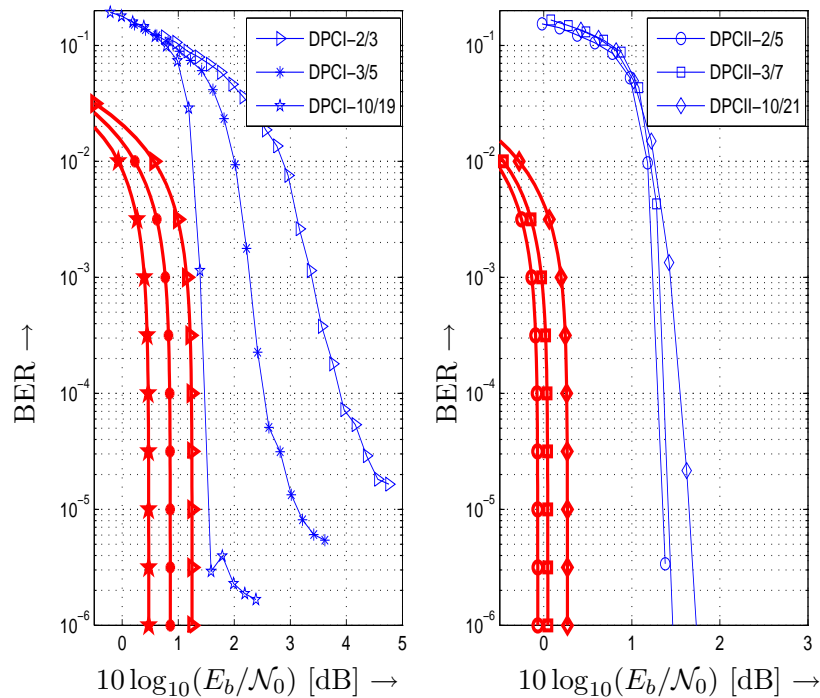


Figure 4.12: Estimated capacity (bold curves) and simulated BER (non-bold curves) vs. $10 \log_{10}(E_b/N_0)$ for MSK (CPM: $M = 2$, 1REC phase pulse and $h = 1/2$) concatenated with DPC I class codes (in the figure to the left) and DPC II class codes (in the figure to the right).

SNRs for the three labelings that produce distinct transfer characteristics are shown. The Gray labeling yields the lowest threshold SNR (1.3 dB), but the threshold SNR of the three labelings are separated by only 0.2 dB. Although, the transfer characteristics of the three labelings are not strikingly different, we note that the size of the EXIT channel tunnel opening is different for the different schemes before the threshold SNR is reached (i.e. before the tunnel completely opens). Before the threshold SNR is reached the GL2 scheme has the smallest unopened tunnel size, followed by the UL scheme, and then the GL1 scheme. We also note that at the upper right hand of the EXIT chart, when large quantities of mutual information are being exchanged, the GL2 provides the largest tunnel opening, followed by the UL labeling, and finally the GL1 labeling.

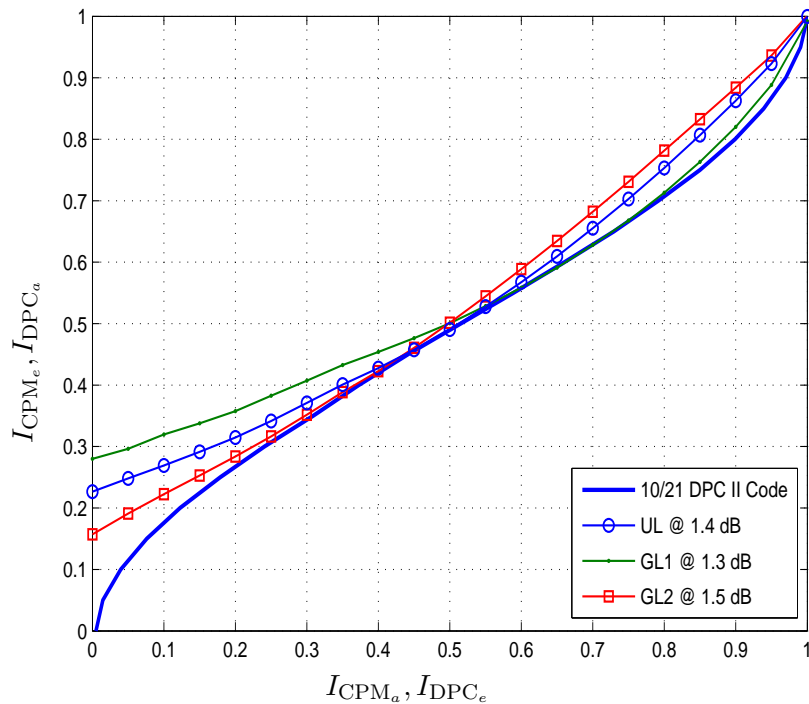


Figure 4.13: EXIT chart showing the threshold SNR for three labelings of CPM ($M = 4$, $h = 1/4$, a 1REC phase pulse) and the rate 10/21 DPC II code. SNR is E_b/\mathcal{N}_0 .

Figure 4.14 shows the simulated BER results for the $M = 4$ scheme just described. Again, the rate distortion capacity curve is provided for reference. BER results are shown for an interleaver length of 4200, and 8400 bits. First, we consider the performance of the three labelings when the interleaver length is 4200 bits. Given the fact that the three labelings have comparable threshold SNRs, the size of the tunnel opening prior to the threshold SNR has a significant affect on the shape and ordering of the BER curves in the 10^{-1} to 10^{-2} BER region. In fact, the BER can be determined directly from the *a priori* at the input of the DPC decoder, and the extrinsic information at the output of the DPC decoder for any point on the decoding trajectory [85]. Thus, when schemes have similar threshold SNR, the shape of the mutual information transfer characteristic takes on an added importance. From Figure 4.14, we see that as SNR is increased the GL2 labeling

provides superior performance, and the GL1 labeling encounters an error floor. This ordering can be attributed to the relatively short interleaver length, and the size of the tunnel opening at high values of mutual information (i.e. at the upper right hand corner of the EXIT chart). As discussed earlier when a short interleaver is employed correlation amongst the extrinsic information generated by the decoders reduces the actual amount of mutual information exchanged from the values predicted by the EXIT chart. If the EXIT chart is already narrow the iterative decoding process may terminate prematurely causing an error floor. Therefore, when a short interleaver is employed the size of the opening of the EXIT chart tunnel is an important consideration. To see the effect of a longer interleaver, we now look at the results of the 8400 bit interleaver. In this case none of the mappings encounters an error floor before a BER of 10^{-7} . We note that the $M = 4$, GL labeling scheme that we have considered provides BER performance within 1.2 dB of capacity.

Finally, we consider 8-ary CPM. The mutual information transfer characteristics of five of the six 8-ary labelings given in Table 4.2 are shown in Figure 4.15 for CPM with $h = 1/4$ and a 2RC phase pulse. The mutual transfer characteristic of the HL is not shown as it is almost identical to the characteristic of the SSPL. Of the six labelings only two reach the (1,1) point of mutual information when the ‘tunnel’ opens at a relatively low SNR. The other four labelings are expected to demonstrate the BER waterfall characteristic but to produce BER error floors. The two labelings that reach the point of (1,1) of mutual information are the AGL and NAL labelings. The NAL labeling scheme has a threshold SNR of 1.0 dB, and the AGL labeling has a threshold of 0.9 dB and wider opening between the inner and outer mutual information transfer characteristics at low SNR.

Figure 4.16 shows the simulated BER results for the $M = 8$ scheme just described. The rate distortion capacity is provided for reference. An interleaver of 4200 bits is used. For reference the performance of the UL scheme is shown in Figure 4.16. As expected the

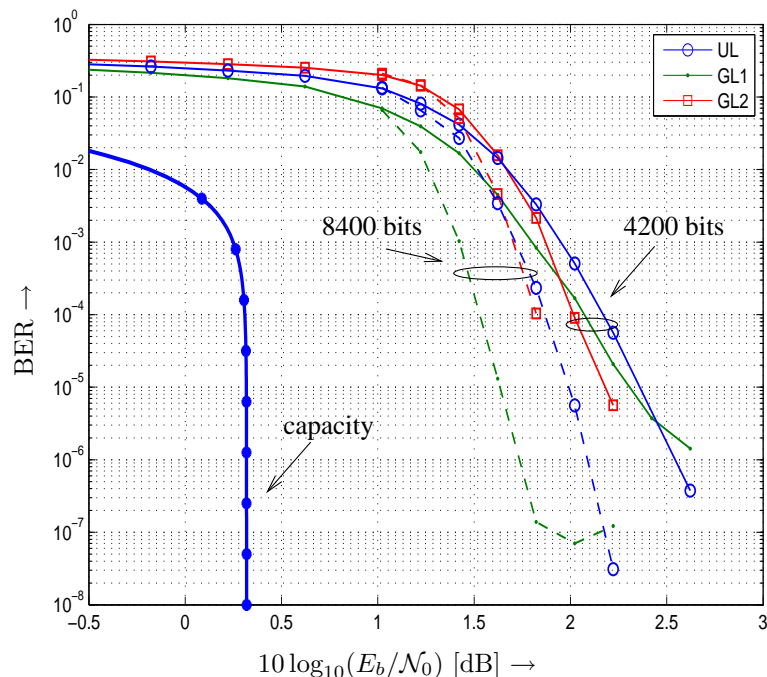


Figure 4.14: Estimated capacity (bold curve) and simulated BER (non-bold curves) vs. $10 \log_{10}(E_b/N_0)$ for CPM: $M = 4$, 1REC phase pulse and $h = 1/4$) concatenated with the rate 10/21 rate DPC II code.

UL labeling scheme has an error floor at a relatively high BER (at 10^{-4}). The AGL code provides BER performance within approximately 1 dB of capacity.

4.4.2 Block Fading Channel

In this section, we consider the QSFC and the performance of proposed concatenated coding scheme employing ST–CPM. In this section will set $N_R = 1$, and assume the outer code is the DPC II, rate 10/21 code. The transmitted energy per bit \bar{E}_b is always normalized with respect to the number of transmit antenna. The ST–CPM coding scheme employs repetition coding with the symbol labelings listed in Tables 4.1 and 4.2. It is worth noting that repetition codings reduces the complexity of the DBST coding scheme from $p^{N_T} M^{L-1}$ states to $p M^{L-1}$ states.

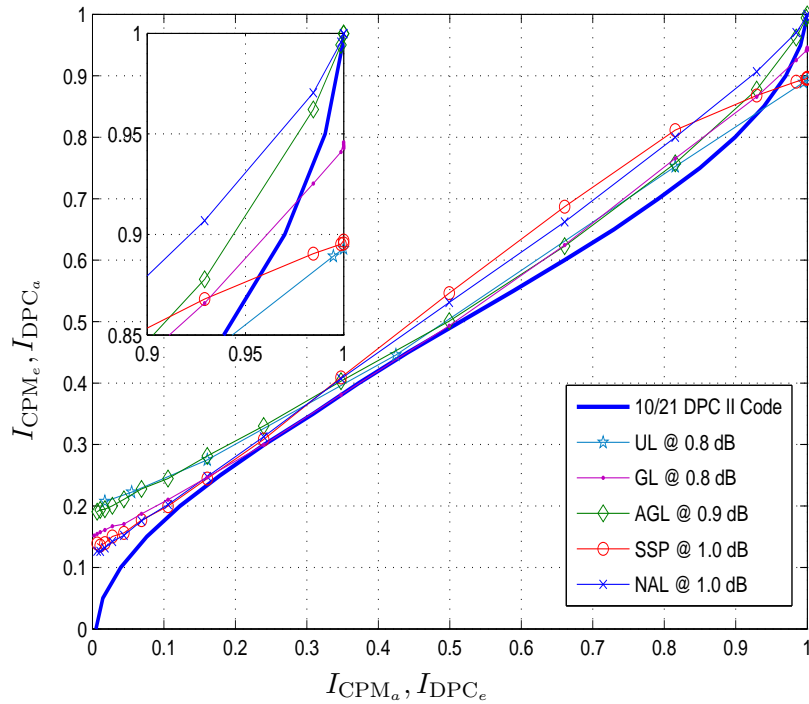


Figure 4.15: Mutual information transfer chart for the ST–CPM code employing $N_T = 1$ transmit antenna, and $M = 8$, $h = 1/4$, a 2RC pulse, and with a SNR of $10 \log_{10}(E_b/\mathcal{N}_0) = -2.0$ dB and the symbol mappings given in Table 4.2.

We begin with the performance of scheme employing $M = 4$, and $N_T = 2$. The CPM scheme considered is 1REC with $h = 1/4$. The EXIT chart for this scheme is shown in Figure 4.17. The spread of threshold SNRs in this case is 2.4, 3.8, and 3.0 dB for UL, GL1, and GL2, respectively. Once again, we note that prior to the threshold SNR the EXIT chart tunnel is most open for GL1, followed by GL2, and then UL.

The second scheme we consider employs $M = 8$, and $N_T = 3$. The CPM scheme uses the 2RC phase pulse, with $h = 1/4$. The EXIT chart for this scheme is shown in Figure 4.18. The mutual information transfer characteristics for the UL and the AGL are shown in the EXIT chart. The AGL labeling has a threshold SNR of 1.4 dB, whilst the UL does not open a tunnel until an SNR of 10 dB is reached. The FER performance of these schemes

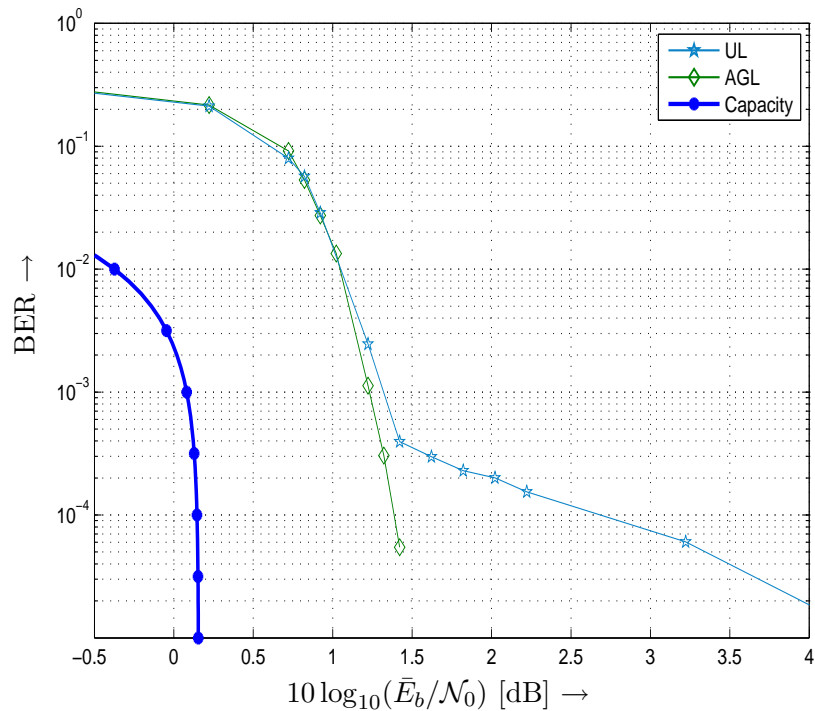


Figure 4.16: Estimated capacity (bold curve) and simulated BER (non-bold curves) vs. $10 \log_{10}(\bar{E}_b/\mathcal{N}_0)$ for CPM: $M = 8$, 2RC phase pulse and $h = 1/4$) concatenated with the rate 10/21 rate DPC II code.

is shown in Figure 4.19. The FER performance of the concatenated ST–CPM scheme with $N_T = 2$ antenna provides performance within 0.7 dB of the outage probability at capacity up to a FER of almost 10^{-3} . The different symbol mappings for $N_T = 2$ provide very similar performance. The 1.4 dB spread of threshold SNRs for $N_T = 2$ is a relatively small margin in the QSFC, and the shape of the mutual information transfer characteristics is such that, for example, although the GL1 labeling has the highest threshold its tunnel is also open to the furthest right (of the three labelings considered) of the EXIT chart before the threshold SNR is reached.

As expected the AGL labeling provides performance superior to the UL for $N_T = 3$ at low to moderate SNR. At high SNR the tunnel opens for the UL and the scheme provides

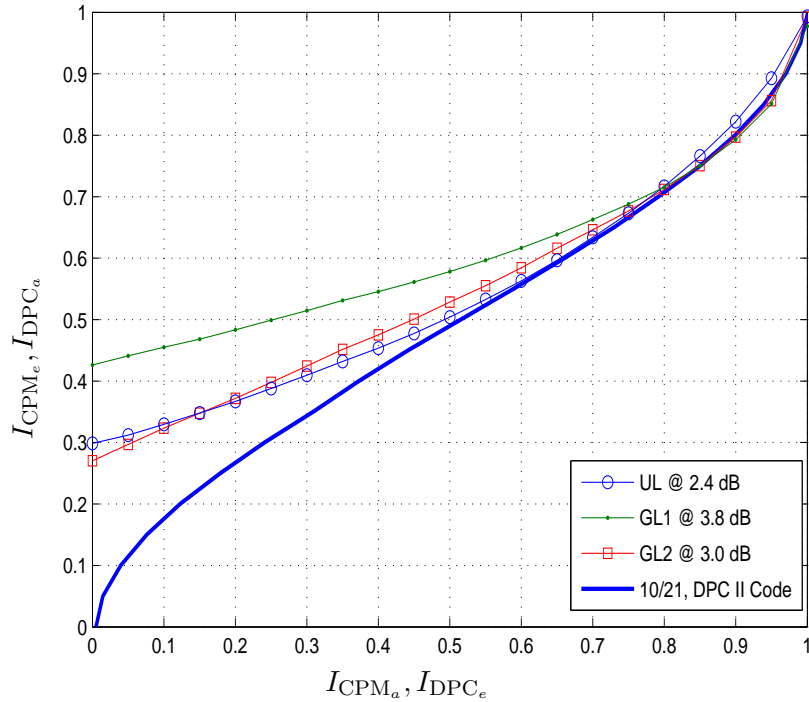


Figure 4.17: EXIT chart for $N_T = 2$ ($M = 4$, 1REC, $h = 1/4$) and the 10/21 rate DPC II code. The UL, GL1 and GL2 are shown at their threshold SNRs.

performance comparable to the AGL. However, by selecting the AGL, a FER performance within 0.5 dB of the outage probability at capacity is provided. Finally, we note that the concatenated coding schemes presented in Figure 4.19 have the same rate, and consume the same amount of energy. Thus, increasing the number of transmit antenna provides an excellent means to improve system performance.

4.4.3 Comparison with Previous Work

In this section, we compare the performance of the proposed scheme with that of existing concatenated ST–CPM, and concatenated CPM coding schemes. We first make a comparison of the performance of the proposed concatenated CPM code without considering the ST aspect. Using this comparison we can properly evaluate the merit of the proposed

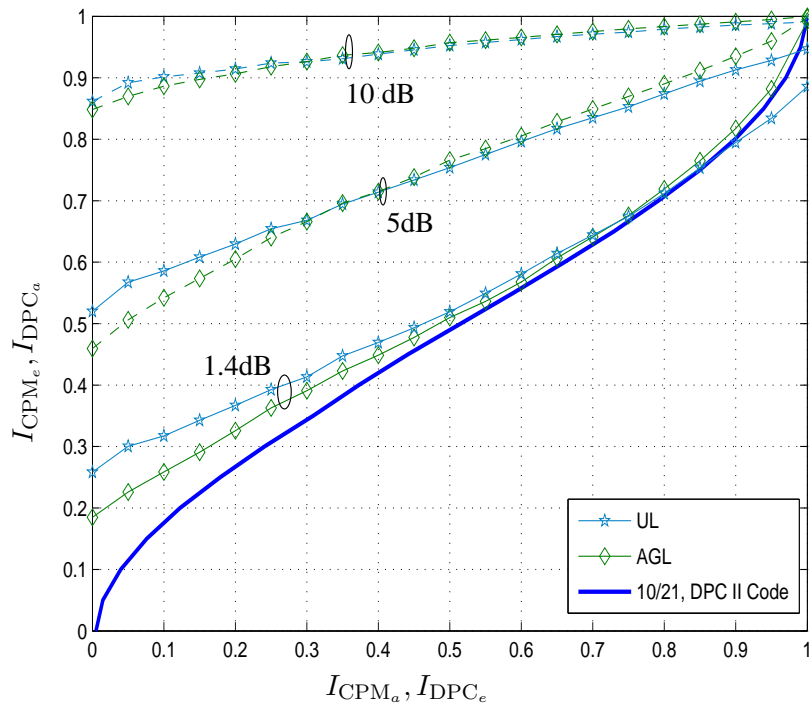


Figure 4.18: EXIT chart for $N_T = 3$ ($M = 8$, 2RC, $h = 1/4$) and the 10/21 rate DPC II code. The UL and SSPL are shown for SNRs of 1.4, 5.0, and 10.0 dB.

pairing of the DPC class of codes with CPM. To date, all of the proposed schemes for concatenated codes ST–CPM employ convolutional codes, e.g. Zhang and Fitz [8], Bokolamulla and Aulin [9], and Gabrowska *et al.* [23]. In fact, most of the work on concatenated CPM employs convolutional codes. Therefore, the first comparison that we make is with the concatenated CPM code proposed by Moqvist and Aulin in [7]. Figure 4.20 shows the performance of MSK paired with a (7,5) convolutional code when transmitting over an AWGN channel. The performance of this scheme is shown for interleaver lengths of 128, 512, 2048, and 8192 bits. Also shown in the figure is the performance of MSK concatenated with the DPC 10/21 code (in this case the interleaver lengths are closely approximated by 126, 525, 2058, and 8190 bits). The performance of the concatenated CPM–DPC code clearly outperforms the performance of the concatenated CPM–CC code. Therefore, the

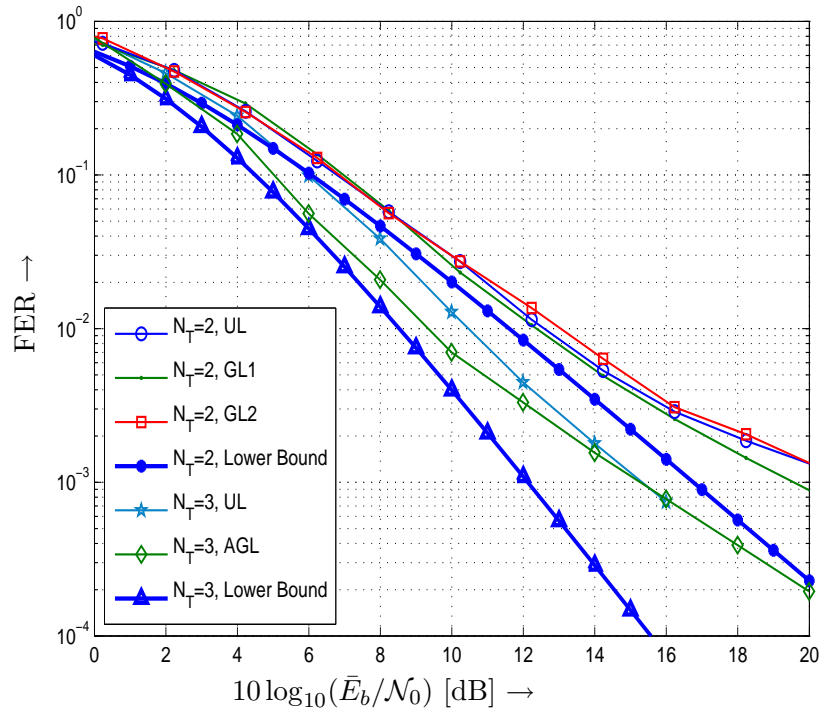


Figure 4.19: Estimated outage probability (bold curve) and simulated FER (non-bold curves) vs. $10 \log_{10}(\bar{E}_b/\mathcal{N}_0)$ for concatenated ST–CPM. Results for $N_T = 2$ ($M = 4$, 1REC, $h = 1/4$), and $N_T = 3$ ($M = 8$, 2RC, $h = 1/4$) and the 10/21 rate DPC II code. UL, GL1, and GL2 shown for $N_T = 2$, and UL, and SSPL shown for $N_T = 3$.

DPC class of codes are good fit for use with CPM, and promise competitive performance in a space-time system.

The second comparison we make with delay diversity concatenated ST–CPM scheme proposed by Zhang and Fitz [8]. The scheme employs a (7,5) convolutional code, and 1RC, $h = 1/4$, $M = 4$ delay diversity CPM, and $N_T = 2$ transmit antennas and $N_R = 2$ receive antennas. We use the same underlying ST–CPM scheme and replace the (7,5) convolutional code with the rate 10/21 DPC II code. An interleaver of 256 bits is employed and a maximum of 5 iterations are permitted. The FER performance of these schemes over a continuous fading channel with a fading bandwidth $B_f T = 0.008$ is shown in Figure 4.21. Note that the FER results shown in the figure are taken from [9], where the scheme proposed

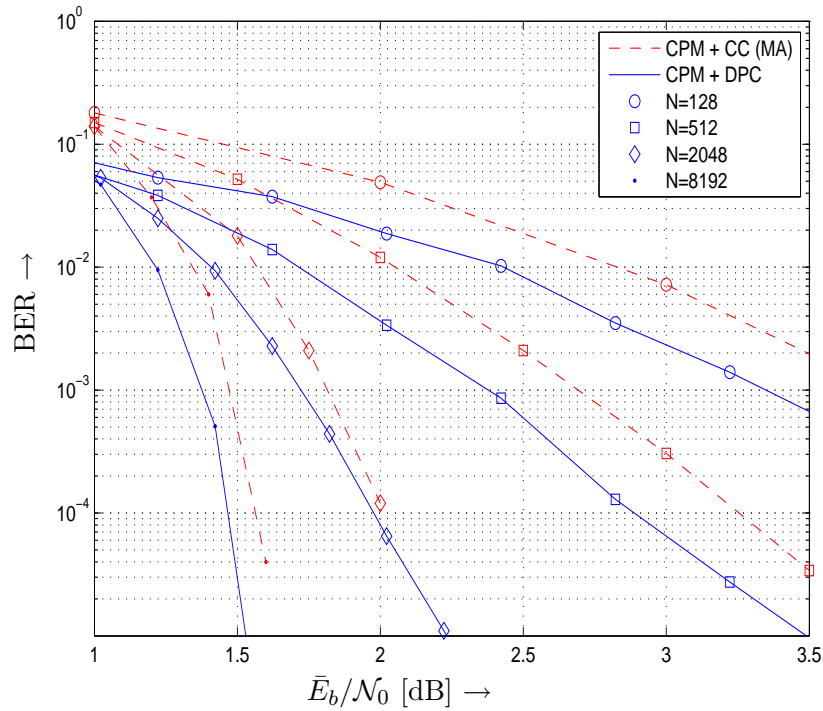


Figure 4.20: BER vs. $10 \log_{10}(\bar{E}_b/\mathcal{N}_0)$ for the concatenated CPM scheme proposed by Moqvist and Aulin in [7], and for the proposed scheme employing MSK concatenated with the rate 10/21 DPC II code over an AWGN channel.

in [8] was employed with an improved detector. Once again the FER performance results show that the pairing of the DPC code with CPM is an improvement over a pairing with a convolutional code.

Few results exist for the performance of concatenated ST–CPM coding schemes in QSFC. Bokomulla and Aulin [9] studied the performance of their proposed scheme when fading remained constant over a number of symbols rather than over an entire frame. We compare the performance of the proposed with that of ‘System B’ in [9]. This scheme employs $N_T = 2$, and $N_R = 2$ antenna, a (7,5) convolutional outer code, MSK, and a 600 bit interleaver. Full diversity is achieved by offsetting the carrier frequencies of the different transmit antenna by the normalized value $\Delta fT = 1/6$. The overall rate of

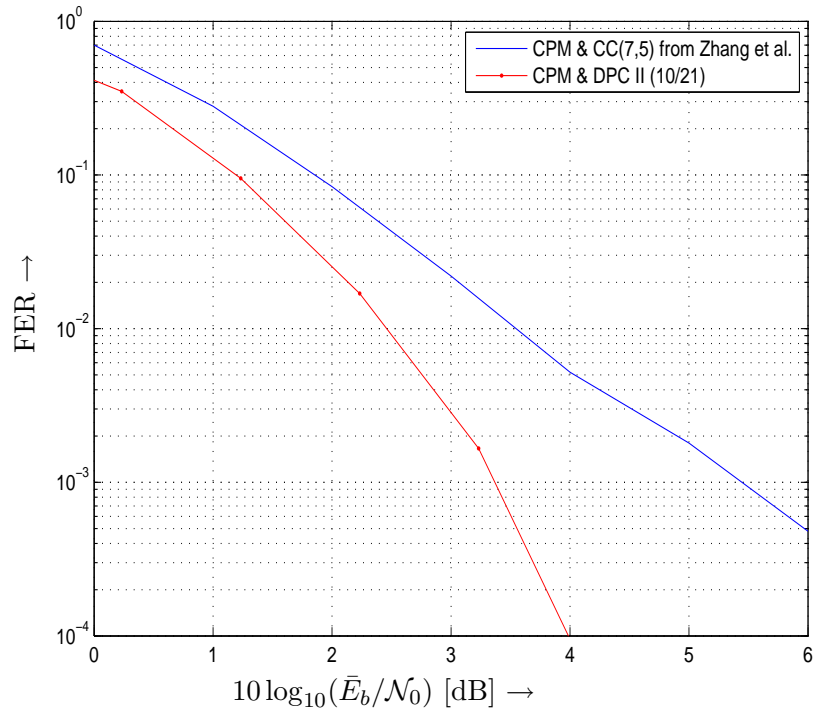


Figure 4.21: FER vs. $10 \log_{10}(\bar{E}_b/\mathcal{N}_0)$ for the concatenated CPM scheme employing a (7,5) convolutional code as proposed by Zhang and Fitz in [8], [9], and the performance of CPM concatenated with the rate 10/21 DPC II code. The channel is a continuous fading channel with fading bandwidth $B_f T = 0.008$, and $N_T = 2$, $N_R = 2$ antenna are employed. The underlying CPM scheme is 1RC, $h = 1/4$, $M = 4$. The interleaver length is 256 bits, and 5 iterations are used.

the code is 0.5 bits per symbol duration T , and excluding the frequency offset it has a normalized bandwidth of $B_{99}T = 1.18$. Due to the diagonal structure of our proposed code we employ CPM with the 2RC phase pulse, $M = 4$, and $h = 1/4$. We use the DPC II code with rate 10/21. The overall rate of the code is 0.4762 bits per symbol duration, and it has a normalized bandwidth of $B_{99}T = 1.24$. In Figure 4.22 the performance of the Bokomullla and Aulin scheme is compared with that of the proposed scheme when fading is constant for $f = 1, 10$ and 30 symbol intervals, and 10 iterations are permitted. The proposed scheme provides comparable or superior performance regardless of the duration of the fading interval. Significant improvement is observable as the fading duration is

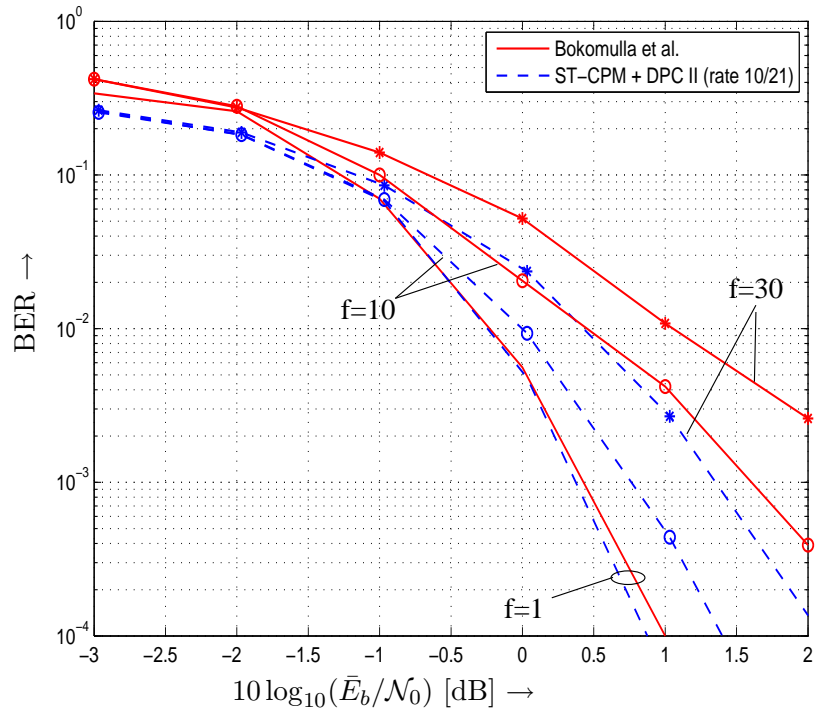


Figure 4.22: BER vs. $10 \log_{10}(\bar{E}_b/\mathcal{N}_0)$ for the concatenated CPM scheme denoted as ‘system B’ by Bokomulla and Aulin [9], and the proposed scheme. Both schemes employ $N_T = 2$, $N_R = 2$, and a 600 bit interleaver. ‘System B’: (7,5) convolutional outer code, MSK and a $\Delta fT = 1/6$ normalized carrier offset. ST-CPM and DPC code: rate 10/21 DPC II code, 2RC phase pulse, $M = 4$, and $h = 1/4$. The channel is a QSFC constant for $f = 1, 10, 30$ symbol intervals. 10 iterations are permitted.

increased.

We include no comparisons with the performance of the scheme proposed by Gabrowska *et al.* [23] due to the rate difference of the codes. The set of concatenated ST-CPM codes proposed in this chapter are by design highly flexible, low-rate, low complexity codes that are capable of non-coherent detection. The set of codes proposed by Gabrowska *et al.* have a high rate (the overall code rate is 1), but also a much higher degree of complexity at the receiver. The Gram–Schmidt decomposition employed by Gabrowska *et al.* replaces the CPM waveform with $L(M - 1) + 1$ linear waveforms. In addition, this decomposition was previously designed specifically for CPFSK signals and all other CPM formats considered

by Gabrowska *et al.* are approximated as LREC signals, which may result in a performance degradation for CPM formats other than CPFSK. Lastly, no mechanism for non-coherent detection of the codes proposed by Gabrowska *et al.* is discussed in [23]. Thus, the set of codes proposed in this chapter may be a better fit for many strictly cost and energy constrained, *ad-hoc* wireless applications.

4.5 Conclusions

A serially concatenated code for ST–CPM has been proposed. The concatenated code employs the diagonal block-based ST code proposed in Chapter 2 as an inner code, and a class of double parity check codes as the outer code. In order to evaluate the merit of the proposed scheme a method for estimating the capacity of underlying ST–CPM scheme in AWGN and over a QSFC was proposed. EXIT charts were employed to select the best CPM symbol labelings for the ST–CPM code. The concatenated code formed from the ST–CPM code and the DPC codes was shown to provide performance close to capacity, and to provide performance superior to that provided by CPM, and ST–CPM schemes that are concatenated with the commonly used convolutional code.

Chapter 5

Conclusions and Future Work

In this chapter, we conclude the thesis by summarizing our results and highlighting the contributions of this dissertation. We also suggest several topics for further research.

5.1 Research Contributions

In this thesis, we have proposed space-time (ST) codes for use with continuous phase modulation (CPM). In Chapter 2, we began by proposing a code that supports the combination of CPM with orthogonal designs (ODs). Then, we proposed a ST-CPM code using a diagonal signalling matrix. In Chapter 3, we used the ST-CPM code with the diagonal signalling matrix as the basis for a distributed ST-CPM code. Finally, in Chapter 4, we proposed combining a ST-CPM with a diagonal signalling matrix with a double parity check (DPC) code to form a serially concatenated code.

Specifically, in Chapter 2 we begin with the proposal of a simple orthogonal space-time block coding (OSTBC) technique for CPM. Although the straightforward combination of orthogonal designs (ODs) and CPM was deemed impossible in [1] and [15], the burst-based approach accomplishes the task in very simple manner. The resulting ST-CPM code can be combined with any CPM format. After an appropriate ST combining at the receiver, the OSTBC scheme can utilize the same detection techniques as for a single-antenna transmission scheme. Thus, the proposed scheme entails a lower complexity than all previously proposed ST coding schemes for CPM. Additionally, simulation results along

with accurate approximations that were derived for the bit error rate (BER) and the frame error rate (FER) of CPM with OSTBC show that this scheme yields a better performance for the important case of $N_T = 2$ transmit antennas. For $N_T > 2$ transmit antennas OSTBC for CPM suffers from the same rate loss as all ST coding schemes based on ODs.

In the second part of Chapter 2 an alternate ST–CPM coding scheme was presented. This scheme also employs a block–based approach to preserve the properties of CPM, but in this case makes use of a diagonal signalling matrix rather than an OD. The resulting diagonal block-based ST–CPM (DBST–CPM) scheme facilitates non-coherent detection at the receiver in addition to providing increased energy efficiency. It was noted that DBST-CPM can be regarded as a non-trivial extension of the well-known differential ST modulation (DSTM) scheme with diagonal signal matrices for linear modulation formats. An upper bound on the frame-error rate of DBST–CPM in the quasi-static fading channel (QSFC) was derived for use in optimizing the DBST-CPM code. Also, an efficient code optimization algorithm was presented. Additionally, decision rules were derived for low-complexity non-coherent detection of DBST-CPM in various fading environments. Numerical and simulation results showed that (a) the derived upper bound accurately predicts the performance of DBST-CPM in the QSFC, (b) the proposed code optimization yields highly power-efficient designs, and (c) the non-coherent detectors approach the performances of their coherent counterparts for various fading channel models.

In Chapter 3 we presented and analyzed the energy consumption of a distributed ST code for CPM. The distributed ST codes were designed to operate in wireless networks containing a large set of nodes \mathcal{N} , of which only a small *a priori* unknown subset $\mathcal{S} \subset \mathcal{N}$ were active at any time. Under the proposed scheme, a relay node transmits a signal which is the product of DBST–CPM code presented in Chapter 2 (optimized specifically for ST-CPM transmission) and a signature vector of length N_c uniquely assigned to each node in

the network. An efficient method was presented for the design and optimization of appropriate signature vector sets, assuming a quasi-static, frequency non-selective fading channel model. It was shown that when a properly designed signature vector set is employed a diversity order of $d = \min\{N_S, N_c\}$ can be achieved, where N_S is the number of active relay nodes. The decoding complexity of the proposed scheme was shown to be independent of the number of active relay nodes. In the same manner as for the underlying DBST-CPM code, non-coherent receiver implementations, which do not require channel estimation, are applicable. Simulation results showed that the performance of the proposed distributed ST-CPM scheme is close to that achievable with co-located antennas. The chapter concluded with a comparison of the total energy (radiated and used in hardware) required to supply a target BER at a maximum transmission distance for the distributed ST-CPM scheme and a distributed ST scheme based upon linear modulation. At high power the CPM based scheme offers significant energy savings, and extended coverage range (from 2.6% to 43.8%). Performance gains were shown to increase with the number of active relay nodes N_s .

Finally, in Chapter 4, we presented a serially concatenated code that used the diagonal ST-CPM code in combination with a double parity check code. EXIT charts were used to select the best performing symbol labelings in the AWGN channel and for the QSFC. A method was proposed to obtain an estimate on the capacity of the diagonal ST-CPM code over the AWGN channel. A lower bound on outage probability for the diagonal ST-CPM code over the QSFC was derived in order to better evaluate the system. Simulation results showed that the concatenated code provided performance close to capacity over the AWGN channel, and achieved performance approaching the lower bound on outage probability over the QSFC. Finally, the concatenated code formed from the ST-CPM code and the DPC codes was shown to provide performance superior to that provided by CPM,

and ST-CPM schemes that are concatenated with the commonly used convolutional code.

5.2 General Conclusions

The ST-CPM codes presented in this thesis are highly flexible codes that can be used with any CPM format, any number of transmit and receive antenna, and can be used with existing CPM receivers. In addition, the DBST-CPM code enables non-coherent detection. CPM allows for the use of energy efficient low power amplifiers. In the case of distributed coding we have shown that ST-CPM can provide considerable energy savings and an extended coverage range in comparison to distributed ST linear coding schemes. Serial concatenation of the ST-CPM code with DPC codes provides low error-rate performance. In summary, the energy efficiency, flexibility, non-coherent detection capability, and performance provided by the proposed ST-CPM coding make this code an excellent candidate for application in wireless networks, especially highly energy constrained networks, such as sensor networks.

5.3 Suggestions for Future Work

1. The energy consumption analysis presented in Chapter 3 could be generalized from the case of distributed ST-CPM coding to ST-CPM code to provide a more holistic picture of the energy savings offered by employing a ST-CPM instead of a linear based code.
2. The serially concatenated ST-CPM coding scheme presented in Chapter 4 uses repetition coding. The scheme could be extended to use different symbol labelings on each of the transmit antenna. Optimal symbol labelings could be selected with the aid of a multi-dimensional EXIT chart.

Bibliography

- [1] X. Zhang and M.P. Fitz. Space-Time Code Design with Continuous Phase Modulation. *IEEE J. Select. Areas Commun.*, 21:783–792, June 2003.
- [2] F. Pancaldi and G.M. Vitetta. Space-Time Block Codes for Noncoherent CPFSK. In *Proc. IEEE Global Telecom. Conf.*, pages 3043 – 3047, St. Louis, Oct./Nov. 2005.
- [3] T. Pande, H. Huh, and J.V. Krogmeier. Non-Coherent Receiver Performance for Orthogonal Space-Time Coded CPM in Fading Channels. In *Proc. 39th Asilomar Conf. on Signals, Systems and Computers*, pages 853 – 856, Oct./Nov. 2005.
- [4] A.-M. Silvester, L. Lampe, and R. Schober. “Diagonal Space-Time Code Design for Continuous-Phase Modulation”. In *Proc. IEEE Global Telecom. Conf.*, San Francisco, November 2006.
- [5] J. Carls, F. Ellinger, R. Eickhoff, P. Sakalas, S. von der Mark, and S. Wehrli. Design of a C-Band CMOS Class AB Power Amplifier for an Ultra Low Supply Voltage of 1.9 V. In *International Microwave and Optoelectronics Conference*, pages 786–789, Aurangabad, India, November 2007.
- [6] S. Cao, W. Lu, S. Cheng, K. Zhang, W. Li, and X. Zhou. A 2.4 GHz Highly Linear Class C Power Amplifier in 0.18 μm CMOS Technology. In *International Conference on ASIC*, pages 427–430, Guilin, China, October 2007.
- [7] P. Moqvist and T.M. Aulin. Serially Concatenated Continuous Phase Modulation with Iterative Decoding. *IEEE Trans. Commun.*, 49:11:1901–1915, November 2001.
- [8] X. Zhang and M.P. Fitz. Soft-Output Demodulator in Space-Time-Coded Continuous Phase Modulation. *IEEE Trans. on Acoustics, Speech, and Signal Processing*, 50:10:2589–2597, October 2007.
- [9] D. Bokolumulla and T. Aulin. Serially Concatenated Space-Time Coded Continuous Phase Modulated Signals. *IEEE Trans. Commun.*, 6:10:3487–3492, October 2007.
- [10] V. Tarokh, N. Seshadri, and A.R. Calderbank. “Space-Time Codes for High Data Rate Wireless Communication: Performance Criterion and Code Construction”. *IEEE Trans. Inform. Theory*, 44:3:744–765, March 1998.
- [11] S.M. Alamouti. A Simple Transmitter Diversity Scheme for Wireless Communications. *IEEE J. Select. Areas Commun.*, 16:1451–1458, October 1998.

- [12] G.J. Foschini and M. Gans. On the Limits of Wireless Communications in a Fading Environment When Using Multiple Antennas. *Wireless Pers. Commun.*, 6:311–335, March 1998.
- [13] E. Teletar. Capacity of Multi-Antenna Gaussian Channels. *European Transactions on Telecommunications*, 10:585–595, November 1999.
- [14] A. Wittneben. Base Station Modulation Diversity for Digital SIMULCAST. In *Proc. of Veh. Technol. Conf.*, pages 848–853, May 1991.
- [15] G. Wang and X.-G. Xia. An Orthogonal Space-Time Coded CPM System with Fast Decoding for Two Transmit Antennas. *IEEE Trans. Inform. Theory*, IT-50:486–493, March 2004.
- [16] J.K. Cavers. Space-Time Coding Using MSK. *IEEE Trans. Wireless Commun.*, TW-05:185–191, January 2005.
- [17] L. Xian, R. Punnoose, and H. Liu. Space-Time Block Coded GMSK With Low-Complexity Linear Receiver. In *Proc. IEEE Int. Conf. Commun.*, pages 2374 – 2378, June 2006.
- [18] A.R. Ahmadi and R.K. Rao. Space-Time Trellis Code Design With Binary CPM. *Electronics Letters*, 42(3):168–170, February 2006.
- [19] W. Zhao and G.B. Giannakis. Reduced Complexity Receivers for Layered Space-Time CPM. *IEEE Trans. Wireless Commun.*, 4(2):574–582, March 2005.
- [20] R.L. Maw and D.P. Taylor. Space-Time Coded Systems with Continuous Phase Frequency Shift Keying. In *Proc. IEEE Global Telecom. Conf.*, pages 1581 – 1586, November 2005.
- [21] S. Yiu, R. Schober, and L. Lampe. Distributed Space-Time Block Coding. *IEEE Trans. Commun.*, 54:7:1195–1206, July 2006.
- [22] J.N. Laneman and G.W. Wornell. “Distributed Space-Time Block Coded Protocols for Exploiting Cooperative Diversity in Wireless Networks”. *IEEE Trans. Inform. Theory*, 49:2415–2425, October 2003.
- [23] M. Gabrowska, M. Bossert, S. Shavgulidze, and S. Schober. Serially Concatenated Space Time Convolutional Codes and Continuous Phase Modulation. *IEEE Trans. Commun.*, 56:9:1442–1450, September 2008.
- [24] J. Mitra and L. Lampe. Serial Concatenation of Simple Linear Block Codes and Differential Modulations. *IEEE Trans. Wireless Commun.*, 7:1477–1482, May 2008.
- [25] B.E. Rimoldi. A Decomposition Approach to CPM. *IEEE Trans. Inform. Theory*, IT-34:260–270, March 1988.

- [26] J. Huber and W.L. Liu. An Alternative Approach to Reduced-Complexity CPM-
Receivers. *IEEE J. Select. Areas Commun.*, SAC-7:1437–1449, December 1989.
- [27] Weilin Liu. *Complexity Reduction for Coherent Receivers for Digital Continuous Phase
Modulation*. Doktor-Ingenieur, Universität der Bundeswehr München, Institut für
Nachrichtentechnik, Werner-Heisenberg-Weg 39, D-85577 Neubiberg, 1990.
- [28] T.H. Lee. *The Design of CMOS Radio-Frequency Integrated Circuits*. Cambridge
University Press, Cambridge, UK, 2004.
- [29] F.H. Raab, P. Asbeck, S. Cripps, P.B. Kenington, Z.B. Popovic, N. Pothecary, J.F.
Sevic, and N.O. Sokal. Power Amplifiers and Transmitters for RF and Microwave. *IEEE
Trans. on Microwave Theory and Tech.*, 50:3:814–826, March 2002.
- [30] V. Tarokh, H. Jafarkhani, and A.R. Calderbank. Space-Time Block Codes from
Orthogonal Designs. *IEEE Trans. Inform. Theory*, IT-45:1456–1467, July 1999.
- [31] B.L. Hughes. Differential Space-Time Modulation. *IEEE Trans. Inform. Theory*,
46(7):2567–2578, November 2000.
- [32] B.M. Hochwald and W. Sweldens. Differential Unitary Space-Time Modulation. *IEEE
Trans. Commun.*, 48(12):2041–2052, December 2000.
- [33] H. Jafarkhani. *Space-Time Coding*. Cambridge University Press, New York, 2005.
- [34] G. Wang, W. Su, and X.-G. Xia. Orthogonal-Like Space-Time Coded CPM with Fast
Decoding for Three and Four Transmit Antennas. In *Proc. IEEE Global Telecom.
Conf.*, pages 3321–3325, San Francisco, December 2003.
- [35] E. Lindskog and A. Paulraj. A Transmit Diversity Scheme for Channels with Intersymbol
Interference. In *Proceedings of IEEE International Conference on Communications
(ICC)*, pages 307–311, New Orleans, 2000.
- [36] H. Bouzekri and S.L. Miller. Distance Spectra and Performance Bounds of Space-
Time Trellis Codes Over Quasi-Static Fading Channels. *IEEE Trans. Inform. Theory*,
IT-50:1820–1831, August 2004.
- [37] A. Stefanov and T.M. Duman. Performance Bounds for Space-Time Trellis Codes.
IEEE Trans. Inform. Theory, pages 2134–2140, June 2002.
- [38] D. Aktas and M.P. Fitz. Distance Spectrum Analysis of Space Time Trellis-Coded
Modulations in Quasi-Static Rayleigh Fading Channels. *IEEE Trans. Inform. Theory*,
IT-49:3335–3344, December 2003.
- [39] A. Demir, A. Mehrotra, and J. Roychowdhury. Phase Noise in Oscillators: A Unifying
Theory and Numerical Methods for Characterization. *IEEE Trans. Circuits and
Systems*, 47(5):655–674, May 2000.

- [40] Ed. W.C. Jakes, Jr. *Microwave Mobile Communications*. Prentice–Hall, Inc., New Jersey, 1974.
- [41] O. Tirkkonen and A. Hottinen. Square-Matrix Embeddable Space-Time Block Codes for Complex Signal Constellations. *IEEE Trans. Inform. Theory*, IT-48:384–395, February 2002.
- [42] J.B. Anderson, T. Aulin, and C.-E. Sundberg. *Digital Phase Modulation*. Plenum Press, New York, 1986.
- [43] P. Laurent. Exact and Approximate Construction of Digital Phase Modulation by Superposition of Amplitude Modulated Pulses (AMP). *IEEE Trans. Commun.*, COM-34:150–160, 1986.
- [44] M.K. Simon and M. Alouini. A Unified Approach to the Performance Analysis of Digital Communications over Generalized Fading Channels. *Proceedings of the IEEE*, 86:1860–1877, September 1998.
- [45] R. Raheli, A. Polydoros, and C.-K. Tzou. Per–Survivor Processing: A General Approach to MLSE in Uncertain Environments. *IEEE Trans. Commun.*, 43:354–364, Feb./Apr. 1995.
- [46] R. Schober and L. Lampe. Noncoherent Receivers for Differential Space-Time Modulation. *IEEE Trans. Commun.*, 50(5):768–777, May 2002.
- [47] S. Lv, G. Wei, J. Zhu, and Z. Du. Differential Unitary Space-Time Modulation in Fast Fading Channel. In *Proc. of Veh. Technol. Conf.*, pages 2374 – 2378, September 2004.
- [48] D. Zheng and N.C. Beaulieu. Decision-Feedback Detection for Block Differential Space-Time Modulation. *IEEE Trans. Commun.*, 54(5):900 – 910, May 2006.
- [49] A.J. Viterbi. Error Bounds for Convolutional Codes and an Asymptotically Optimum Decoding Algorithm. *IEEE Trans. Commun.*, 13(2):260–269, April 1967.
- [50] G. Colavolpe and R. Raheli. Noncoherent Sequence Detection of Continuous Phase Modulations. *IEEE Trans. Commun.*, 47(9):1303–1307, September 1999.
- [51] L. Lampe, R. Schober, G. Enzner, and J. Huber. Coded Continuous Phase Modulation with Low-Complexity Noncoherent Reception. *IEEE Trans. Commun.*, 50(4):517–520, April 2002.
- [52] R. Schober, L. Lampe, Y. Ma, and S. Pasupathy. DF-DD for Channels With Phase Noise. *IEEE Trans. Commun.*, 51(6):890–893, June 2003.
- [53] S. Haykin. *Adaptive Filter Theory*. Prentice-Hall, Englewood Cliffs, New Jersey, 1986.

- [54] R.J. Young and J.H. Lodge. Detection of CPM Signals in Fast Rayleigh Flat-Fading Using Adaptive Channel Estimation. *IEEE Trans. Veh. Technol.*, pages 338–347, May 1995.
- [55] M. V. Eyuboğlu and S.U.H. Quershi. Reduced-State Sequence Estimation With Set Partitioning and Decision Feedback. *IEEE Trans. Commun.*, 36(1):13–20, January 1988.
- [56] W.H. Press, S.A. Teukolsky, W.T. Vetterling, and B.P. Flannery. *Numerical Recipes in C++*. Cambridge University Press, New York, 2nd edition, 2002.
- [57] A.J. Viterbi and J.K. Omura. *Principles of Digital Communications and Coding*. McGraw Hill, New York, 1979.
- [58] T. Aulin, C.-E. Sundberg, and N. Rydbeck. Continuous Phase Modulation – Part II: Partial Response Signalling. *IEEE Trans. Commun.*, COM-29:210–225, March 1981.
- [59] A. Sendonaris, E. Erkip, and B. Aazhang. “User Cooperation Diversity – Parts I and II”. *IEEE Trans. Commun.*, 51:1927–1948, November 2003.
- [60] R.U. Nabar, H. Bölcskei, and F.W. Kneubühler. “Fading Relay Channels: Performance Limits and Space–Time Signal Design”. *IEEE J. Select. Areas Commun.*, 22:1099–1109, August 2004.
- [61] G. Kramer, M. Gastpar, and P. Gupta. “Cooperative Strategies and Capacity Theorems for Relay Networks”. *IEEE Trans. Inform. Theory*, pages 3037–3063, September 2005.
- [62] S. Cui, A.J. Goldsmith, and A. Bahai. “Energy-constrained Modulation Optimization”. *IEEE Trans. Wireless Commun.*, pages 2349–2360, September 2005.
- [63] H.El Gamal and D. Atkas. “Distributed Space-Time Filtering for Cooperative Wireless Networks”. In *Proc. IEEE Global Telecom. Conf.*, San Francisco, December 2003.
- [64] R.A. Horn and C.R. Johnson. *Matrix Analysis*. Cambridge University Press, Cambridge, UK, 1999.
- [65] B.M. Hochwald, T.L. Marzetta, T.J. Richardson, W. Sweldens, and R. Urbanke. “Systematic Design of Unitary Space-Time Constellations”. *IEEE Trans. Inform. Theory*, 46:1962–1973, September 2000.
- [66] B.S. Mergen and A. Scaglione. “Randomized Space-Time Coding for Distributed Cooperative Communication”. *IEEE Trans. Signal Processing*, 55:5003–5017, October 2007.
- [67] J.B. Huber. *Trelliscodierung*. Springer, Berlin, 1992.

- [68] S. Cui, A.J. Goldsmith, and A. Bahai. Energy-constrained Modulation Optimization. *IEEE Trans. Wireless Commun.*, 4:5:2349–2360, September 2005.
- [69] C. Li-Chung and J.V. Krogmeier. Analysis of the Effects of Linearity and Efficiency of Amplifiers in QAM Systems. In *IEEE Wireless Com. and Networking Conference*, pages 475–479, New Orleans, USA, March 2003.
- [70] C. Liang, J. Jong, W. Stark, and J. East. Nonlinear Amplifier Effects in Communication Systems. *IEEE Trans. on Microwave Theory and Tech.*, 47:1461–1466, August 1999.
- [71] C. Rapp. Coded and Uncoded M-PSK and CPM Signals on Nonlinear Bandpass Channels: An Approach to a Fair Comparison. In *Proc. IEEE Global Telecom. Conf.*, pages 720–724, San Diego, USA, December 1990.
- [72] A.M. Silvester, L. Lampe, and R. Schober. Distributed Space-Time Continuous Phase Modulation Code Design. *IEEE Trans. Wireless Commun.*, Accepted for publication, 2008. [http://www.ece.ubc.ca/~annas/Distributed ST-CPM Code Design.pdf](http://www.ece.ubc.ca/~annas/Distributed-ST-CPM-Code-Design.pdf).
- [73] J.B. Andersen, T.S. Rappaport, and S. Yoshida. Propagation Measurements and Models for Wireless Communications Channels. *IEEE Communications Magazine*, 33:1:42–49, January 1995.
- [74] T. Song, H.S. Oh, S. Hong, and E. Yoon. A 2.4-GHz sub-mW CMOS Receiver Front-end for Wireless Sensors Networks. *IEEE Microwave and Wireless Components Letters*, 16:206–208, April 2006.
- [75] K. Giannopoulou, A. Katsareli, D. Dres, D. Vouyioukas, and P. Constantinou. Measurements for 2.4 GHz Spread Spectrum System in Modern Office Buildings. In *Mediterranean Electrotechnical Conference*, pages 326–329, Limassol, Cyprus, May 2000.
- [76] C.E. Shannon. A Mathematical Theory of Communication. *Bell System Tech. Journal*, 27:623–656, October 1948.
- [77] S. Benedetto, D. Divsalar, G. Montorsi, and F. Pollara. Serial Concatenation of Interleaved Codes: Performance Analysis, Design, and Iterative Decoding. *IEEE Trans. Inform. Theory*, 44:3:909–926, May 1998.
- [78] K.R. Narayanan and G.L. Stüber. Performance of Trellis-Coded CPM with Iterative Demodulation and Decoding. *IEEE Trans. Commun.*, 49:4:676–687, April 2001.
- [79] M. Xiao and T.M. Aulin. Serially Concatenated Continuous Phase Modulation With Convolutional Codes Over Rings. *IEEE Trans. Commun.*, 54:8:1387–1396, August 2006.

- [80] X. Li, A. Chindapol, and J.A. Ritcey. Bit-interleaved Coded Modulation with Iterative Decoding and 8PSK Signaling. *IEEE Trans. Commun.*, 50:8:1250–1257, August 2002.
- [81] S. Howard, C. Schlegel, and L. Perez. Differential Turbo Coded Modulation over Unsynchronized Channels. In *IASTED 3rd International Conference on Wireless and Optical Communications*, pages 96–101, Banff, Alberta, 2002.
- [82] R. Nuriyev and A. Anastasopoulous. Rotationally Invariant and Rotationally Robust Codes for the AWGN and Noncoherent Channel. *IEEE Trans. Commun.*, 51:12:2001–2010, December 2003.
- [83] L.R. Bahl, J. Cocke, F. Jelinek, and J. Raviv. Optimal Decoding of Linear Codes for Minimizing Symbol Error Rate. *IEEE Trans. Inform. Theory*, 20:2:264–287, March 1974.
- [84] T.J. Richardson and R.L. Urbanke. The Capacity of Low-Density Parity-Check Codes Under Message-Passing Decoding. *IEEE Trans. Inform. Theory*, 47:2:599–618, February 2001.
- [85] S. ten Brink. Convergence Behavior of Iteratively Decoded Parallel Concatenated Codes. *IEEE Trans. Commun.*, 49:10:1727–1737, October 2001.
- [86] G. Kramer. Serially and Parallel Concatenated (Turbo) Codes. *Mini Course at TU-Wien and FTW*.
- [87] D.W. Marquardt. An Algorithm for Least-Squares Estimation of Nonlinear Parameters. *J. Appl. Math.*, 11:2:431–441, June 1963.
- [88] D.M. Arnold, H.-A. Loeliger, P.O. Vontobel, A. Kavčić, and W. Zeng. Simulation-Based Computation of Information Rates for Channels With Memory. *IEEE Trans. Inform. Theory*, 52:8:3498–3508, August 2006.
- [89] L. Lampe. *Noncoherent Coded Modulation*. Doktor-Ingenieur, Der Universität Erlangen-Nürnberg, Der Technischen Fakultät, Erwin-Rommel-Str. 60, 91058 Erlangen, 2002.
- [90] S. Haykin. *Digital Communications*. John Wiley & Sons, Inc, New York, USA, 1988.
- [91] S. Dolinar and D. Divsalar. Weight Distributions for Turbo Codes Using Random and Nonrandom Permutations. In *JPL Progress Report*, pages 42–122, 1995.

Appendix A

Related Publications

The following is a list of publications that are based on the research conducted for this thesis.

Journal Papers

1. A.-M. Silvester, L. Lampe, and R. Schober. Energy Consumption of Distributed Space-Time Coding Methods. Submitted to the *IEEE Transactions on Wireless Communications*.
2. A.-M. Silvester, L. Lampe, and R. Schober. Distributed Space-Time Continuous Phase Modulation. *IEEE Transactions on Wireless Communications*, 7:11:4455-4461, November 2008.
3. A.-M. Silvester, L. Lampe, and R. Schober. Space-Time Continuous Phase Modulation for Non-Coherent Detection. *IEEE Transactions on Wireless Communications*, 7:4:1264–1275, April 2008.
4. A.-M. Silvester, R. Schober, and L. Lampe. Burst-Based Orthogonal ST Block Coding for CPM. *IEEE Transactions on Wireless Communications*, 6:4:1208–1212, April 2007.

Conference Papers

5. A.-M. Silvester, L. Lampe, and R. Schober. Cooperative Diversity with Continuous Phase Modulation. In *Proc. Sensor, Signal and Information Processing Conference*,

Invited Paper, Sedona, May 2008.

6. A.-M. Silvester, L. Lampe, and R. Schober. Distributed Space-Time Transmission with CPM. In *Proc. IEEE Global Telecommunications Conference (Globecom)*, Washington, December 2007.
7. A.-M. Silvester, L. Lampe, and R. Schober. Diagonal Block Space-Time Code Design for Continuous-Phase Modulation. In *Proc. IEEE Global Telecommunications Conference (Globecom)*, San Francisco, December 2006.
8. A.-M. Silvester, R. Schober, and L. Lampe. Burst-based orthogonal ST Block Coding for CPM. In *Proc. IEEE Global Telecommunications Conference (Globecom)*, St. Louis 2005.